공학박사학위논문

Analysis of Influential Factors on Deionization Capacity and Rate in Capacitive Deionization

축전식 탈염기술의 담수화 용량과 속도 특성에 영향을 미치는 주요인자 평가와 분석

2015년 2월

서울대학교 대학원

화학생물공학부

김태영

Analysis of Influential Factors on Deionization Capacity and Rate in Capacitive Deionization

축전식 탈염기술의 담수화 용량과 속도 특성에 영향을 미치는 주요인자 평가와 분석

지도교수 윤제용

이 논문을 공학박사 학위논문으로 제출함
2014년 10월

서울대학교 대학원
공과대학 화학생물공학부
김태영

김태영의 공학박사 학위논문을 인준함
2014년 11월

위원장 이 정혁 (인)
부위원장 윤 제용 (인)
위원 朴 鍾 來 (인)
위원 오 승 모 (인)
위원 강 경 석 (인)

Abstract

Analysis of Influential Factors on Deionization Capacity and Rate in Capacitive Deionization

Taeyoung Kim
School of Chemical and Biological Engineering
The Graduates School
Seoul National University

Capacitive deionization (CDI) is an emerging desalination process to produce fresh water from saline water. Compared to conventional desalination processes such as thermal distillation and reverse osmosis (RO), CDI is more simple, energy-efficient, and environment-friendly. These advantages could make CDI as an alternative and/or supplementation to the conventional desalination processes. To make use of the advantages of CDI, a variety of studies have been carried out focusing on improving deionization performance. Among those, carbon electrodes play an important role to determine the performance; thus, many efforts have been made to analyze properties of carbon electrodes, develop a novel carbon material, and modify carbon electrodes. Although there have been considerable advances, systematic studies providing influential factors on deionization performance are insufficient. In this study, deionization performance was investigated especially focusing on capacity and rate to substantially extend previous understandings on CDI. Firstly, to understand deionization capacity, activated carbon materials of various surface areas were fabricated to composite electrodes and their electrochemical and deionization performances were examined. The results showed that a higher capacitance led to a higher capacity, where ~70% of charge capacity converted from capacitance was utilized for deionization. In the further study, a model equation to correlate deionization capacity with salt concentration and applied voltage was used to predict the deionization performance. The equation successfully modeled the experimental results obtained over salt concentration and applied voltage. In particular, when discharge voltage was increased with fixed charge voltage, charge efficiency was enhanced with marginal loss in the capacity, which suggests a possibility of an efficient energy-use by adjusting the operating condition. Secondly, a novel carbon material and analytical method were proposed to investigate deionization rate in CDI. A novel carbon material called metal organic framework (MOF)-derived carbon (MDC) with hierarchic pore structure was synthesized and electrochemical and deionization performances were examined compared to microporous and mesoporous carbons. The result confirmed that hierarchically porous carbon could show outstanding deionization rate mainly due to its unique pore structure. To develop a new method for evaluating rate capability of deionization, potential sweep method was utilized which applies voltage under different scan rates for charging a CDI cell.

Deionization capacity was obtained over low to high scan rates and its retention ratio was used as a criterion for the rate capability; high retention ratio represents better rate capability. This method was applicable for various parameters such as electrode thickness, salt concentration, and flow rate. As a result, the thinner electrode, high salt concentration, and high flow rate showed better rate capability. Lastly, a novel concept to evaluate deionization performance was proposed, called the CDI Ragone plot. This plot was developed to show deionization capacity and rate over wide range of current load in constant current operation, thus maximum capacity and rate could be available. Moreover, it allows intuitive acquisition of deionization performance obtained in different parameters. In conclusion, this dissertation could provide an insight to understand deionization capacity and rate. Furthermore, a novel concept was firstly proposed, called the CDI Ragone plot, which could simultaneously demonstrate two important parameters in CDI, which are deionization capacity and rate. Therefore, it would be a comprehensive guide for deionization performance as a future standard in CDI.

Keywords : Water, desalination, capacitive deionization, carbon electrode, deionization capacity, deionization rate

Student Number : 2008-21066

Tables of Contents

1. Introduction 1

1.1. Backgrounds 1

1.2. Objectives 4

2. Literature review 7

2.1. Activated carbons 7

2.2. Carbon fibers 21

2.3. Carbon aerogels 27

2.4. Ordered mesoporous carbons 30

2.5. Carbon nanotubes 33

2.6. Graphene 35

2.7. Carbon/carbon composites 38

2.8. Novel carbon materials 39

3. Deionization Capacity in Capacitive Deionization 43

3.1. Relationship between Capacitance of Activated Carbon Composite Electrodes Measured at a Low Electrolyte Concentration and Their Deionization Performance in Capacitive Deionization 43

3.1.1. Introduction 43
3.1.2. Experimental.. 45
3.1.3. Results 52
3.1.4. Discussion.. 66
3.1.5. Conclusions 74

3.2. Enhanced Charge Efficiency and Reduced Energy Use in Capacitive Deionization by Increasing the Discharge Voltage 76

3.2.1. Introduction 76
3.2.2. Theory 81
3.2.3. Experimental.. 91
3.2.4. Results and Discussion 98
3.2.5. Conclusions 112

4. Deionization Rate in Capacitive Deionization 115

4.1. Solvent Evaporation Mediated Preparation of Hierarchically Porous Metal Organic Framework-derived Carbon with Controllable and Accessible Large-scale Porosity 115

4.1.1. Introduction 115
4.1.2. Experimental.. 120

4.1.3. Results and Discussion 123
4.1.4. Conclusions 148

4.2. Potential Sweep Method to Evaluate Rate Capability in Capacitive Deionization 149

4.2.1. Introduction 149
4.2.2. Materials and Methods 151
4.2.3. Theory 160
4.2.4. Results and Discussion 161
4.2.5. Conclusions 184

5. CDI Ragone Plot as a Functional Tool to Evaluation Deionization Performance in Capacitive Deionization 185

5.1. Introduction 185

5.2. Experimental 187

5.3. Results and Discussion 191

5.4. Conclusion 210

6. Conclusions 211

List of Figures

Figure 2-1. SEM image of activated carbon composite electrode......................11

Figure 2-2. Comparison of (a) electrochemical and (b) deionization performance between CDI and MCDI. 14

Figure 2-3. Classification of carbon electrode. 15

Figure 2-4. Cell configuration of (a) capacitive deionization and (b) membrane capacitive deionization..19

Figure 2-5. Schematic diagram of FCDI cell configuration [22]. 20

Figure 2-6. SEM images of (a-c) carbon cloth and (d) activated carbon composite electrode. (e) Contact angles of carbon cloth and (f) activated carbon composite electrode [57]. 23

Figure 2-7. Schematic diagram for boron removal steps in CDI [58]................24

Figure 2-8. SEM images of carbon aerogels synthesized under various RF wt%. 29

Figure 2-9. TEM images of CMK-1 and CMK-2 [89]......................................32

Figure 2-10. Various images of carbon nanotube sponges made by chemical vapor deposition (CVD) [9]. 34

Figure 2-11. Comparison of activated carbon and GNFs in relation to their BET surface area, deionization performance, and pore structure [7].................37

Figure 2-12. Schematic diagram to synthesize MDC...41

Figure 3-1. Schematic diagram of the CDI system. The CDI module consists of (1) two pairs of graphite sheets, (2) two pairs of carbon composite electrodes, and (3) nylon as a spacer. Feed solution (0.01 M NaCl) was supplied to the CDI module using a peristaltic pump (10 ml/min). Meanwhile, voltage (1.2 V) was applied and conductivity of an effluent was continuously monitored using a flow-type conductivity meter. 49

Figure 3-2. Comparison between batch and single-pass operations.................... 51

Figure 3-3. CV curves of carbon composite electrodes used in this study. The specific capacitance was obtained by dividing current by the scan rate (2 mV/s) and the mass of an electrode. The concentration of electrolyte was 1 M NaCl. .55

Figure 3-4. Relationship between BET specific surface area (BET-SSA) and capacitance. Capacitance was measured using cyclic voltammetry in 1 M NaCl (scan rate = 2 mV/s). BET-SSA was obtained for powdered carbons before they are fabricated to carbon composite electrodes (carbon:superP:binder = 86:7:7 in weight ratio). 56

Figure 3-5. Concentration-dependent capacitive behavior of carbon composite electrodes. (a) Representative galvanostatic charge/discharge voltage profile of MSP-20 recorded at a current density of 0.5 mA/cm2; electrolyte concentrations were 1 M (solid line), 0.1 M (dotted line), and 0.01 M (dashed line) NaCl. Magnified insets show the voltage profiles for 0.01 M (left side) and 1 M (right side) when discharging started. (b) The specific capacitance was calculated from discharging profiles. 59

Figure 3-6. Galvanostatic charge/discharge voltage profiles of S-51HF............ 60

Figure 3-7. Galvanostatic charge/discharge voltage profiles of SX PLUS. 61

Figure 3-8. Galvanostatic charge/discharge voltage profiles of YS-2. 62

Figure 3-9. Representative deionization performance of carbon composite electrodes. (a) Conductivity of an effluent was continuously recorded was plotted over time. The operation was carried out for 60 min; 1.2 V for 10 min (deionization step) and 0 V for 10 min (regeneration step) were repeated for three times. (b) The conductivity data of the 3rd deionization step (40–50 min) was converted to deionization capacity (mg/g) by integration, representing to the mass of deionized ionic charge (mg) divided by the mass of a pair of electrodes (g). 65

Figure 3-10. Schematic diagrams of ionic behavior during deionization in CDI. 67

Figure 3-11. Correlation between converted deionization capacity (*D*$_c$) and deionization capacity (*D*). The converted deionization capacity was calculated by Eq. (3) and applying capacitance (additional x-axis below the plot) measured at 0.01 M NaCl (filled symbols) and 1 M NaCl (open symbols), representing the maximum deionization capacity. Deionization capacity was evaluated in the CDI system at 0.01 M NaCl. Note that filled symbols are located between D=0.6D_c and D=0.8D_c (light gray-filled area), indicating that 60–80% of charge capacity is utilized in deionization. Open symbols are located between D=0.5D_c and D=0.6D_c (dark gray-filled area). In this case, 50–60% of charge capacity (evaluated at 1 M NaCl) is utilized in deionization.72

Figure 3-12. (a) Schematic diagram of a CDI cell as used in this study. (b)

Operational cycles where discharge voltage is varied (V_{disch} = 0 V and 0.3 V) as a function of time. 77

Figure 3-13. Experimental data of CDI cycles for effluent salt concentration and accumulated charge, versus time (V_{ch}=1.2 V, V_{disch}=0.3 V, c_∞=20 mM, half-cycle time 1200 s, only first 500 s shown). 99

Figure 3-14. Equilibrium salt adsorption, charge, and charge efficiency as function of salt concentration and V_{ch}, which is the cell voltage during charging (V_{disch}=0 V). Solid lines obtained according to the i-mD model (parameters in Table 3-2). 102

Figure 3-15. Salt adsorption, charge, and charge efficiency (Λ) as function of salt concentration and discharge voltage, V_{disch} (V_{ch}=1.2 V). Solid lines obtained according to the i-mD model (parameters in Table 3-2). 104

Figure 3-16. CDI at short cycle times. (a). Average salt adsorption rate as function of half-cycle time (HCT; charging and discharging step of equal duration, namely equal to HCT) and as function of V_{disch}. (b). Dynamic charge efficiency as function of HCT (V_{ch}=1.2 V, c_∞=20 mM, electrode thickness 235 μm). 108

Figure 3-17. Constant-current CDI operation. (a) Effluent salt concentration as function of V_{disch} (data represented by dots; theory calculations by lines). (b) Dynamic charge efficiency vs. V_{disch}. (c) Electrical energy input per ion removed (kT) vs. V_{disch}. (I_{ch}=30.6 A/m^2, c_∞=20 mM, electrode thickness 260 μm). 111

Figure 4-1. Schematics showing the formation of hierarchically porous carbon with an ultrahigh pore volume from MOFs; (a) The structural evolution of the large-sized pore seeds with micrograin boundaries by non-volatile solvent evaporation; (b) The formation of amesoporous metal oxide@carbon hybrid; (c) Micro- and macroporeswere introduced by continuously reducing the metal oxide, evaporating the metal, and carbonizing the material. 119

Figure 4-2. FE-SEM and TEM images of the product obtained (a–d) after pore activation (MDC-A) and (e–h) upon immersion in DMF (MDC-D). 126

Figure 4-3. Additional FE-SEM micrographs of MDC-D. 127

Figure 4-4. FE-SEM micrographs of the MDC-C. 128

Figure 4-5. (a) Nitrogen adsorption isotherms and the corresponding pore size distributions determined using (b) the NLDFT function (microporosity) and (c) the BJH equation (mesoporosity). 131

Figure 4-6. (a) XRD patterns and (b) Raman spectroscopy of the products. 133

Figure 4-7. FE-SEM images of (a) MOF_A and (b) MOF_D (inset: whole image of MOF). (c) N_2 adsorption isotherms of the products. 135

Figure 4-8. XRD patterns of the products. 136

Figure 4-9. FE-SEM micrographs and XRD patterns of the carbonizing IRMOF-1 immersed in the DMF at different temperatures. (a) 200, (b) 600, (c) 800, and (d) 900^{o}C for 3 h. 138

Figure 4-10. (a) CVs and (b) Frequency-dependent capacitance of MDC-D, CEP21, and CA. 141

Figure 4-11. Cyclic voltammograms of the MDC-D recorded at various scan rates. 142

Figure 4-12. Cyclic voltammograms of the microporous carbon (CEP-21) recorded at various scan rates. 143

Figure 4-13. Cyclic voltammograms of the carbon aerogel (CA) recorded at various scan rates. 144

Figure 4-14. Nitrogen adsorption isotherms and corresponding meso- and macropore size distribution of (a) CA and (b) CEP21. Calculated BET SSA with total pore volume at 0.99 of relative pressure of CA and CEP21 are 790 (3.45) and 2210 m^2/g (1.00 cm^3/g), respectively. 145

Figure 4-15. (a) conductivity changes in the effluent (top) and recyclability of MDC-D (bottom), and (b) deionization capacity (the integrated number of deionized ions per gram electrode) as a function of time. 146

Figure 4-16. Schematics showing the pore characteristics of a typical microporous carbon material (left) and a hierarchically porous MDC-D (right). 147

Figure 4-17. (a) Nitrogen adsorption isotherm and (b) pore size distribution of MSP-20. 152

Figure 4-18. A schematic diagram of an experimental setup for the CDI tests. For the deionization, the CDI module was charged and discharged with a power supply which was connected to the current collectors inside the module.

Feed solution (10 mM NaCl) passed through a spacer from outside to the center, which was located between the cation- and anion-exchange membranes. Then, the effluent conductivity was continuously recorded using a flow-type conductivity meter. 157

Figure 4-19. Representative conductivity and pH profiles as a function of time in potential sweep operation (electrode thickness=300 μm, scan rate=2 mV/s).158

Figure 4-20. Representative cycle performance of the 300-μm-thick electrode at a scan rate of 4 mV/s. 159

Figure 4-21. Representative effluent conductivity profiles as a function of the scan rate for different electrode thicknesses ((a) 200, (b) 300, and (c) 400 μm). The module was charged from 0 to 1.2 V at different scan rates (2, 4, 8, 12 mV/s) followed by short-circuiting until the conductivity returned to the initial value. 163

Figure 4-22. Deionization capacity, charge, and dynamic charge efficiency as functions of the scan rate and electrode thickness. Deionization capacity (rectangle) and charge (triangle) were obtained from the conductivity meter and the cycler for (a) 200-, (b) 300-, and (c) 400-μm-thick electrodes. (d) The dynamic charge efficiency was calculated by dividing the deionization capacity by the total charge that transferred to the electrode. 165

Figure 4-23. Retention ratio of the deionization capacity as a function of the scan rate for different electrode thicknesses. The retention ratio was calculated by dividing the deionization capacity of each scan rate by that of 2 mV, indicating the rate capability. 167

Figure 4-24. Representative conductivity profiles obtained at different flow rates (electrode thickness=300 μm, scan rate=4 mV/s). 169

Figure 4-25. Deionization capacity, charge, and dynamic charge efficiency as a function of scan rate for different flow rates (electrode thickness=300 μm)..170

Figure 4-26. Retention ratio as functions of scan rate and flow rate (electrode thickness=300 μm). 171

Figure 4-27. Representative conductivity profiles obtained at different salt concentrations (electrode thickness=300 μm, scan rate=4 mV/s). 173

Figure 4-28. Deionization capacity, charge, and dynamic charge efficiency as a function of scan rate for different salt concentrations (electrode thickness=300 μm). 174

Figure 4-29. Retention ratio as functions of scan rate and salt concentration (electrode thickness=300 μm). 175

Figure 4-30. Mean deionization rate of the electrodes with different thicknesses as a function of the current density. The mean deionization rate (mg/g/s) was calculated by dividing the deionization capacity (mg/g) by the duration of charging (s). Deionization performance tests were carried out in the constant current mode; the module was charged at various current densities (2, 5, 9, 15 mA) with a cutoff voltage of 1.2 V..................................177

Figure 4-31. Cyclic voltammograms of the carbon composite electrodes with different thicknesses. The results were obtained in 1 M NaCl solution at a scan rate of (a) 2 mV/s and (b) 50 mV/s. 179

Figure 4-32. Capacitance vs. frequency plots for different electrode thicknesses...181

Figure 5-1. A conceptual diagram of a CDI Ragone plot (a) and the representative conductivity profiles (b). A CDI Ragone plot consists of the deionization capacity and mean deionization rate, indicating total removed ions during charging and deionization capacity divided by duration of charging, respectively. These two parameters were obtained under constant current charging followed by zero-voltage discharging shown in (b); the area below the influent conductivity (dashed line) refers to the removed ions by the CDI cell. Data points obtained at each current load are located in the CDI Ragone plot, thus becoming a curve representing its experimental condition. The location and shape of a curve represent the deionization performance; two imaginary cases would be a high rate & low capacity (blue color) and a high capacity & low rate (red color). An ideal CDI system would shift a curve toward the upper, right region of the plot (green color). 192

Figure 5-2. Representative voltage profiles of different salt concentrations obtained during charging step. 196

Figure 5-3. Representative voltage profiles of different flow rates during charging step. 198

Figure 5-4. Extended data of variation in electrode thickness. Original figure (Fig. 5-5(c)) contained plots for various electrodes in the range of 200 to 400 μm. In a further experiment, more thinner electrode (140 μm, ◆) was fabricated and plotted together with the previous electrodes. The plot for the 140-μm-thick electrode was located above the 200-μm-thick electrode, indicating better deionization rate. It implies that the influence of electrode thickness on rate is valid even below 200 μm. 200

Figure 5-5. Effect of various parameters on the CDI Ragone plot. Each plot shows the effect of the (a) salt concentration, (b) flow rate, (c) electrode thickness, and (d) type of carbon materials. Each parameter was examined based on the standard operating condition (10 mM NaCl, 2 ml/min, 300 μm, and MSP-20), and the range of the current load was from 1 to 25 mA but properly adjusted to show the overall performance. Detailed operating parameters for each experimental condition are provided in Table 5-1. 204

Figure 5-6. CDI Ragone plots normalized by foot print area of electrode (3.02 cm^2) for (a) electrode thickness and (b) type of carbon materials. Results of Figs. 5-5(c) and 5-5(d) were converted from mass-based performance (mg/g and mg/g/s) to area-based performance (mg/cm^2 and mg/cm^2/s). All experiments were carried out under the standard operating condition (10 mM NaCl, 2 ml/min, 300 μm, and MSP-20), unless otherwise indicated. Detailed operating parameters for each experimental condition are provided in Table 5-1. 205

Figure 5-7. Contact angle images of (a) CEP21 and (b) MSP-20. To obtain these images and contact angle values, a contact angle analyzer (KRÜSS, DSA100, Germany) and DSA100 software were used. The electrode was dried prior to the measurement and installed to the analyzer. Then, 6 μL of deionized (DI) water attached at the tip of a needle was smoothly transferred to the electrode surface by direct contact and following detachment. The contact angle measurement was immediately made after the transfer in order to avoid water penetration into the electrode and evaporation. The contact angle was collected from five different points of the electrode, and the resulting averaged values were 131±1 and 116±3° for CEP21 and MSP-20, inferring that the surface of MSP-20 is more hydrophilic compared to that of CEP21. Though various factors could affect contact angle measurement, oxygen functional groups developed on the carbon would play a major role. XPS analysis confirmed that atomic O/C ratio of MSP-20 was 0.20, which is two-fold higher than that of CEP21 (0.10), indicating MSP-20 contains more oxygen functional groups. 206

Figure 5-8. (a) Mass-based deionization performance as a function of pore size and (b) the CDI Ragone plot of various carbon materials normalized by the mass of electrodes. 208

Figure 5-9. (a) Volume-based deionization performance as a function of pore size and (b) the CDI Ragone plot of various carbon materials normalized by the volume of electrodes. 209

List of Tables

Table 2-1. Deionization (salt adsorption) capacity (mg/g) of various carbon materials. 42

Table 3-1. Characterization of activated carbons. 53

Table 3-2. Deionization capacity values calculated using a charging and a discharging step. 73

Table 3-3. System and electrode dimensions, operational parameters, and settings for theoretical calculations. 97

Table 4-1. Information on the electrodes used in this study. 153

Table 4-2. Parameters obtained by equivalent circuit analysis as a function of the electrode thickness. 183

Table 5-1. Detailed operating parameters for each experimental condition. 190

1. Introduction

1.1. Backgrounds

Securing fresh water is the most important task for humankind. Desalination process could provide a solution to achieve this goal by producing fresh water from saline water with remarkable advances in water treatment technologies over the past few decades. Thermal distillation and reverse osmosis (RO) have been the most successful processes [1]. Recently, capacitive deionization (CDI) has attracted growing attentions as an alternative and/or supplementation to the conventional desalination processes [2]. This novel desalination process is a modified system from supercapacitor, which is one of energy storage devices [3], thus it is driven by applying electrical potential to a pair of porous carbon electrodes. Compared to supercapacitor, however, a solution between the electrodes is extracted to obtain ion-deficient solution or fresh water while ions are stored in double layer of the porous electrodes. CDI is a simple, energy-efficient, and environmentally friendly process, and therefore, it is expected to become a future desalination technology.

So far, there have been numerous attempts to improve deionization performance of CDI, especially for last two decades. The majority of them were to use novel carbon materials such as carbon aerogel [4], mesoporous carbon [5], carbon fiber [6], graphene [7, 8], carbon nanotube [9], carbide-derived carbon [10], and

MOF(metal organic framework)-derived carbon [11]. The performance of the carbon electrodes was able to be further improved by adopting functional groups [12-14], heterogeneous particles [15, 16], and ion-exchange membranes or polymers [17, 18]. Other electrode materials can be applied instead of carbon in order to make use of Faradaic reactions [19, 20]. Adjusting operating parameters also achieved enhanced performance in various criterions [17, 21]. In addition, the development of a new process, called flow-CDI (FCDI) where flowable carbon slurry served as an electrode, has been suggested as an innovative breakthrough for the future CDI technology [22].

Regardless of strategies that have been explored for the advancements, a carbon electrode plays a crucial role to determine deionization performance in CDI. Better capacity and rate of deionization, which are the most important parameters of deionization performance in CDI, can be achieved by using a carbon material with high surface area and optimal pore structure. Moreover, these properties are applicable only when an electrode containing the carbon material shows a proper electrochemical performance. In this regard, both physicochemical and electrochemical properties of a carbon electrode are quite important for the development of CDI process with outstanding deionization performance. However, most of previous studies have directed towards achieving better performance in terms of capacity and rate without suggesting a comprehensive insight related to such properties. Therefore, further studies are required to systematically understand deionization performance and mechanism in relation to physicochemical and electrochemical properties of carbon electrodes.

1.2. Objectives

In this dissertation, deionization performance of CDI was investigated to find influential factors especially focusing on deionization capacity and rate, which are the most significant parameters in CDI. To achieve this goal, extensive studies were carried out over three parts.

Firstly, the deionization capacity was investigated to understand the amount of ions that can be removed through CDI process. For this, activated carbons with different surface area were selected and their capacitance values were obtained over 0.01 to 1 M NaCl in an electrochemical cell. Then, deionization capacity was evaluated in a CDI cell and it was quantitatively compared to capacitance. To further understand the deionization capacity, a model equation was adopted to estimate its behavior. Modeling was proved by adjusting charge and discharge voltage in the range of 5 to 80 mM NaCl, and intensive discussion was provided.

Secondly, the rate capability was investigated with an optimal pore structure of a carbon for rapid deionization and by developing systematic method to evaluate deionization rate in CDI. Carbon electrodes of various pore structures were prepared from activated carbon, carbon aerogel, and MOF-derived carbon (MDC). Activated carbon and carbon aerogel represent microporous and mesoporous carbon, respectively. The MDC is hierarchically porous carbon containing micro-, meso-, and macropores. From electrochemical and deionization performance of these carbon electrodes, a role of pore structure in deionization rate was examined. In addition, potential sweep method was used to evaluate rate capability of deionization in CDI. Effects of electrode thickness, salt concentration, and flow rate on deionization rate were investigated by using the potential sweep method.

Lastly, a novel concept to evaluate deionization performance was proposed, called the CDI Ragone plot. The original methodology of Ragone plot in the field of energy storage device was properly modified for CDI; the CDI Ragone plot consists of deionization capacity and rate while the Ragone plot consists of energy and power. To achieve the plot, both parameters were obtained from a low to high rate in constant current operation. Feasibility of this new methodology was confirmed by investigating well-established operating parameters such as electrode thickness, salt concentration, flow rate, and type of carbon.

2. Literature review

2.1. Activated carbons

Among various carbon materials for CDI, activated carbon is the most commercially feasible electrode material with outstanding deionization performance. Normally, carbon precursors are carbonized at the elevated temperature (>700^{o}C) under inert atmosphere (i.e. N_2), and they are chemically (KOH, NaOH, $ZnCl_2$, etc.) or physically (CO_2 and H_2O) activated. The activation process can provide nano-sized pores into carbon structure depending on the activation condition such as activation time, temperature, and types of agents. It enables activated carbons to have high specific surface area (500–2500 m^2/g), which is one of the most important requirements for a CDI electrode to exhibit outstanding deionization performance. Currently, numbers of activated carbons with various price and property are available in the market; thus, many studies have been carried out focusing on physicochemical properties of electrodes, chemical or physical modifications, operating parameters, and developing a new design by using activated carbons.

Fundamental study to examine the effect of pore structure was presented by Wang et al. [23]. Six commercial activated carbons with different surface area ranging from 917 to 2030 m^2/g were purchased and their deionization performance was examined. Electrosorption capacity was found to increase with increasing surface area of the carbon; especially the mesopore volume of the carbons was suggested to provide more contribution to the deionization performance. Extended study to investigate the effect of surface area of activated carbons was carried out in relation to electrochemical properties [24]. In this study, capacitance of four commercial activated carbons (630–2266 m^2/g) was evaluated under various electrolyte concentrations (0.01, 0.1, and 1 M NaCl) by using galvanostatic charge/discharge method. The capacitance measured at the low electrolyte concentration (0.01 M NaCl) was converted to charge capacity and plotted versus deionization capacity obtained at the same concentration. This relationship indicated that 60–80% of charge capacity derived from capacitance can be utilized for deionization, which ratio is in good agreement with charge efficiency (a ratio of desalinated ions to transferred charge to electrodes [25]). Electrode thickness variation is also one of important operating parameters in CDI. Porada et al. reported the effect of electrode thickness and its asymmetric variation on salt adsorption capacity and kinetic [10, 26]. In addition, electrode thickness was found to one of properties affecting rate capability evaluated by potential sweep method [27]. This study also reported capacitive behaviors of carbon electrodes with different thickness as functions of scan rate and frequency by using cyclic voltammetry (CV) and electrochemical impedance spectroscopy (EIS), respectively. In these studies, the thinner electrode could show more swift deionization when the performance was normalized by the mass of both electrodes. Another parameter which is inevitable but unfavorable component of CDI electrode is a polymer bind. As shown in Fig. 2-1, activated carbons normally in the form of powder, so that a polymer binder must be included to fabricate a sheet-type electrode and at the same time to keep the carbon powders inside the electrode structure during deionization. However, the polymer binder is unfavorable component as it increases the hydrophobicity and electrical resistance of an electrode. With increasing polyvinylidene fluoride (PVDF) binder content from 10 to 40 wt%, internal resistance increased and capacitance decreased though mechanical strength was enhanced [28]. Many attempts have been made to find solutions for this problem. Combining an ion-exchange resin with electrode could enhance the hydrophilicity of the electrode [29]. Acrylic acid was also suggested as a promising binder [30]. When compared to phenolic resin, polytetrafluoroethylene (PTFE), and epoxy, acrylic acid resulted in flexible and hydrophilic electrode with carbonization [31]. Conducting agent is also one of important components of a carbon electrode together with the carbon and polymer binder. Addition of conducting agent such as carbon black was known to increase electrical conductivity of an electrode, leading to better rate capability. As mentioned in the introduction section, CDI is competitive desalination process for brackish water. In such low concentrations, contribution of the solution to overall resistance in CDI system becomes significant; thus, the effect of an electrical conductivity increase of the electrode on deionization performance was marginal [32]. The performance was rather deteriorated in terms of deionization capacity ($mg/g_{electrode}$) because of high conducting agent loading. The highest conducting agent content resulted in poor performance even when the performance was compared based on the mass of the activated carbon (mg/g_{carbon}). On the other hand, when the electrical conductivity of an activated carbon is too low, conducting agent can enhance the performance. In this case, small surface area of a conducting agent compared to activated carbons would be disadvantageous. It can be solved by introducing a conducting agent with high surface area [33].

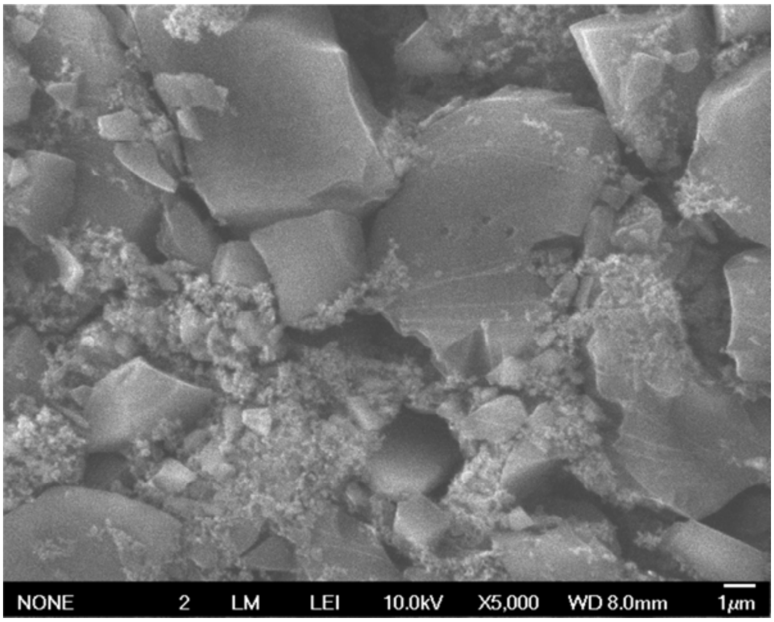

Figure 2-1. SEM image of activated carbon composite electrode.

Activated carbon electrodes have been physically or chemically modified to enhance the deionization performance. Among various strategies, ion-exchange membranes allowed for the most successful improvements, called membrane-assisted CDI (MCDI) [17, 27, 34-40]. In this configuration, cation- and anion-exchange membranes are placed above negative and positive electrodes. Ion-exchange membranes only allow for the transport of counter-ions while it prevents that of co-ions. Without ion-exchange membranes in a typical CDI configuration, co-ions are released to spacer channel when the voltage is applied to the cell, thus providing undesirable ionic charges to the effluent. Therefore, the deionization performance can be greatly enhanced in MCDI because the charge transferred to the electrodes is only used to attract counter-ions. In an electrochemical point of view, MCDI is disadvantageous because cation- and anion-exchange membranes serve as resistive factors. As confirmed in Fig. 2-2(a), MCDI has higher y-intercept; thus, it has higher ohmic resistance compared to CDI. From this result, poor deionization performance is expected for MCDI because a higher ohmic resistance leads to low deionization capacity with poor rate performance. However, MCDI showed better deionization performance compared to CDI as confirmed in Fig. 2-2(b). The decrease in conductivity was rapid and the area between influent and effluent conductivity was larger for MCDI. This conflicting result can be explained by unique properties of ion-exchange membranes; ion-selectivity only allows for penetration of counter-ions, thus deionization is more efficient even though the resistance is higher than CDI. Another route to make use of this advantage is to coat ion-exchange resins directly onto electrodes [18, 41-43]. This method could facilitate the contact between electrodes and ion-exchange resins, thus lowering contact resistance. Another strategy to enhance the deionization performance is to introduce surface charge. Additional surface charge could facilitate the attraction of counter-ions and increase hydrophilicity. For example, TiO_2-incorporated carbon electrodes showed better deionization performance because of increased charge storage sites and hydrophilicity [44-47]. Similar enhancement was reported with SiO_2 coating [48], KOH treatment [44], nitric acid treatment [13], and plasma oxidation [49].

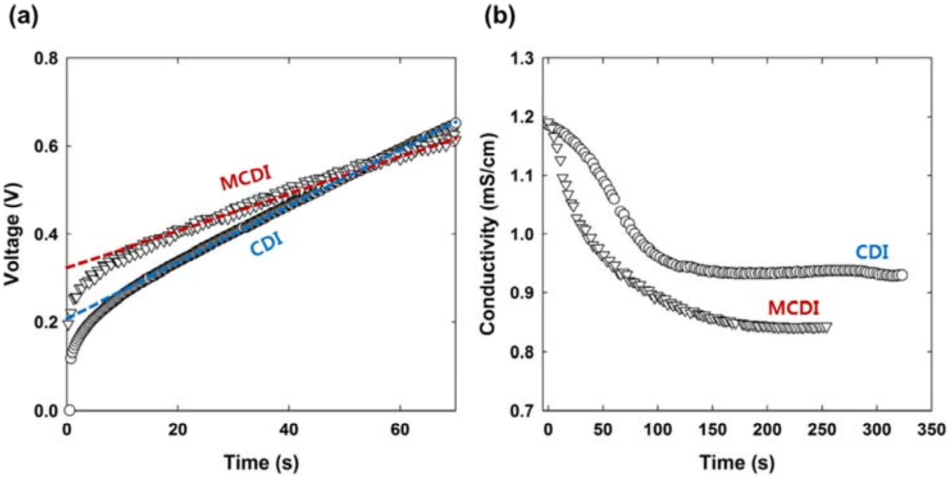

Figure 2-2. Comparison of (a) electrochemical and (b) deionization performance between CDI and MCDI.

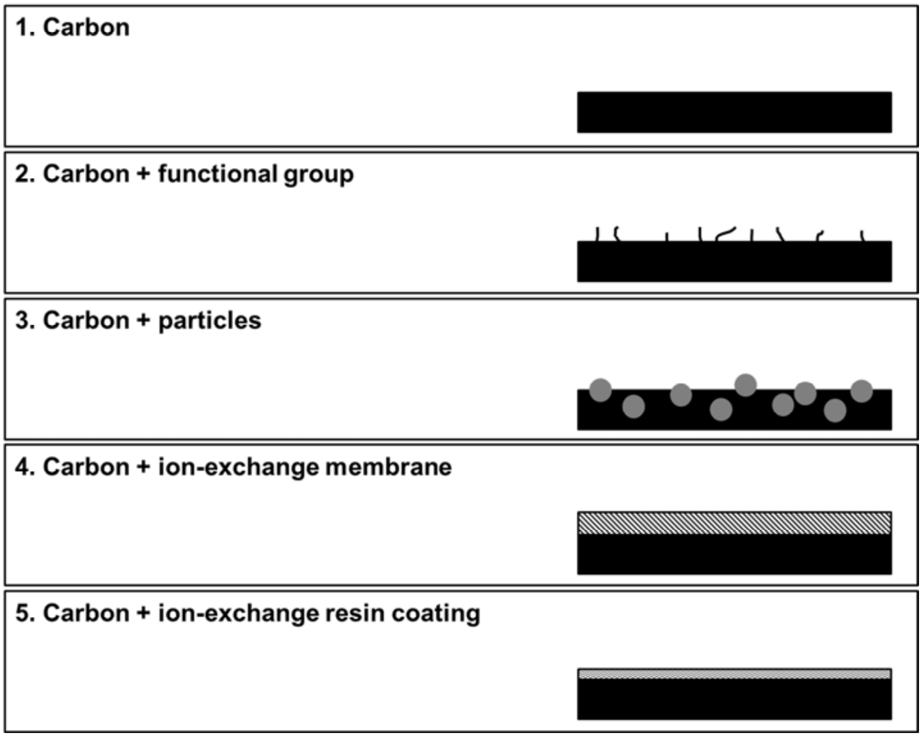

Figure 2-3. Classification of carbon electrode.

Various operating parameters were investigated by Zhao et al. in which effects of salt concentration, charging current, flow rate, and desorption time on water recovery, salt adsorption capacity, and average salt adsorption rate were reported [17]. As explained above, MCDI only allows for transport of counter-ions and the selective transport could enable reverse current and reverse voltage desorption. Therefore, effects of desorption current, desorption voltage, and desorption time on salt adsorption capacity and average salt adsorption rate could be examined. These operating variations also affected energy consumption during deionization [39]. MCDI was more favorable than CDI in terms of consumed energy per ion removed. When compared adsorption and desorption methods, constant current adsorption and zero voltage desorption used less energy than constant voltage adsorption and zero reverse current desorption. In addition, model equations could be used to describe these performances [34]. Investigations on the composition of a feed solution were reported with various ionic species. Zhao et al. observed that a solution consisting of NaCl and $CaCl_2$ shows time-dependent ion selectivity; initially adsorbed sodium ions were gradually replaced by calcium ions [50]. Selectivity of ions was compared focusing on cations [51], anions [38], and specific ions [41]. Moreover, CDI could be utilized to remove specific ions such as acetic acid, sulfuric acid [40], and copper ions [52].

Most of CDI studies have been carried out in a typical configuration in which sheet-type electrodes are assembled with current collectors and a spacer (see Fig. 2-4(a)). Ion-exchange membranes/resins are placed between an electrode and a spacer for MCDI (Fig. 2-4(b)). A feed solution is supplied to CDI module and it passes between the electrodes through the spacer. The effluent can be recirculated (batch mode) or wasted (single-pass mode). Recently, new designs have been proposed which would be the future of CDI. Porada et al. suggested wire-type electrodes by coating activated carbon on the surface of graphite rods followed by ion-exchange resin coating [53]. This could serve as a mobile electrode bundle which allows for deionization of reservoir instead of pumping the solution to the CDI module. Repetitive cycles of charging and discharging between two reservoirs produced diluted and concentration solutions. Another new design, flow capacitive deionization (FCDI), showed a big leap converting conventional transient deionization to steady process. This novel design was firstly reported by Jeon et al. where steady deionization was demonstrated with carbon slurry electrodes [22]. As described in Fig. 2-5, FCDI module consisted of three channels; two channels were for carbon slurry electrodes in contact with current collectors and another channel for a feed solution was located in between. Three channels were separated by ion-exchange membranes which only allows for transport of ions. Compared to the conventional CDI, it did not require discharge step to release ions in the electrode because fresh carbon slurry electrodes were continuously supplied to the FCDI module. Therefore, the effluent with a steady conductivity profile was produced, even for a high salt concentration (32.1 g/L) close to seawater. Sequel studies have been reported investigating energy recovery [54], no ion-exchange membrane design [55], and operating parameters [56].

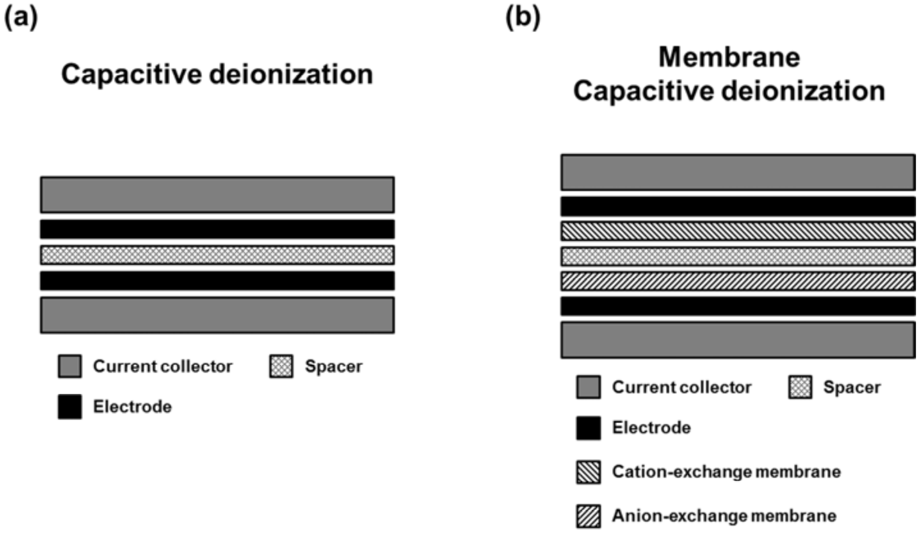

Figure 2-4. Cell configuration of (a) capacitive deionization and (b) membrane capacitive deionization.

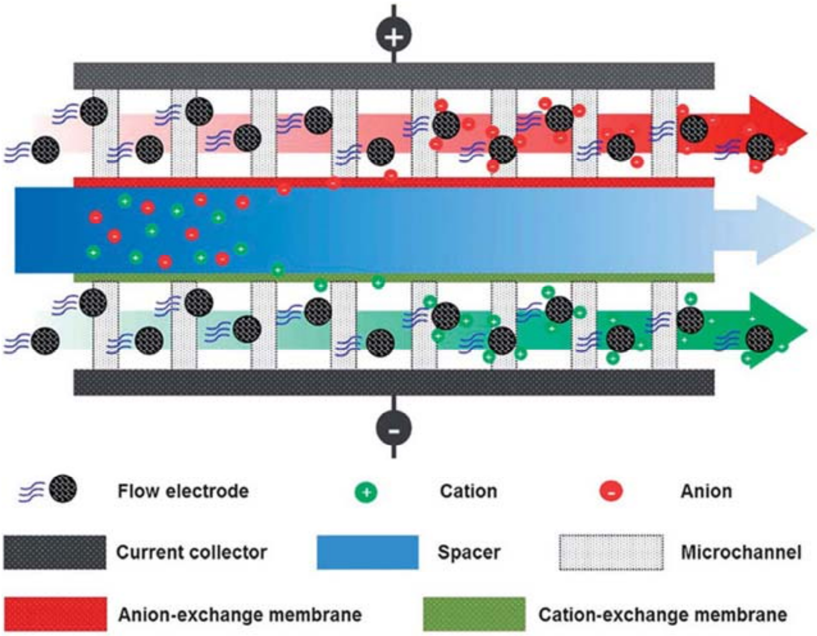

Figure 2-5. Schematic diagram of FCDI cell configuration [22].

2.2. Carbon fibers

Carbon fiber is made from carbon precursor which is in the form of fiber and it retains the structure after the carbonization and/or activation. Compared to the powdered carbons, carbon fibers do not need a polymer binder to be used as an electrode because they are connected. Therefore, electrical conductivity can be greatly improved, which is unique and advantageous properties of this material. In particular, the fiber network could enable facile access of water [57]. This is especially beneficial for CDI applications because inherent hydrophobic property of a carbon and polymer binder can be overcome while keeping its electrochemical properties (see Fig. 2-6). Its unique structure also allows water to penetrate the electrode. A Feed solution passes *between* carbon sheet electrodes in a conventional CDI configuration, but with a carbon fiber electrode, a feed solution can pass *through* the electrodes. Boron removal could be possible if it is properly used during deionization. Because of uncharged state of boron in the neutral pH (boric acid, $B(OH)_3$), its removal is quite difficult in conventional desalination processes such as RO. CDI is suitable to remove charged ionic species in a solution, thus removal of uncharged boric acid is possible only when it is transformed to charged state in an increased pH condition. However, flow-through configuration could enable boron removal without additional treatment to increase pH [58]. If a feed solution containing boric acid firstly passes through a negative electrode, boric acid changes to borate ($B(OH)_4^-$) due to increased pH near the negative electrode. Afterwards, the solution containing borate passes through a positive electrode and leaves the CDI cell. Negatively charged borate could be attracted to positively-biased electrode and thus cannot leave the cell. Detailed process for boron removal in CDI is described in Fig. 2-7.

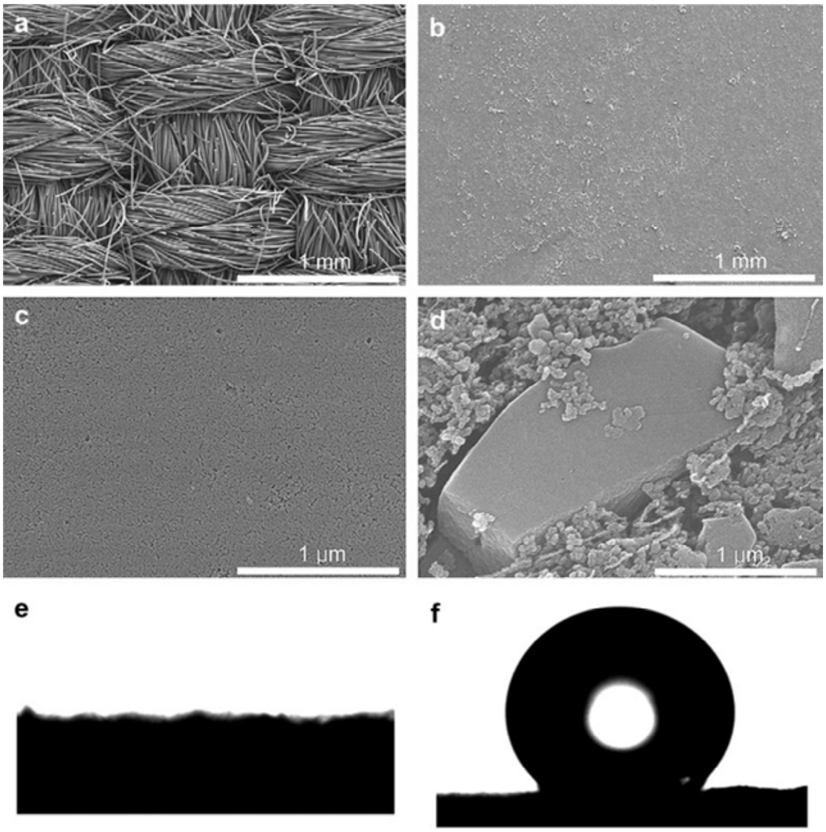

Figure 2-6. SEM images of (a-c) carbon cloth and (d) activated carbon composite electrode. (e) Contact angles of carbon cloth and (f) activated carbon composite electrode [57].

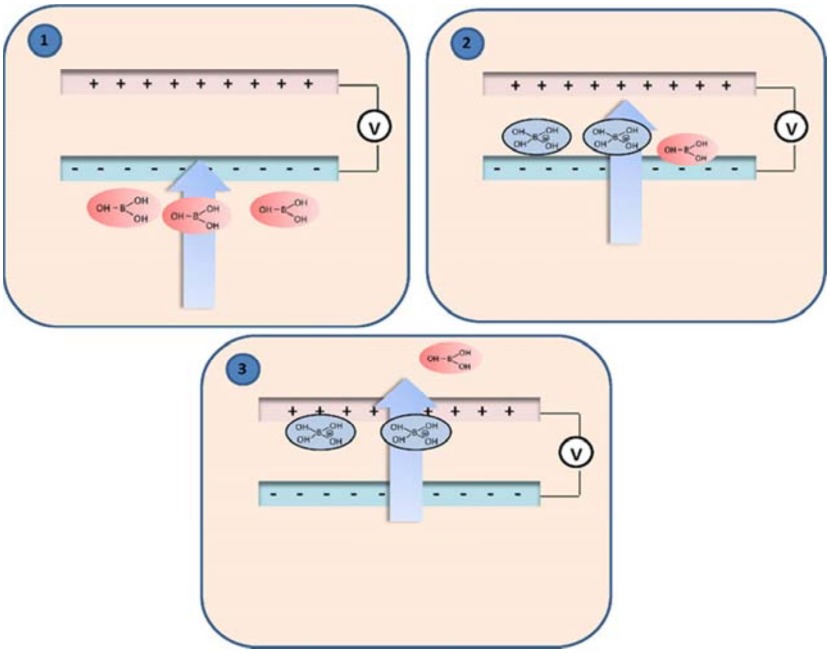

Figure 2-7. Schematic diagram for boron removal steps in CDI [58].

For the general deionization, carbon fibers can be modified by grafting metal oxides or introducing functional groups onto the electrode surface to enhance the performance. Metal atoms can be incorporated to carbon fibers by the reaction of metal alkoxide and hydroxyl group of the carbon surface, thus forming M-O-C bonds. In this way, titania could be incorporated to activated carbon cloth and the deionization performance was greatly enhanced [59]. Such grafting was also possible with various metal atoms including Zr, Si, and Al, but Ti was more beneficial than the others [60]. Moreover, metal oxide nanoparticles could be simply incorporated by dipping the electrode in colloidal solution followed by hydrothermal reaction [61]. The enhancement could be partly explained by electron-hole generation under electric field. It could be also due to inherent surface charge of metal oxides depending on the pH of a solution. When this behavior is properly applied to CDI, asymmetric electrodes could be fabricated to more efficiently attract counter-ions [16, 62, 63]. In addition, surface charge could play a role to enhance the hydrophilicity. Functional groups can be simply introduced by chemical modification with KOH or HNO_3 [12, 64]. Membrane-assisted configuration was also possible, which is known as the first MCDI research paper [65]. Besides, a large number of studies have reported the performance carbon fibers made by electrospinning. This technique allows for various strategies to combine other materials or to realize unique structure. It can be activated to increase the surface area after carbonization of carbon precursor by using CO_2 [66], KOH [67], and $ZnCl_2$ [68]. Adding carbon black [6] or graphene oxide [69] to carbon precursor and subsequent electrospinning, heating, and carbonization could realize unique carbon fiber network with outstanding performance. Similar strategy was also introduced to develop multi-channel carbon fibers. PMMA (poly(methyl methacrylate)) nanoparticles in carbon precursor transformed to nanofibers during electrospinning, and they are decomposed with carbonization, thus leaving nano-sized channels in carbon fibers structure [70, 71].

2.3. Carbon aerogels

Aerogel is a substance that is derived from a sol-gel process and subsequent drying process (under supercritical or ambient atmosphere) without collapsing its integrated network. Carbon aerogel can be produced by carbonization of aerogel, thus unique physical properties of the aerogel such as interconnected structure, high porosity, and high surface area are also available in the carbon aerogel together with electrical conductivity. Its application to deionization was firstly reported by Farmer et al. in Lawrence Livermore National Laboratory (LLNL), initiating prosperity of CDI. Their pioneering works have been carried out using resorcinol-formaldehyde (RF) aerogel infiltrated carbon paper and subsequent carbonization. Resulting carbon aerogel composites (CACs) were attached to titanium plate current collectors. Fundamental studies were carried out using various ions such as NaCl, $NaNO_3$ [72], and NH_4ClO_4 [73]. Hazardous chromium ions were also possibly removed, though it is not based upon simple double-layer charging [74]. A detailed and comprehensive study was reported later [4], where the effect various parameters including types of ions, operating voltage, and carbonization conditions on deionization performance was discussed. Furthermore, a target was extended beyond synthetic solutions. Colorado River water was tested with and without natural organic matter (NOM); a proper pretreat for NOM removal was recommended to prevent the performance degradation. Carbon aerogel can also be combined with other materials to enhance the deionization performance. Titania [75] was one of them as in the other carbon materials and silicagel incorporation was also reported [76]. When carbon aerogel is combined with SiO_2 by sol-gel dip-coating method, especially a negative electrode, potential of zero charge could be modified and better charge efficiency was acquired [77]. A novel method allowed homogeneous deposition of metal oxides into carbon aerogel [78]. For this, RF gel was mixed with metal oxide precursors ($Mn(NO_3)_2$ or $Fe(NO_3)_2$) followed by supercritical drying and carbonization. The resulting carbon aerogel could contain MnO or Fe_3O_4 inside the carbon network. The metal oxides provided pseudo-capacitive property to carbon aerogel, thus composite electrodes showed enhanced deionization performance. Pore structure could be controlled by adjusting compositions of RF gel during sol-gel process. RF-gel to catalyst (Na_2CO_3) ratio (R/C ratio) [79] or RF wt% [80] substantially affected the pore structure of resulting carbon aerogels (see Fig. 2-8). Additional activation process could greatly increase surface area from typical range (~700 m^2/g) to more than 2,000 m^2/g [81]. Because deionization performance is strongly dependent on the surface area of a carbon material, CO_2-activated carbon aerogel showed enhanced performance. Moreover, such activation process could enable to realize unique pore structure consisting of various pore sizes, hierarchic pore structure [82]. High porosity of this monolithic carbon aerogel allowed penetration of a solution, thus deionization was conducted in a flow-through configuration with outstanding performance.

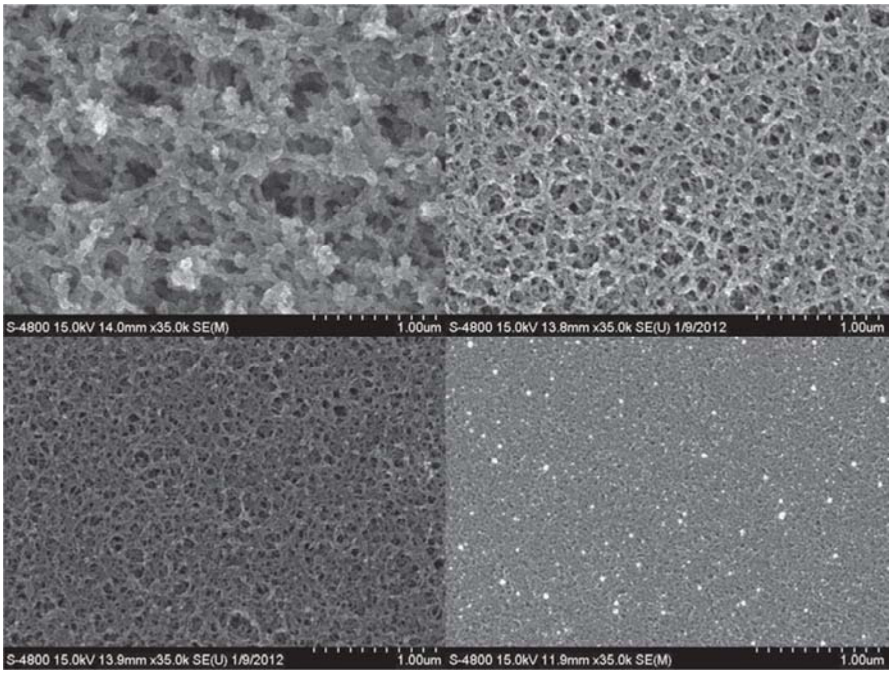

Figure 2-8. SEM images of carbon aerogels synthesized under various RF wt%.

2.4. Ordered mesoporous carbons

There are three types of pore depending on the size: micropore (<2 nm), mesopore (2–50 nm), and macropore (>50 nm). Ordered mesoporous carbon (OMC) mainly consists of mesopores with ordered configuration (see Fig. 2-9). This ordered and mesoporous structure can be realized by two strategies. The first one is called hard templating method. In this method, *hard* mesoporous template with ordered structure such as silica is impregnated with carbon precursors followed by polymerization and carbonization. After dissolving the template, only un-dissolved carbon remains with ordered structure. Another strategy is soft templating method, where *soft* copolymer and carbon precursors are involved to form mesoporous structure and thus, additional template removal is unnecessary. These strategies provide easy and inexpensive synthetic method to develop carbon materials with tailored mesopore size. More importantly, ordered pore structure allows for rapid transport of ions inside pore structure, improving rate performance of carbon-based energy storage devices as well as CDI. Therefore, it could exhibit better deionization performance compared to microporous activated carbon with similar surface area, because facile ion transport was possible inside mesopores [83]. The effect of additional modifications on deionization performance was investigated on OMCs [14]; functional groups on carbon surface could be impregnated or removed by H_2O_2 solution or pyrolysis under N_2 atmosphere. The performance was enhanced with

H_2O_2 and subsequent functional group impregnation, while functional group removal deteriorated the performance. Involving nickel salt to mesoporous silica template could lead to various pore structures of OMCs [84]. The resulting OMC showed higher surface area and better deionization performance. An attempt to improve the synthetic procedure of OMC was made to exclude a toxic chemical compound, which is formaldehyde [85]. Glyoxal was used as an alternative of formaldehyde and a similar performance was obtained. OMCs derived from soft-template method were also prepared with physical/chemical activation [86] and for further CDI applications [5]. MnO_2 could be incorporated to OMC, providing Faradaic reactions [87]. In addition, hierarchically porous structure was realized with addition of SiO2 microspheres during OMC synthesis and their removal after carbonization [88].

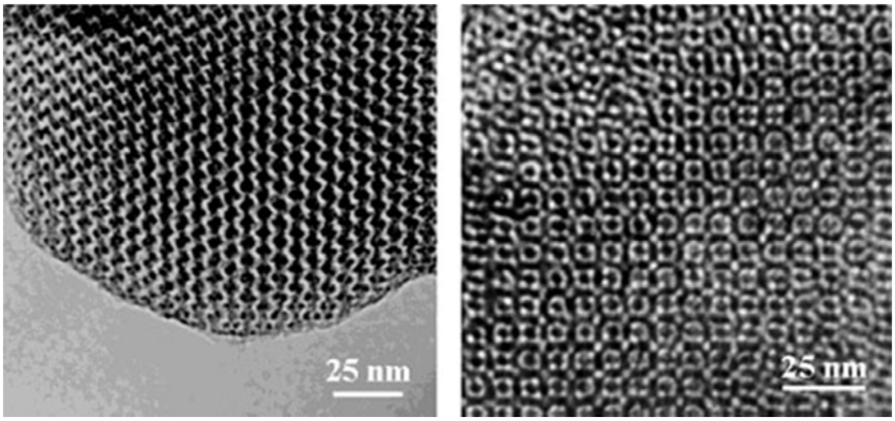

Figure 2-9. TEM images of CMK-1 and CMK-2 [89].

2.5. Carbon nanotubes

Various CDI studies have been reported by using carbon nanotubes (CNTs) as an electrode material in order to make use of their excellence electrical property. Initial studies have focused on simple applications of CNTs prepared by commercial products [90], chemical vapor deposition [9], and electrophoretic depositions [91, 92]. However, the CNT-based CDI electrodes showed poor deionization performance compared to that of carbon electrodes reported in other studies including activated carbons. Unexpected results would be ascribed to unfavorable CNT arrangement inside the electrode, leading to retarded access of a solution and low surface area. Afterwards, many attempts have been made to enhance the deionization performance by combining with various additives. One of them was to modify CNTs by sulfonation or amination, thus functional groups could aid the deionization due to their inherent charges under experimental condition [93]. To introduce such charges to the electrode while maintaining the carbon surface, functional group-impregnated polymers were incorporated when fabricating electrodes by casting [94, 95] or electrophoresis [96]. Furthermore, MnO_2 could improve deionization performance, in which sodium ions can be intercalated [97].

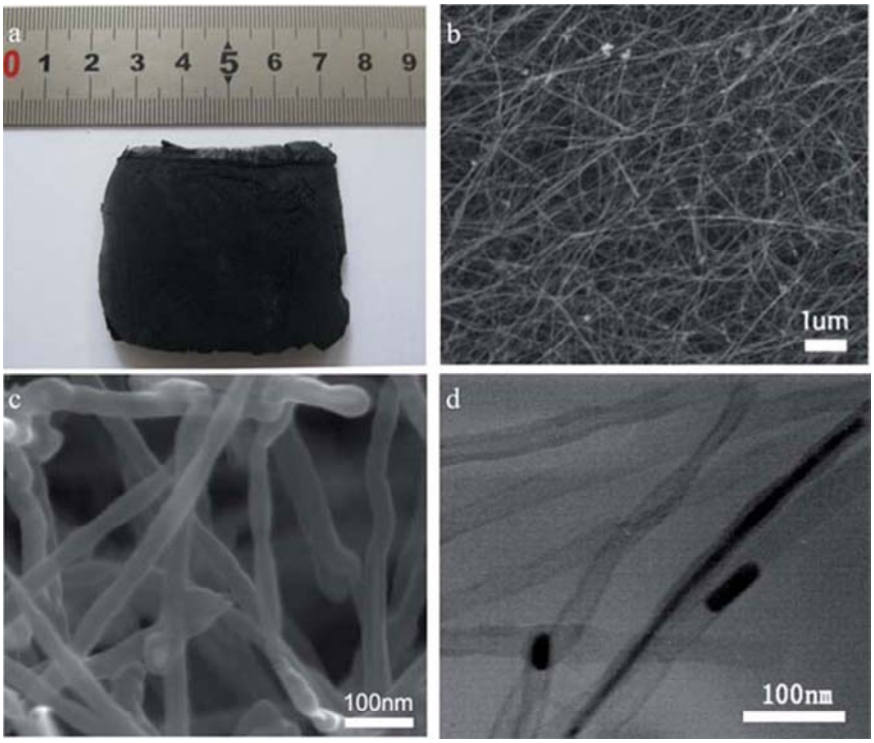

Figure 2-10. Various images of carbon nanotube sponges made by chemical vapor deposition (CVD) [9].

2.6. Graphene

With growing attention of graphene as a promising electrode material due to its outstanding electrical properties, there has been numbers of studies to investigate deionization performance of graphene electrodes. The first study applying graphene electrode to CDI was reported by Li et al. [7], where graphene-like nano flakes (GNFs) were prepared by modified Hummer's method. When compared to activated carbon (989 m^2/g), its surface area was quite low (222 m^2/g). Interestingly, better deionization performance was achieved with GNFs; its interlayer structure allowed facile access of ions, thus providing more effective surface area (see Fig. 2-11). This electrode was also utilized to remove ferric ions in an aqueous solution [98]. Though GNFs showed outstanding deionization performance in CDI, the most significant issue when utilizing such electrode is to prevent aggregation during the synthesis. Normally, graphene can be prepared by modified Hummer's method. Firstly, graphite is exfoliated to detach graphene layers by using strong acids. The exfoliated products are in the form of graphene oxide, thus further chemical reaction is required to reduce graphene oxide. Therefore, reduced graphene oxide (rGO) is appropriate expression rather than graphene when it is synthesized by the modified Hummer's method. However, the reduction process brings undesirable aggregation of rGO, leading to severe decrease in surface area. To utilize theoretical surface area of graphene (~2,675 m^2/g), various strategies were suggested to prevent aggregation. One of them was adopted when preparing rGO electrodes for CDI, in which pyridine was added to GO solution to inhibit the aggregation and to increase dispersity [99]. Sulphonation of GO also could prevent the aggregation [100]. More effective strategy with high-performance CDI was reported by Yin et al. [15], where graphene/metal oxide nanoparticle hybrids were prepared via a novel synthetic procedure. To prepare graphene aerogel/TiO_2 (GA/TiO_2), $TiCl_3$ and NH_3 were mixed with a graphene oxide aqueous solution followed by hydrothermal treatment at 180^oC for 12 h and subsequent freeze-drying. High pH condition and the location of TiO_2 nanoparticles during hydrolysis allowed GA/TiO_2 hybrids to have open-pore structure. This unique structure and TiO_2 nanoparticles played an important role to show outstanding deionization performance. More simple method to prepare graphene with high surface area was realized by using the sponge as a template [8]. It was achieved by immersing the sponge to a GO solution followed by annealing under inert atmosphere. The resulting electrode showed better performance graphene electrode without TiO_2.

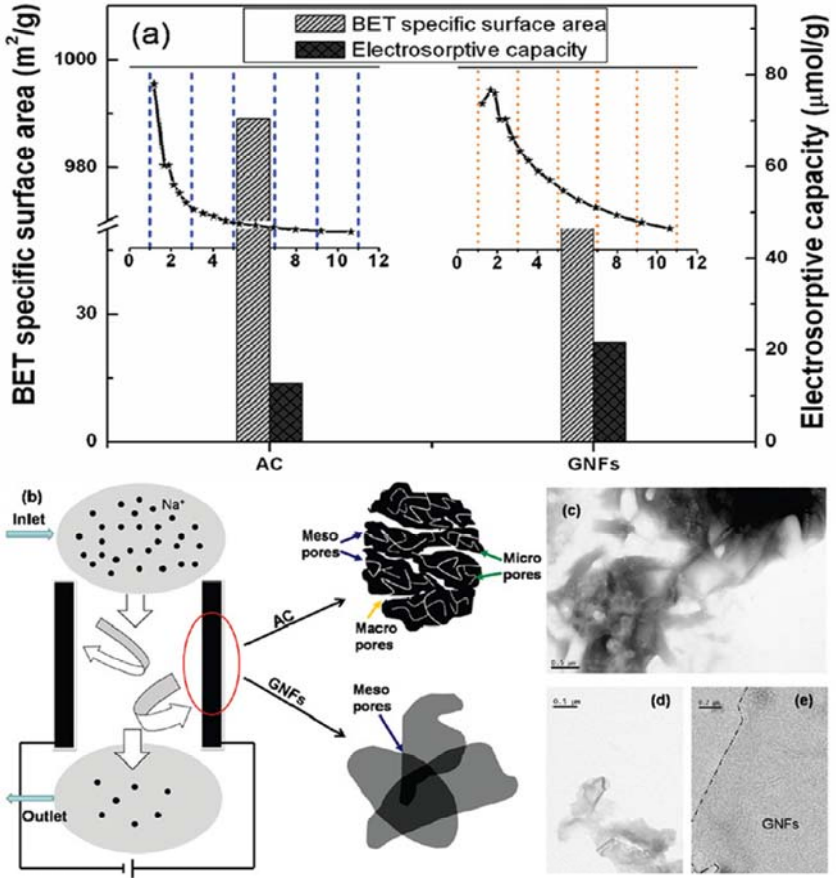

Figure 2-11. Comparison of activated carbon and GNFs in relation to their BET surface area, deionization performance, and pore structure [7].

2.7. Carbon/carbon composites

Combination of two different carbon materials can result in performance enhancement by complementing each property. For example, CNTs were used to increase the electrical conductivity of OMCs [101, 102]. Also, rGO could help to reduce the resistance of activated carbon fiber when electrospinning was conducted with rGO containing carbon precursor [103]. Another approach is to incorporate other carbon materials to prevent the aggregation of rGO. As explained in the graphene part, the aggregation led to severe performance decrease. Effective incorporation of carbon materials such as mesoporous carbon [104], CNTs [105, 106], and activated carbon [107] could prevent restacking of rGO, thus providing open pores to carbon/carbon composite. Furthermore, CNT could be grown onto carbon fiber surface [108] and simple mixture of carbon aerogel/activated carbon was also reported [109].

2.8. Novel carbon materials

With recent progress in carbon synthetic method, novel carbon materials have developed and their applicability has evaluated in various fields such as hydrogen storage, energy storage device, and CDI. One of novel carbon is called carbide-derived carbon (CDC), containing regular micropores which can be controlled by adjusting synthetic condition. As one can notice from its name, its precursor is carbide. Carbide is a compound consisting of carbon with metallic substance such as silicone or titanium. Carbon and metal in carbide has regular structure; thus, regular microporous carbon can be obtained by extracting metals from its structure by chlorination at high temperature [110]. Because of its tunable and ultra-fine pores, interesting results have been reported when applied to supercapacitor. In CDI, the similar result was also reported [111]. CDC with pore size approximately 0.75 nm was synthesized and used as CDI electrodes. The result showed that CDC could exhibit better deionization performance in terms of capacity even though CDC had a lower surface area compared to activated carbons. In a sequel study [10], three CDCs were prepared: TiC-CDC, OM SiC-CDC, and HIPE SiC-CDC. TiC-CDC had only micropores; OM SiC-CDC had micro- and mesopores; HIPE SiC-CDC had micro-, meso-, and macropores. From the CDCs with different pore structure, direct prediction could be possible only from pore size distribution analysis. They suggested that pore provides different contribution depending on its size. Another novel carbon materials is MOF-derived carbon (MDC). Metal organic framework (MOF) is a compound with regular structure consisting of metals and organic molecules [112]. It was reported by Yang et al. that hierarchically porous carbon can be achieved by carbonization of MOF [113]. To make use of its hierarchic pore structure in CDI, MDC was prepared (see Fig. 2-12) and its deionization performance was investigated [11]. When compared to activated carbon (microporous carbon) and carbon aerogel (meso- and macroporous carbon), MDC exhibited rapid deionization performance due to its unique porous structure.

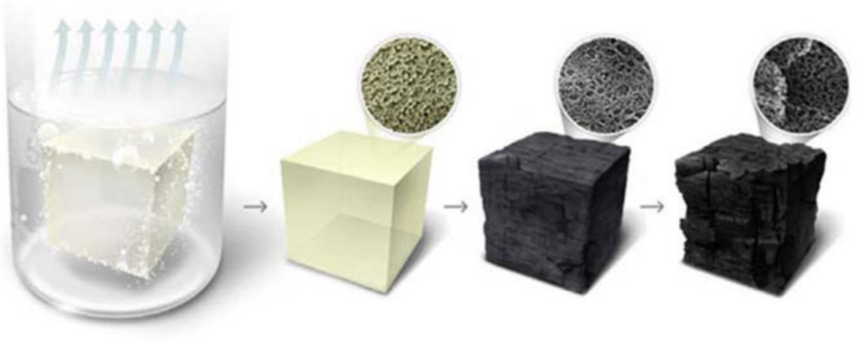

Figure 2-12. Schematic diagram to synthesize MDC.

Table 2-1. Deionization (salt adsorption) capacity (mg/g) of various carbon materials.

Year	Carbon	Voltage (V)	Concentration (mg/L)	Capacity (mg/g)	Ref.
1996	Carbon aerogel	1.2	47	1.7	[72]
2008	Ordered mesoporous carbon	1.2	25	0.7	[83]
2009	Activated carbon	1.2	292 1167	10.9 13.0	[25]
2010	Reduced graphene oxide	2.0	25	1.4	[7]
2011	Ordered mesoporous carbon	1.2	3970	14.6	[5]
2011	Carbon nanotube sponge	1.2	60	4.3	[9]
2012	Carbon nanotube	1.2	23	1.0	[91]
2012	Carbon aerogel	1.5	5844	10.2	[82]
2012	Carbon fiber	1.6	90	4.6	[66]
2012	Carbon fiber/carbon black	1.6	90	9.1	[6]
2012	Carbide-derived carbon	1.2	292	12.4	[111]
2012	Reduced graphene oxide /sulphonation	2	250	8.6	[100]
2012	Reduced graphene oxide/activated carbon	1.2	50	2.9	[107]
2013	Activated carbon	1.2	584	13.6 7.0 6.2 4.1	[24]
2013	OM SiC-CDC HIPE SiC-CDC TiC-CDC	1.2	292	12.8 11.1 10.1	[10]
2014	Carbon aerogel	1.5	1460	5.4	[79]
2014	Carbon fiber/reduced graphene oxide	1.2	450	13.2	[69]
2014	Carbon fiber	1.2	500	10.5	[68]
2014	Ordered mesoporous carbon/H_2O_2 modification	1.2	100	7.6	[14]
2014	Sponge templated reduced graphene oxide	1.5	50	5.0	[8]
2014	Carbon nanotube/PVA	1.2	58	13.0	[94]
2014	Reduced graphene oxide/Carbon fiber	1.2	95	7.2	[103]
2014	MOF-derived carbon	1.2	584	11.2	[11]

3. Deionization Capacity in Capacitive Deionization

3.1. Relationship between Capacitance of Activated Carbon Composite Electrodes Measured at a Low Electrolyte Concentration and Their Deionization Performance in Capacitive Deionization

3.1.1. Introduction

Water scarcity is one of the most urgent environmental problems that have to be solved for sustaining our life. Unfortunately, this problem is expected to be intensified with population growth and subsequent increase in water demand for agricultural, industrial, and domestic purposes. The increase in water demand, especially fresh water, is estimated to be roughly 64 billion cubic meters per year [114]. From a technical point of view, one way of meeting this increased water demand will be the deionization of saline water which accounts for 97% of water on Earth [115]. Deionization processes such as thermal distillation, reverse osmosis (RO), and electrodialysis (ED) have all been utilized to achieve this goal.

Recently, capacitive deionization (CDI) has attracted growing attention as a novel deionization process. CDI removes ionic species in saline water by applying an electric potential to porous electrodes, and has several advantages over conventional deionization processes, including efficient energy use, eco-friendliness, and a high recovery rate [4, 116, 117]. In this process, porous electrodes play a key role in deionization, as ionic charges are captured by the pore structure of the electrode. Carbon has been recognized as a suitable electrode material for CDI due to its high specific surface area. Because of this, various carbon electrodes, including carbon aerogel, graphene, and carbide-derived carbon, have been utilized in CDI [7, 82, 90, 111].

An electrode material for CDI requires outstanding electrochemical behavior as well as a high specific surface area. Capacitance is an ability of an electrode to store charges, which is an essential requirement for operating CDI; thus, it has been considered to be the most important parameter for CDI electrodes among various electrochemical properties. Activated carbon is one of electrode materials exhibiting high capacitance. Moreover, it is competitive over other carbon materials from an economic point of view, so that they have been widely investigated as a CDI electrode [23, 111, 118]. However, a quantitative correlation between capacitance of activated carbons and their deionization performance remains unclear, especially at low electrolyte concentrations. Several studies have reported CDI performance and capacitance values in various electrolyte concentrations [5, 17, 34, 39, 83, 105, 119], but further investigation is required to understand how capacitance of electrodes at low electrolyte concentrations affects deionization performance.

In this study, we investigated the deionization performance of various activated carbon composite electrodes with diverse capacitance values in order to examine their deionization performance in relation to capacitance. Concentration-dependent capacitance was evaluated at various electrolyte concentrations. In particular, capacitance at a low electrolyte concentration was converted to charge capacity to compare with deionization capacity obtained in CDI operation.

3.1.2. Experimental

Materials. Four commercially available carbon powders were provided by Norit (S-51HF and SX PLUS), Japan EnviroChemicals (YS-2), and Kansai Coke and Chemicals (MSP-20). The resistivity of carbon powders was determined by utilizing the four-probe van der Pauw method [120]. To obtain this measurement, a round-shape homemade reactor with four probes located at the bottom was fabricated and carbon powders were pressed (~700 kgf/cm^2) after installation. Nitrogen adsorption/desorption (at 77 K) was carried out using a Micromeritics ASAP2010 and specific surface area (SSA) was determined according to the Brunauer- Emmett-Teller (BET) equation.

Electrode preparation. Carbon composite electrodes were prepared by mixing 86 wt% carbon powder, 7 wt% carbon black (Super P, Timcal), and 7 wt%

polytetrafluoroethylene (PTFE, Aldrich). This mixture was consistently kneaded with a few ml of ethanol for homogeneity and pressed using a roll press machine (electrode thickness of ~300 μm). The fabricated carbon composite electrodes were dried in a vacuum oven at 120°C for 12 h. After drying, the electrodes were cut into round pieces (18 mm in diameter) and larger round pieces (50 mm in diameter) with a 4-mm-diameter hole located at the center for electrochemical characterization and deionization performance evaluation, respectively.

Electrochemical characterization. The electrochemical properties of carbon composite electrodes were analyzed using cyclic voltammetry (CV) and galvanostatic charge/discharge tests. An electrochemical cell was manufactured with graphite current collectors (18 mm in diameter) and cellulose nitrate (thickness of ~110 μm, pore size = 0.45 μm, Advanced Microdevices, India) was used as a separator. CV was performed in a three-electrode configuration with 1 M NaCl as an electrolyte; two carbon composite electrodes were used as a working and as a counter electrode and a conventional KCl-saturated Ag/AgCl electrode (Princeton Applied Research, USA) was used as a reference electrode. Potential was applied using a PARSTAT 2273 (Princeton Applied Research, USA) in the range of 0.0 to 0.6 V with a scan rate of 2 mV/s. Capacitance of an electrode was obtained according to Eq. (1),

$$C = i/v\, m \qquad (1)$$

where C (F/g) is the specific capacitance, i (A) is the current, v (V/s) is the scan rate, and m (g) is the mass of an electrode. Average values in the voltage range (0-0.6 V) were used as the specific capacitance.

Galvanostatic charge/discharge tests were conducted in a two-electrode configuration with a pair of carbon composite electrodes. Voltage profiles were obtained at a current density of 0.5 mA/cm^2 with different electrolyte concentrations (0.01, 0.1, and 1 M NaCl) in the potential range 0.0–0.4 V. Discharging voltage profile was used to determine specific capacitance according to Eq. (2) [121],

$$C = 2i\Delta t/m\Delta V \qquad (2)$$

where C (F/g) is the specific capacitance, i (A) is the current, Δt (s) is the discharging time, ΔV (V) is the potential difference in the discharging step, and m (g) is the mass of an electrode.

Deionization performance. Fig. 3-1 shows a schematic diagram of the CDI system used in this study. The CDI module was constructed with a pair of carbon composite electrodes, a pair of graphite sheets as a current collector (thickness = 220 μm), and nylon as a spacer (thickness = 200 μm). The system was operated in a single-pass mode (fresh feed solution continuously went through between electrodes, see Fig. 3-2) and the experiment was carried out in a temperature chamber (KCL-2000, EYELA, Japan) at 25°C. A feed solution (10 mM NaCl) was supplied to the CDI module with a flow rate of 10 ml/min using a peristaltic pump (Gilson, Inc., USA). Constant voltages of 1.2 V and 0 V (each for 10 min) were applied to the CDI module using a cycler (WBCS3000, WonATech, Korea) for charging and discharging, respectively. During the operation, outlet conductivity was continuously monitored using a flow-type conductivity meter (3573-10C, HORIBA, Japan). All experiments were triplicated to assess reproducibility.

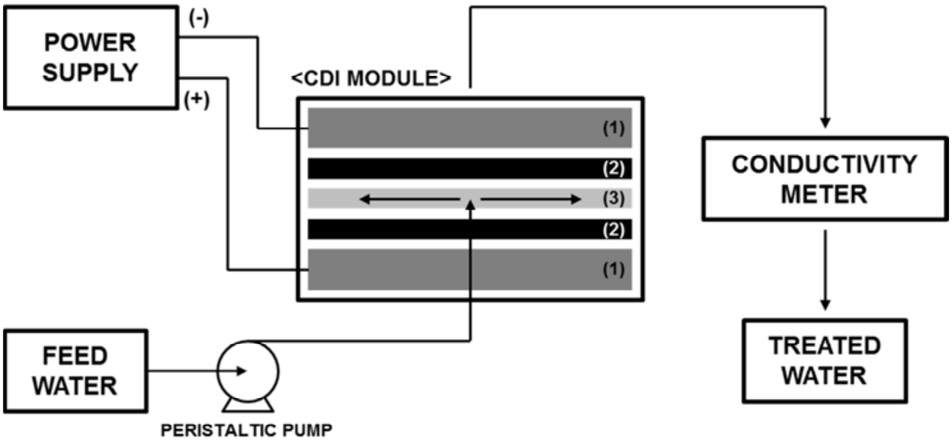

Figure 3-1. Schematic diagram of the CDI system. The CDI module consists of (1) two pairs of graphite sheets, (2) two pairs of carbon composite electrodes, and (3) nylon as a spacer. Feed solution (0.01 M NaCl) was supplied to the CDI module using a peristaltic pump (10 ml/min). Meanwhile, voltage (1.2 V) was applied and conductivity of an effluent was continuously monitored using a flow-type conductivity meter.

Comparison between batch and single-pass operational modes. Fig. 3-2 illustrates schematic diagrams of two representative operational modes in CDI, which are batch and single-pass modes. In the batch mode CDI (Fig. 3-2(a)), a recirculated feed solution is supplied to CDI module and it conductivity is recorded over time. The conductivity levels off when the electrodes are saturated with charging; the difference between initial and final conductivity (denoted by the arrow) becomes deionization capacity. To observe the conductivity change, small amount of feed solution is required. This mode is simple to prepare experimental setups and interpret the result, but its experimental condition cannot be clearly defines as the concentration changes during the operation. In the single-pass mode CDI (Fig. 3-2(b)), fresh feed solution is continuously supplied to the CDI module and effluent conductivity is recorded over time. The effluent conductivity initially decreases and turns back to the influent conductivity with charging and subsequent saturation of the electrodes. In this case, the area between influent and effluent conductivity (denoted by dashed lines) corresponds to the deionization capacity. Compared to the batch mode CDI, its experimental setup is complex because the effluent needs to be directly connected to a flow-type conductivity meter. However, single-pass CDI mode is quite similar to practical CDI system and concentration-dependent performance can be clearly defines because a fresh feed solution is supplied.

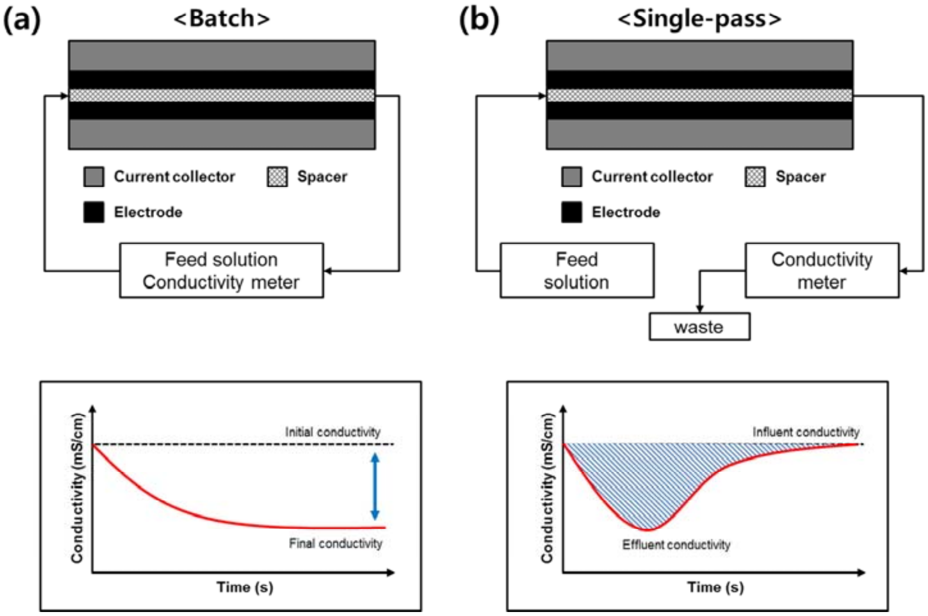

Figure 3-2. Comparison between batch and single-pass operations.

3.1.3. Results

Characterization of carbon materials and composite electrodes. The basic physical properties of the activated carbon powders used in this study are summarized in Table 3-1. The resistivity of the carbon materials ranged from 0.07 to 0.21 Ωcm, where MSP-20 and YS-2 showed the lowest and highest values, respectively. In pore structure analysis, the carbon materials were found to have pore volumes of 0.61–0.96 cm^3/g and specific surface areas range between 630–2266 m^2/g. The increase in specific surface area was mainly due to the development of the micropore; the micropore ratio was only 43% for S-51HF, which has the lowest specific surface area, but it increased up to around 80% for the MSP-20, which has the highest specific surface area.

Table 3-1. Characterization of activated carbons.

	S-51HF	SX PLUS	YS-2	MSP-20
Resistivity (Ωcm)	0.19±0.002	0.14±0.003	0.21±0.001	0.07±0.001
Pore volume (cm^3/g) [a]	0.61	0.71	0.79	0.96
BET surface area (m^2/g) [b]	630	1095	1705	2266
Micropore area (m^2/g) [c]	268	701	1234	1753
Ratio [d]	0.43	0.64	0.72	0.77
Mesopore area (m^2/g) [e]	362	394	471	513

[a] $P/P_0 = 0.95$

[b] $P/P_0 = 0.01\text{-}0.1$

[c] Calculated from t-plot analysis

[d] Micropore area/BET surface area

[e] Mesopore area (>2 nm) = BET surface area – micropore area

Fig. 3-3 shows CV curves of five carbon composite electrodes, where current profiles were converted to a specific capacitance by dividing with the scan rate and the mass of electrodes. As shown in Fig. 3-3, all the curves exhibit rectangular shape profiles, suggesting that the carbon composite electrodes behave like fairly ideal capacitors. From this result, one could expect that the electrodes would be able to deionize saline water by a capacitive double layer effect. As a result, the specific capacitance of electrodes were 44 (S-51HF), 63 (SX PLUS), 81 (YS-2), and 124 F/g (MSP-20). Interestingly, higher capacitance was obtained with increasing BET surface area. However, it should be noted that this relationship is valid only when entire pores of the carbon materials could be used as charge storage sites. In other words, a carbon material of high surface area cannot exhibit corresponding capacitance unless the pores can be approached by ionic charges (see Fig. 3-4).

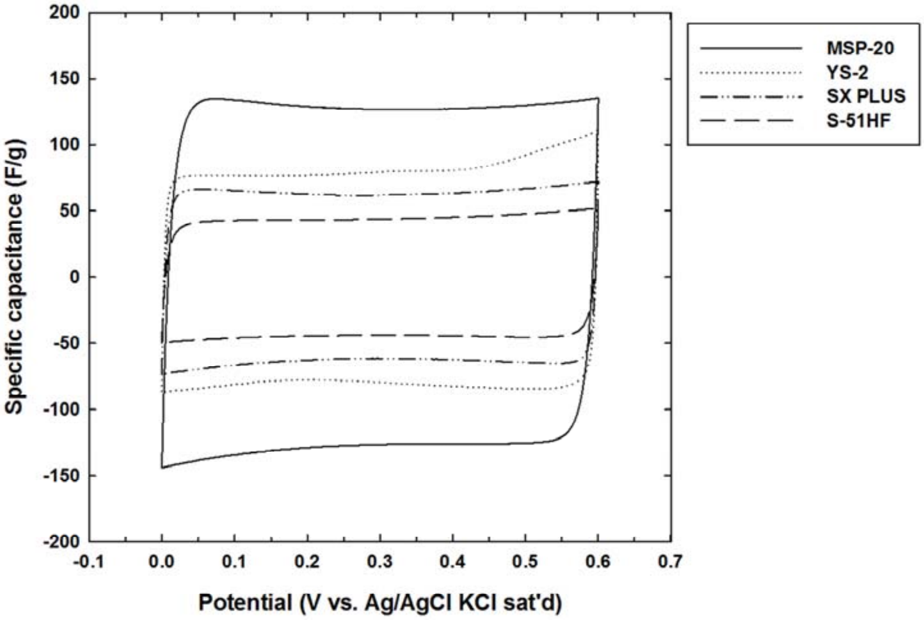

Figure 3-3. CV curves of carbon composite electrodes used in this study. The specific capacitance was obtained by dividing current by the scan rate (2 mV/s) and the mass of an electrode. The concentration of electrolyte was 1 M NaCl.

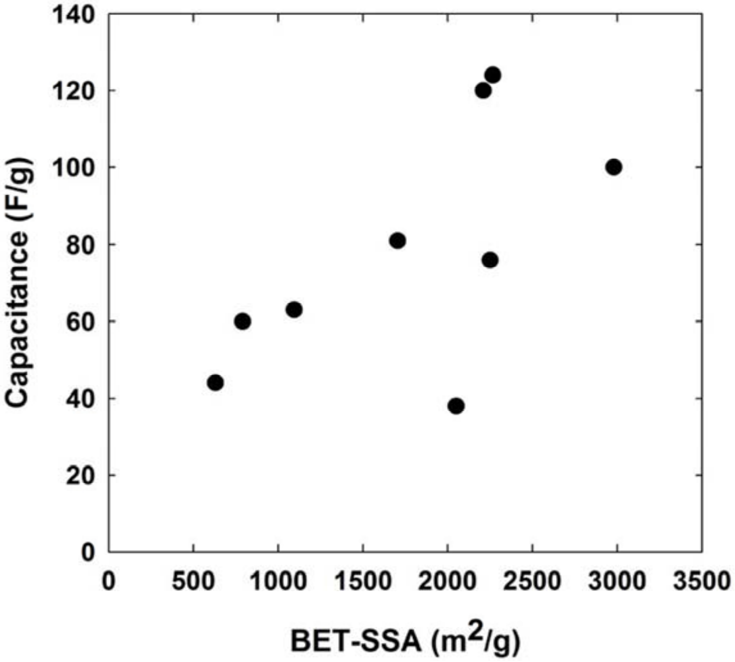

Figure 3-4. Relationship between BET specific surface area (BET-SSA) and capacitance. Capacitance was measured using cyclic voltammetry in 1 M NaCl (scan rate = 2 mV/s). BET-SSA was obtained for powdered carbons before they are fabricated to carbon composite electrodes (carbon:superP:binder = 86:7:7 in weight ratio).

Fig. 3-5 shows the concentration-dependent behavior of carbon composite electrodes obtained by galvanostatic charge/discharge tests, where (a) and (b) display representative voltage profiles (MSP-20) and resulting specific capacitance of all the electrodes, respectively. As shown in Fig. 3-5(a), we observe representative linear charge/discharge voltage profile (MSP-20) through all of the electrolyte concentrations, indicating typical capacitive behavior (profiles of the other electrodes were provided in Figs. 3-6–3-8). It should be noted that the linear profile could be obtained at the low electrolyte concentration (0.01 M NaCl) due to the narrow range of voltage (0.0–0.4 V). The electrolyte of low concentration contains insufficient amount of ionic charges for charging or discharging within a wider range of voltage; the profile will be no longer linear and subsequent analysis would become difficult. Therefore, careful attention is required when conducting an analysis in such a low electrolyte concentration using conventional electrochemical characterization methods [2]. Also, we observe that resistance of the electrolyte increased with decreasing concentration by *iR* drop. The *iR* drop is observable in 0.01 M NaCl at the beginning of the discharging profile (left-side inset, Fig. 3-5(a)), which is barely seen in the case of 1 M NaCl (right-side inset, Fig. 3-5(a)). Fig. 3-5(b) shows the specific capacitance of activated carbon composite electrodes, which were calculated using discharging voltage profiles of Fig. 3-5(a). As can be seen, decreased specific capacitance at the lower electrolyte concentration is observed; the specific capacitance of MSP-20 decreased from

131 F/g at 1 M to 96 F/g at 0.01 M. The other electrodes also followed this tendency, which could be explained by the concentration-dependent feature of the double layer structure. As the electrolyte concentration decreased from 1 to 0.01 M, the thickness of the diffuse layer would increase [122]. Consequently, a loosely packed double layer would result in a low specific capacitance, which is consistent with the result of Fig. 3-5(b). Also, this result is in agreement with previous studies on the double layer capacitor and the membrane-cooperated CDI (MCDI) regarding galvanostatic charge/discharge tests in various concentrations [123, 124].

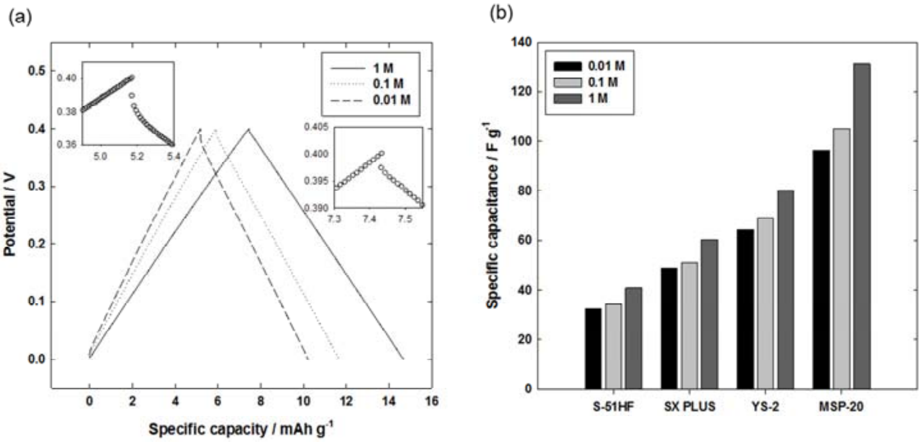

Figure 3-5. Concentration-dependent capacitive behavior of carbon composite electrodes. (a) Representative galvanostatic charge/discharge voltage profile of MSP-20 recorded at a current density of 0.5 mA/cm2; electrolyte concentrations were 1 M (solid line), 0.1 M (dotted line), and 0.01 M (dashed line) NaCl. Magnified insets show the voltage profiles for 0.01 M (left side) and 1 M (right side) when discharging started. (b) The specific capacitance was calculated from discharging profiles.

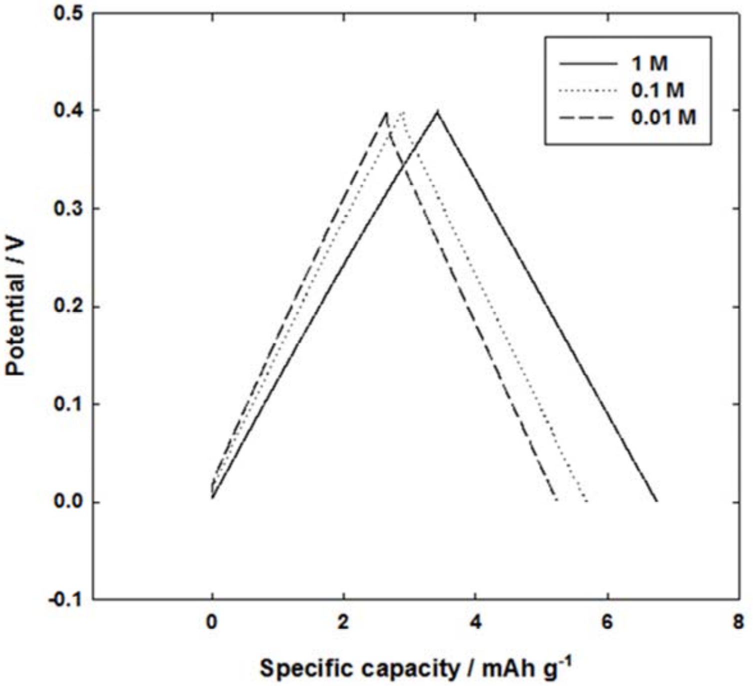

Figure 3-6. Galvanostatic charge/discharge voltage profiles of S-51HF.

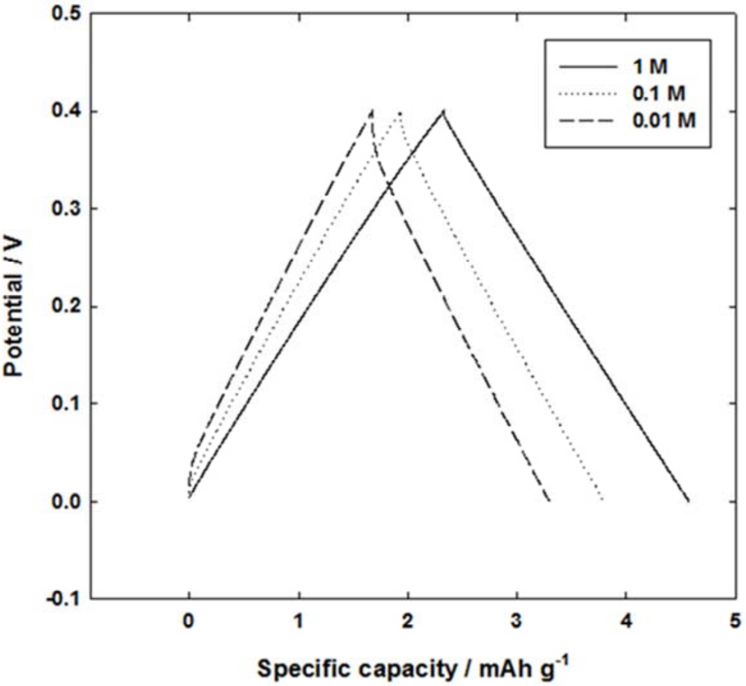

Figure 3-7. Galvanostatic charge/discharge voltage profiles of SX PLUS.

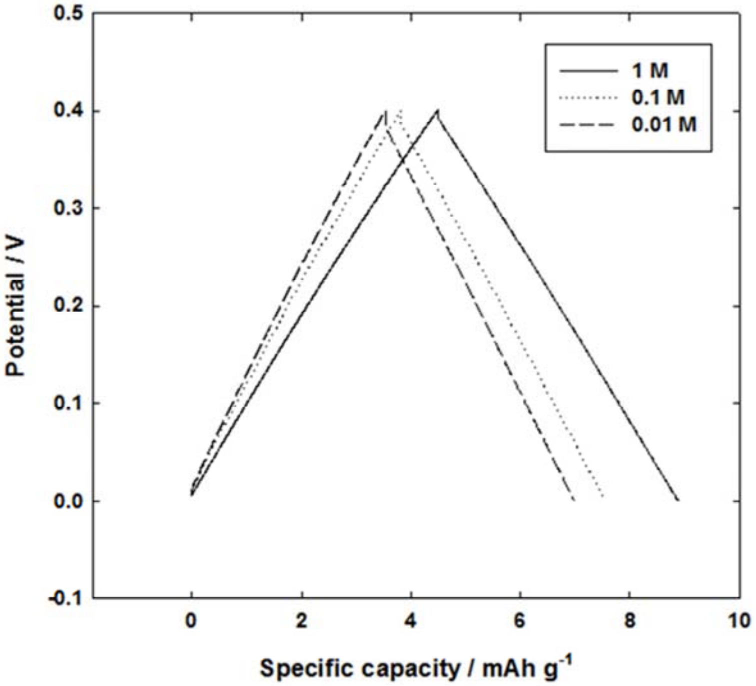

Figure 3-8. Galvanostatic charge/discharge voltage profiles of YS-2.

Deionization performance. Fig. 3-9 shows the deionization performance of activated carbon composite electrodes used in this study. Fig. 3-9(a) displays representative conductivity change data, which exhibits typical deionization/regeneration behavior. In a deionization step, conductivity sharply decreases from the initial value (~1.2 mS/cm) to a different value (~0.9 mS/cm for MSP-20); positive (Na^+) and negative (Cl^-) charges are drawn to oppositely charged electrodes and stored in the pore structure as the deionized solution passes between a pair of electrodes. Afterward, the conductivity returns to the initial value at the end of the deionization step, indicating that the system has reached to a pseudo-equilibrium state for deionization in which the ion transport rate has become zero [111]. The system was switched to a regeneration step after the deionization step; ionic charges were repelled from each electrodes followed by a sharp increase in conductivity. The conductivity returns to the initial value after the sharp increase, suggesting the electrodes regenerated in 10 min. Furthermore, the electrodes exhibited a good reproducibility, which is important requirement for CDI. These results confirm that our CDI system worked properly and the data could be utilized in the subsequent analysis. Fig. 3-9(b) shows the time-dependent deionization capacity (D) of each electrode plotted for quantitative analysis. Recorded conductivity data (the 3rd cycle in Fig. 3-9(a)) was integrated to obtain deionization capacity (the mass of deionized NaCl (mg) divided by the mass of both carbon composite electrodes (g)), in which we assumed that the conductivity of feed solution could represent the concentration of NaCl. After 10 min of deionization, MSP-20 (13.6 mg/g) exhibited the best deionization performance in terms of deionization capacity. The other electrodes are listed here in descending order of deionization capacity: YS-2 (7.0 mg/g), SX PLUS (6.2 mg/g), and S-51HF (4.1 mg/g). The deionization profiles (deionization capacity vs. time) exhibited an abrupt increase followed by a more gradual increase, to finally reach a plateau, which is the total capacity. This behavior indicates that most available charge storage sites are utilized during the early phase of the deionization process and the rate slows approaching saturation.

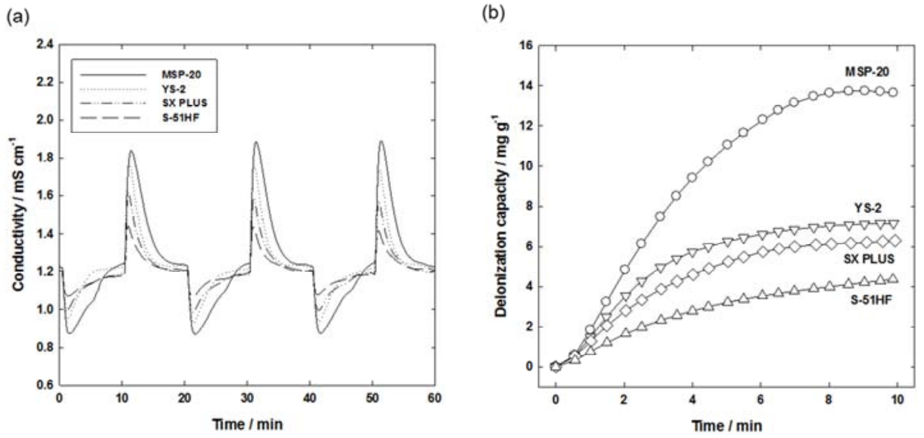

Figure 3-9. Representative deionization performance of carbon composite electrodes. (a) Conductivity of an effluent was continuously recorded was plotted over time. The operation was carried out for 60 min; 1.2 V for 10 min (deionization step) and 0 V for 10 min (regeneration step) were repeated for three times. (b) The conductivity data of the 3rd deionization step (40–50 min) was converted to deionization capacity (mg/g) by integration, representing to the mass of deionized ionic charge (mg) divided by the mass of a pair of electrodes (g).

3.1.4. Discussion

Fig. 3-10 illustrates schematic diagrams describing behavior of ions during deionization in CDI. In the first step (Fig. 3-10(a)), ions (only negative-charged ions are expressed for convenience) are distributed adjacent to the electrode surface (black rectangle). Charging the electrode (Fig. 3-10(b)) generates potential gradient and ions are attracted to the surface by migration. Then, the transport of ions temporarily makes a void, thus concentration gradient develops which subsequently causing transport of ions by diffusion (Fig. 3-10(c)). Finally (Fig. 3-10(d)), concentration of a spacer channel decreases, which corresponds to deionization. This chain reaction could enable the deionization of ions in a spacer channel (~100 μm) which is located far from the double layer (~3 nm in 10 mM NaCl).

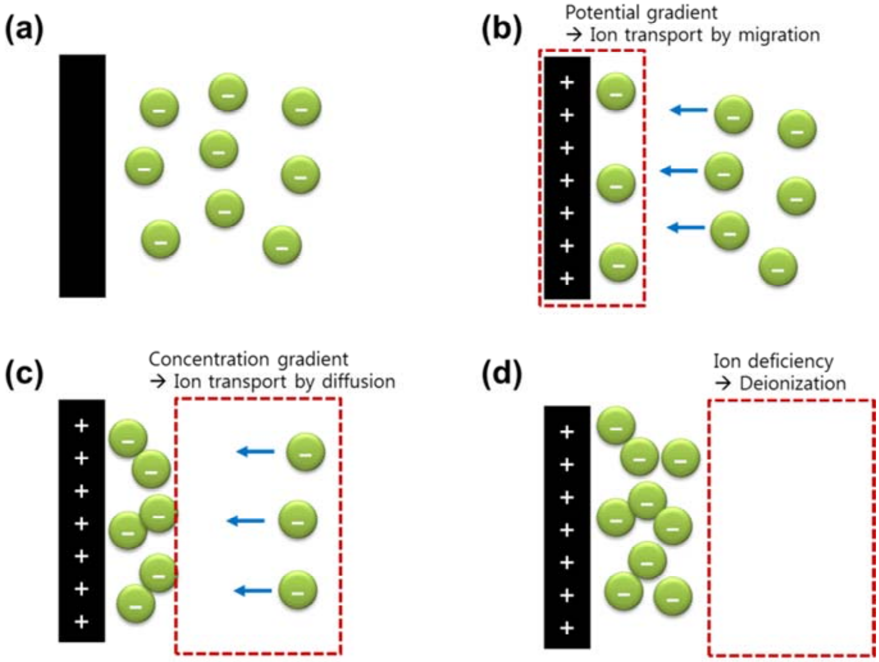

Figure 3-10. Schematic diagrams of ionic behavior during deionization in CDI.

Double-layer formation is essential to the desalination process in CDI, and it can be represented by capacitance. Therefore, capacitance has been considered as the most important parameter to characterize CDI electrodes. Capacitance measurements have been generally made in a high concentration electrolyte in order to minimize contributions of the electrolyte. However, this approach seems to be inappropriate to CDI, since it is more suitable to low electrolyte concentrations considering charge efficiency and energy consumption [25, 125]. In order to minimize this discrepancy and precisely measure the concentration-dependent capacitance, we measured capacitance at various concentrations as can be seen in Fig. 3-5(b). In this figure, we observe that capacitance decreased with decreasing electrolyte concentration with retention ratio ($C_{0.01\text{ M}}/C_{1\text{ M}}$) of 0.7 to 0.8. This result suggests that capacitance measured at a high electrolyte concentration can be used to estimate capacitance values at low electrolyte concentrations. However, it should be noted that the retention ratio of 0.7 to 0.8 would be only applicable to a typical microporous carbon, since the activated carbons used in this study mainly consisted of micropores (Table 3-1). Also, other types of carbon, such as mesoporous carbons, would result in different retention ratio due to the different pore structures [126, 127].

Next, capacitance values measured at a low electrolyte concentration were converted to charge capacity in order to compare with the deionization capacity. Herein, the converted deionization capacity (D_c) represents the total deionization capacity of an electrode, assuming that overall deionization could be achieved when the charge capacity obtained from capacitance (multiplied by voltage) was utilized to remove ionic charges in deionization. The converted deionization capacity was defined as following equation,

$$D_c = 1000CVM_w/4F \tag{3}$$

where D_c is the converted deionization capacity (mg/g) of the CDI system based on capacitance of the electrodes; C (F/g) is the specific capacitance of a single electrode measured using galvanostatic charge/discharge tests at 0.01 M NaCl; V is the applied voltage to the CDI system (1.2 V); M_w is the molecular weight of the ion in the feed solution (NaCl, 58.443 g/mol); and F is Faraday's constant (96500 C/mol). In addition, 1/2 was adopted as the CDI consists of two electrodes and then the capacitance becomes half of the single-electrode capacitance ($1/C = 1/C_1 + 1/C_2$), as we assume that capacitance of the two electrodes are the same. Additionally, the equation was multiplied by 1/2 in order to include the mass of two electrodes.

Fig. 3-11 shows the relationship between converted deionization capacity and deionization capacity. As can be seen, the deionization capacity is greatly proportional to the converted deionization capacity (or the single-electrode capacitance below the x-axis), regardless of types of carbon electrodes. MSP-20 (upward triangle) showed the highest deionization capacity with the highest converted deionization capacity, while S-51HF (circle) showed the lowest deionization capacity with the lowest converted deionization capacity. The slope in the plot refers to the correlation coefficient (D/D_c), indicating a ratio of the deionization capacity over the converted deionization capacity; the coefficient of unity means that all the electric charges are utilized to remove ionic charges from a bulk solution in the CDI. However, this coefficient will always be lower than unity because a double-layer formation includes not only an attraction of counter-ions but also a repulsion of co-ions [128]. We observe that the data points (filled symbols, Fig. 3-11) are located between two lines with the slope of 0.6 and 0.8 (light gray-filled area), indicating that 60–80% of converted deionization capacity was utilized in deionization. When the charge capacity evaluated from 1 M NaCl was used as the converted deionization capacity (open symbols, Fig. 3-11), 50–60% of the charge capacity was found to be utilized in deionization (dark gray-filled area). This correlation clearly demonstrates that the ability of an electrode plays an important role in capacitive deionization. Deionization performance, especially the total deionization capacity, was found to be strongly dependent on the capacitance of the electrode. Interestingly, the correlation coefficient values obtained in this study were in a good agreement with the charge efficiency reported in the previous studies [25, 111, 123]. In those studies, the charge efficiency was calculated based on applied charges in deionization, which is different from the conversion of capacitance value to charging capacity (this study). However, these two approaches correspond with each other, thus capacitance measurement at a low electrolyte concentration could be one of feasible analytical method to evaluate CDI performance. Also, note that various correlation coefficients of the activated carbon composite electrodes in this study could be partly explained by faradaic processes that may occur in deionization. Faradaic reactions may affect pH, chemical components of carbon surface, and double layer structure [129, 130], thus CDI performance may be deteriorated. Correlation coefficients may be diverse with various activated carbons; different chemical structures of carbon would lead to different faradaic reactions. Moreover, pH changes could affect conductivity and subsequent deionization capacity calculation, which was insignificant in this study; the deionization capacity obtained in the charging and discharging were similar (refer to Table 3-2). Additionally, the experimental methods of evaluating capacitance at a low electrolyte concentration and deionization capacity in the CDI system would have limitations to accurately analyze the performance, which would be improved in further studies.

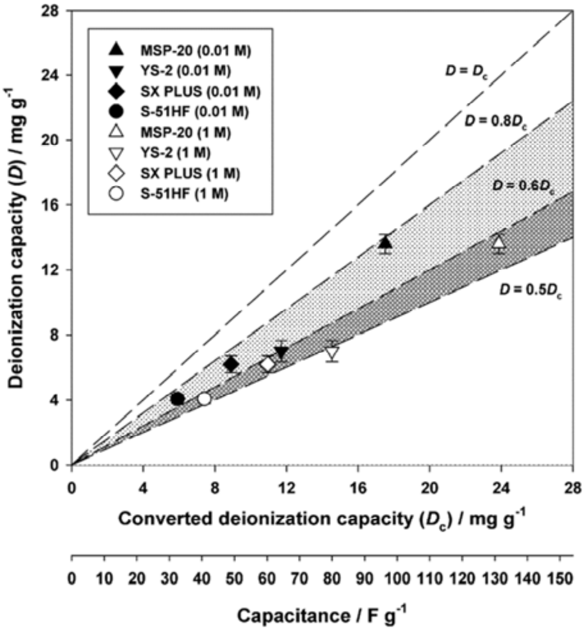

Figure 3-11. Correlation between converted deionization capacity (D_c) and deionization capacity (D). The converted deionization capacity was calculated by Eq. (3) and applying capacitance (additional x-axis below the plot) measured at 0.01 M NaCl (filled symbols) and 1 M NaCl (open symbols), representing the maximum deionization capacity. Deionization capacity was evaluated in the CDI system at 0.01 M NaCl. Note that filled symbols are located between D=0.6D_c and D=0.8D_c (light gray-filled area), indicating that 60–80% of charge capacity is utilized in deionization. Open symbols are located between D=0.5D_c and D=0.6D_c (dark gray-filled area). In this case, 50–60% of charge capacity (evaluated at 1 M NaCl) is utilized in deionization.

Table 3-2. Deionization capacity values calculated using a charging and a discharging step.

	Charging (mg/g)	**Discharging (mg/g)**
S-51HF	4.1	3.8
SX PLUS	6.2	5.9
YS-2	7.0	7.7
MSP-20	13.6	15.2

This study suggests that the deionization capacity of the CDI system can be estimated by characterizing capacitance of the electrode prior to the CDI operation. The retention ratio ($C_{0.01\ \mathrm{M}}/C_{1\ \mathrm{M}}$) and the correlation coefficient (D/D_c) are required to estimate the deionization capacity from the capacitance. For example, deionization capacity of 10 mg/g (0.01 M NaCl, 1.2 V) can be obtained with capacitance of 100 F/g (single-electrode capacitance), when the retention ratio of 0.8 (Fig. 3-5(b)) and the correlation coefficient of 0.7 (Fig. 3-11) are applied into Eq. (3). However, it should be noted that these parameters were obtained under the specified experimental conditions (carbon electrodes made from several selective commercial activated carbons), so that caution is required for more general applications.

3.1.5. Conclusions

This study showed that the converted deionization capacity had a good linear relationship to the deionization capacity, where the converted deionization capacity was evaluated by measuring capacitance at a low electrolyte concentration. In particular, we found out that these two parameters (D and D_c) are related with the correlation coefficient of 0.6–0.8 (0.01 M NaCl) and 0.5–0.6 (1 M NaCl); 60–80% and 50–60% of the charge capacity evaluated from capacitance were utilized in deionization. This approach can provide simple and convenient method to estimate deionization performance from capacitance, which would serve as one of electrode design standards in the future CDI researches.

3.2. Enhanced Charge Efficiency and Reduced Energy Use in Capacitive Deionization by Increasing the Discharge Voltage

3.2.1. Introduction

Capacitive deionization is an electrochemical method for water desalination based on applying a voltage difference (called the cell voltage, V_{cell}, or charging voltage, V_{ch}) between two porous carbon electrode films in contact with aqueous electrolyte [2]. In this process, ions migrate to the electrode of opposite charge (cations to the cathode, anions to the anode) following charge transfer through the external circuit that connects the two electrodes. Within the electrode, ions are stored in the electrical double layers (EDL) which form in the micropores inside the porous carbon particles that compose the electrode [131]. As a consequence, the water flowing through the cell becomes partially desalinated. Generally, the two electrode films are placed parallel to the direction of water flow which runs in between the electrodes through a spacer layer, see Fig. 3-6a. Alternative designs use carbon electrode wires [53], flowable electrode slurries [22, 54, 132-134] or flow-through electrodes [82]. In addition, electrodes can be chemically modified [68, 135], nanoparticles can be incorporated [16, 78, 136], ion-selective coatings can be applied [41, 137], or ion-exchange membranes can be placed in front of the electrodes in a modification called Membrane

Capacitive Deionization, or MCDI [17, 27, 38, 39, 95, 138-141].

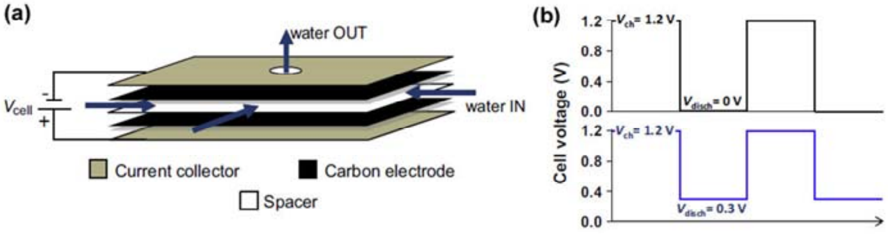

Figure 3-12. (a) Schematic diagram of a CDI cell as used in this study. (b) Operational cycles where discharge voltage is varied (V_{disch} = 0 V and 0.3 V) as a function of time.

In most of these designs, CDI comprises a repeated cycle of charging (salt adsorption) and discharging (salt release), where salt ions are adsorbed upon applying a cell voltage during charging. After subsequent discharge of the cell, generally done by short-circuiting the two electrodes (i.e., a discharge voltage of V_{disch}=0 V is applied), ions are released from the electrodes and a concentrated saline stream is temporarily produced. These two steps of salt adsorption (charging) and desorption (discharge) constitute one full CDI cycle. The charge efficiency Λ describes the ratio of salt adsorption (desorption) over the charge transfer [25]. The charge efficiency Λ differs between materials and depends on the applied cell voltage and salt concentration [142]. For a typical cell voltage of V_{cell}=1.2 V and for salt concentrations in the range 5-50 mM, values for Λ ranging from 0.5 to 0.8 have been experimentally found. Charge efficiency Λ increased with cell voltage, and decreased with salt concentration [142]. Values for Λ close to, or beyond, unity have never been reported for CDI. Indeed, a value of Λ of unity is considered the theoretical maximum, and would be achieved when one full NaCl salt molecule is removed for an equivalent electron transfer between the electrodes. The lower values of Λ obtained in practice, are disadvantageous as it implies more charge transfer and electrical energy input than is necessary for a given objective of salt removal. However, such sub-optimal values of Λ clearly below unity seem to be inherently connected to CDI as a consequence of the structure of the electrical double layer (EDL) in microporous carbons, where the electrical charge is partially compensated by counter-ion adsorption, and partially by co-ion repulsion (ejection of co-ions from the EDL) [142]. The repulsion of the co-ions results in sub-optimal values of the charge efficiency, i.e., a charge efficiency below unity. For salt concentrations below 30 mM, implementation of ion-exchange membranes increases the charge efficiency Λ (Fig. 5d in [39]) to values close to one, because co-ions are blocked from leaving the electrode region, and only counter-ions are transported from spacer to electrode to compensate the electronic charge. The disadvantage of membrane-CDI is the more expensive cell design. Though not well supported by experimental data, theoretical calculations suggest that another route to reach a higher charge efficiency, is to increase the charging voltage to values beyond 1.2 V [142]. However, because of water splitting, voltages beyond 1.23 V lead to an increase in leakage currents, that is, a current which results in electrochemical reactions, which is not used to charge the porous carbon electrodes. Therefore, cell voltages beyond 1.23 V may result in a higher energy consumption. Also the use of (chemically modified) asymmetric electrodes, and reference electrodes, has been suggested as methods to increase [135].

To increase charge efficiency, another route is the use of an increased discharge voltage and, as a consequence, a smaller voltage window for CDI as has been suggested and tested before [143]. This is the route we will reanalyze and extend in the present work by using a fixed value of the cell voltage during charging, V_{ch}=1.2 V, just below the water-splitting voltage, and increase the discharge voltage, V_{disch}, to values above zero, see Fig. 3-6b. As we will demonstrate, both experimentally and theoretically, increasing V_{disch} only moderately, to around V_{disch}=0.3 V, leads to increased values of Λ, while at the same time the salt adsorption capacity and salt adsorption rate are not affected much (order of 5%). Because of the reduced voltage window used in our study, the total charge transfer in one cycle decreases significantly, and thus the overall energy consumption is lower. For instance, in our setup, and for c_{salt}=20 mM and V_{ch}=1.2 V, the energy requirement per ion removed reduces from ~30 kT per ion when V_{disch}=0 V, to ~26 kT per ion when V_{disch}=0.3 V. The results presented in this work go beyond the pioneering work reported in ref. [143] where the charging voltage was V_{ch}=0.6 V and therefore charge efficiency Λ still stayed far below unity, increasing from Λ=0.4 to Λ=0.7 upon increasing the discharge voltage from V_{disch}=0 V to 0.4 V. Another difference is that in ref. [143] it was argued that increasing V_{disch} is disadvantageous because of a significant decrease in salt removal per cycle. However, as we will show, when V_{ch} is the value that we use, V_{ch}=1.2 V, then in the relevant range of values of V_{disch} (up to 0.3 V), this decrease is minor.

In addition, we demonstrate that theoretical equilibrium calculations using a recently proposed “improved modified” Donnan (i-mD) model [142] closely fit the data for charge transfer and salt adsorption, across a range of values of cell voltage and salt concentration, while a porous electrode transport theory for CDI well illustrates dynamic data, i.e., ion transport rates in CDI. We also present experimental and theoretical results for constant-current charging in CDI [144], demonstrating that with an increased discharge voltage the transition period required to reach a stable effluent salinity can be drastically reduced. In summary, our results demonstrate the possibility to increase the charge efficiency in a CDI cycle to values close to unity, leading to a lowered energy consumption, and unchanged salt adsorption, by raising the discharge voltage in CDI to values higher than zero.

3.2.2. Theory

Equilibrium EDL model. To rationalize the origin of improved charge efficiency in a CDI cycle, we make use of an electrical double layer (EDL) model for ion adsorption in microporous carbons [145]. Here we will use the improved modified Donnan (i-mD) model [142] which is an EDL-model that assumes full overlap of the diffuse layers in the small micropores [142]. The i-mD model does not consider ion size effects, but does include a Stern layer capacity and a non-classical "μ_{att}"-term that describes how uncharged carbon micropores also adsorb salt. The EDL model describes the ion concentrations inside the intra-particle pore space, or micropores, ("mi"), where we model the formation of the EDL and the adsorption of salt, as function of the concentration outside the carbon particles (inter-particle pore space, or macropores, "mA") [146], which we model as transport pathways for ions to move from the external solution outside the electrode to the micropores. Note that in this work, the terminology micro-, meso- and macropores, is based on their use in porous electrode transport theory [147] which is a nomenclature different from the strict distinction in size classes as in the IUPAC-definition. At equilibrium, there is no transport across the electrode, and this macropore concentration is equal to that of the external solution outside the electrode, which we will describe using the subscript "∞".

For a 1:1 salt such as NaCl, in the i-mD model the micropore ion concentration relates to that outside the pores according to a modified Boltzmann equilibrium,

$$c_{\mathrm{mi,i}} = c_{\infty} \cdot \exp\left(-z_{\mathrm{i}} \cdot \Delta\phi_{\mathrm{d}} + \mu_{\mathrm{att}}\right) \tag{1}$$

where c_∞ is the outside salt concentration, z_i is the valence of the ion, and $\Delta\phi_d$ the Donnan potential, i.e., the potential increase when going from outside to inside the carbon particle. This is a dimensionless number and can be multiplied by the thermal voltage $V_T=RT/F$ (~25.7 mV) to obtain the Donnan voltage with dimension V. The non-Boltzmann energy term μ_{att} is dimensionless and can be multiplied by RT to obtain a molar energy with dimension J/mol. We will assume equal values of μ_{att} for anion and cation. Inside the carbon micropores, the micropore ionic charge density (per unit micropore volume, dimension mol/m^3=mM) is given by

$$\sigma_{\text{mi}} = \sum_{\text{i}} z_{\text{i}} \cdot c_{\text{mi,i}} \tag{2}$$

This ionic charge σ_{mi} is compensated by the electronic charge in the carbon matrix: $\sigma_{\text{mi}}+\sigma_{\text{elec}}=0$. When using this simple equation we exclude chemical surface charge effects, but such effects can be included [26, 148]. Next, the ionic charge density relates to the Stern layer potential difference, $\Delta\phi_{\text{St}}$, according to

$$\sigma_{\text{mi}} = -C_{\text{St,vol}} \cdot \Delta\phi_{\text{St}} \cdot V_{\text{T}} / F \tag{3}$$

where $C_{\text{St,vol}}$ is a volumetric Stern layer capacity in F/m^3. For $C_{\text{St,vol}}$ we use the expression

$$C_{\text{St,vol}} = C_{\text{St,vol,0}} + \alpha \cdot \sigma_{\text{mi}}^2 \tag{4}$$

where the second term is included to account for the experimental observation that the Stern layer capacity slightly goes up with micropore charge [142]. From this point onward we assume symmetry and only describe an experiment with two equal electrodes (equal mass and composition) [26]. We describe in this section salt adsorption and charge in a CDI-cycle operating at two discrete values of the cell voltage V_{cell}, namely V_{ch} and V_{disch} (for “charge” and “discharge”), where at both levels equilibrium is established.

Combination of Eqs. (1) and (2) leads to

$$\sigma_{\mathrm{mi}} = c_{\mathrm{cation,mi}} - c_{\mathrm{anion,mi}} = -2 \cdot c_{\infty} \cdot \exp\left(\mu_{\mathrm{att}}\right) \cdot \sinh\left(\Delta\phi_{\mathrm{d}}\right) \tag{5}$$

and

$$c_{\mathrm{ions,mi}} = c_{\mathrm{cation,mi}} + c_{\mathrm{anion,mi}} = 2 \cdot c_{\infty} \cdot \exp\left(\mu_{\mathrm{att}}\right) \cdot \cosh\left(\Delta\phi_{\mathrm{d}}\right) \tag{6}$$

The above equations must be supplemented with

$$V_{\mathrm{cell}} / V_{\mathrm{T}} = 2 \cdot \left|\Delta\phi_{\mathrm{d}} + \Delta\phi_{\mathrm{St}}\right| \tag{7}$$

where V_{cell} is either V_{ch} or V_{disch}. In the i-mD model, in contrast to the previous mD-model [2, 10, 53], the energy term μ_{att} is not taken as a constant, but is given by the ratio of an energy density E divided by the total micropore ions concentration, $c_{\mathrm{ions,mi}}$,

$$\mu_{\mathrm{att}} = E / c_{\mathrm{ions,mi}} \tag{8}$$

This modification, used in the i-mD model, has a significant effect in improving the precision of the mD-model, especially to describe the influence of salinity (see Fig. 4 in ref. [142]) without introducing an extra “fit” parameter. As ref. [142] demonstrated, the use of Eq. (8) gives an excellent description of equilibrium data in CDI, both for salt adsorption and charge, as function of both external salt concentration and of cell voltage.

To calculate the charge Σ_F that is transferred from one electrode to the other during charging (denoted by superscript “ch”), and back during discharging (“disch”), we multiply the micropore charge density σ_{mi} in one electrode, by the volume of micropores per gram of electrode, υ_{mi}, and by Faraday’s number F, do this for charging and discharging, and take the magnitude of the difference

$$\Sigma_F = \tfrac{1}{2} \cdot F \cdot \upsilon_{mi} \cdot \left| \sigma_{mi}^{ch} - \sigma_{mi}^{disch} \right| \tag{9}$$

where Σ_F has dimension C/g.

For the salt adsorption of a cell pair we have

$$\Gamma_{m,salt} = \tfrac{1}{2} \cdot M_{w,NaCl} \cdot \upsilon_{mi} \cdot \left(c_{ions,mi}^{ch} - c_{\infty}^{ch} - c_{ions,mi}^{disch} + c_{\infty}^{disch} \right) \tag{10}$$

which has dimension g/g ($M_{w,NaCl}$=58.44 g/mol). In Eqs. (9) and (10) the factor 1/2 stems from the convention in CDI to define salt adsorption and charge by the mass of anode and cathode together. Eq. (10) is a generalization of Eq. (13) in ref. [2]. It is valid when the external salt concentration c_∞ is the same at the end of the charging and the discharging steps as in the Single-Pass method where the inflow salt concentration is always the same. Eq. (10) is also valid when these two values of c_∞ are different, as in the Batch-Mode method where the water from a small container is continuously re-injected into the CDI cell.

The charge efficiency Λ is the ratio of salt adsorption over charge transfer in a

CDI-cycle, and is given by

$$\Lambda = \frac{F}{M_{\mathrm{w,NaCl}}} \cdot \frac{\Gamma_{\mathrm{m,salt}}}{\Sigma_{\mathrm{F}}}$$

(11)

In case $c_\infty^{\mathrm{ch}}=c_\infty^{\mathrm{disch}}$ (Single-Pass method) and we discharge at zero cell voltage, which in our model implies $\sigma_{\mathrm{mi}}^{\mathrm{disch}}=0$ and thus $\Delta\phi_{\mathrm{d}}^{\mathrm{disch}}=0$, Eq. (11), with the substitution of Eqs. (9) and (10), simplifies to

$$\Lambda = \frac{c_{\mathrm{ions,mi}}^{\mathrm{ch}} - c_{\mathrm{ions,mi}}^{\mathrm{disch}}}{\left|\sigma_{\mathrm{mi}}^{\mathrm{ch}}\right|} = \frac{\cosh\left(\Delta\phi_{\mathrm{d}}^{\mathrm{ch}}\right) - \exp\left(\mu_{\mathrm{att}}^{\mathrm{disch}} - \mu_{\mathrm{att}}^{\mathrm{ch}}\right)}{\sinh\left(\left|\Delta\phi_{\mathrm{d}}^{\mathrm{ch}}\right|\right)} \tag{12}$$

which clearly shows the general feature that the theoretically predicted value for the charge efficiency directly depends on the diffuse layer (Donnan) voltage during charging, $\Delta\phi_{\mathrm{d}}^{\mathrm{ch}}$, and not on parameters related to the Stern layer. Note that in the i-mD model, where μ_{att} depends on $c_{\mathrm{ions,mi}}$ (which in turn depends on $\Delta\phi_{\mathrm{d}}^{\mathrm{ch}}$), charge efficiency is no longer given by $\Lambda=\tanh(|\Delta\phi_{\mathrm{d}}^{\mathrm{ch}}|/2)$ as it is in the mD-model which uses a fixed value of μ_{att}.

CDI porous electrode transport theory. To describe the dynamics of salt electrosorption and charge in porous carbon film electrodes forming a CDI cell, we jointly consider ion transport through the space between the carbon particles, that is, through the large transport pathways across the electrode (interparticle pore volume), which we call the macropores (subscript: mA), and the electrosorption of ions inside carbon particles (intraparticle pore volume) which we call the micropores (subscript: mi) [148, 149]. This classical model considers a perfect bimodal pore size distribution, of one type of macropore and one type of micropore, and neglects mesopores [147, 150]. In the present work these mesopores are introduced in Eq. (14). Note again that the nomenclature for these pore classes is based on that in transport theory, not the IUPAC definition based on size only. This mesoporosity describes a charge-neutral volume inside carbon particles, of the same salt concentration as the nearby macropores, but without sustaining ion transport. Ion adsorption in the micropores is described by the i-mD model discussed in the above section. The CDI porous electrode transport theory describes ion electromigration through the spacer and electrode macropores, and the subsequent storage of ions and electrical charge in the EDLs in the micropores [10]. The geometry considered is based on two porous electrodes placed parallel, with a flat planar slit, called the transport channel or spacer, placed in between. In the direction of flow, this transport channel is mathematically divided into M sequential sub-cells, see Fig. 2 in ref. [17] and Fig. 2 in ref. [148]. In the following section, we first describe a single sub-cell and the ion transport into the electrode. Next we describe how all sub-cells can be combined in a unified model for the full CDI system. We focus on a monovalent salt solution, assuming that the two ion diffusion coefficients are equal (as for KCl). Extensions to mixtures with ions of different diffusion coefficients (as must formally also be considered for NaCl) are described in refs. [50, 148].

In the CDI porous electrode transport model, two coupled one-dimensional partial differential equations must be solved along with additional algebraic equations to evaluate the transport and adsorption of salt across the porous carbon electrodes. The model describes, as a function of the depth in the electrode *x*, and time *t*, four coupled variables: (1) the salt concentration in the macropores, c_{mA}; (2) the electrostatic potential there, ϕ_{mA}; (3) the charge density in the micropores, σ_{mi}; and (4) the ions concentration in the micropores, $c_{\mathrm{ions,mi}}$.

The spacer channel between the two electrodes is described as a series of continuously stirred sub-cells with a salt concentration c_{sp} that is only a function of time, described by the salt mass balance

$$p_{\mathrm{sp}} V_{\text{sub-cell}} \frac{\partial c_{\mathrm{sp}}}{\partial t} = -J_{\mathrm{ions}} A + \phi_{\mathrm{v}} \left(c_{\mathrm{sp,in}} - c_{\mathrm{sp}} \right) \tag{13}$$

where $V_{\text{sub-cell}}$ (in m^3) is the geometrical volume of the sub-cell, p_{sp} is the open porosity of the spacer channel, *A* the exchange area of one sub-cell with one electrode (in m^2), and ϕ_{v} the water volumetric flow rate running through the cell, i.e., along the electrodes (in m^3/s). We assume the two electrodes to behave symmetrically and as a consequence the ion flux into one electrode, J_{ions}, is equal to the salt flux into both electrodes.

Base on the Nernst-Planck equation [151], transport within the porous electrode is described by two coupled partial differential equations. First, a differential salt mass balance can be set up, given by

$$\frac{\partial}{\partial t}\left(\left(p_{\mathrm{mA}}+p_{\mathrm{meso}}\right)c_{\mathrm{mA}}+\tfrac{1}{2}p_{\mathrm{mi}}c_{\mathrm{ions,mi}}\right)=p_{\mathrm{mA}}D\frac{\partial^2 c_{\mathrm{mA}}}{\partial x^2} \tag{14}$$

with the electrode position x between $0<x<L_{\mathrm{elec}}$, where L_{elec} is the electrode thickness, and where D is the average ion diffusion coefficient in the macropores, and where p_{mA}, p_{meso}, and p_{mi} are the macro-, meso-, and microporosity in the electrode. As Eq. (14) shows, we consider all fluxes to be in only one direction, namely the direction into the electrode, i.e., at cross-angles with the general flow direction of the solution through the channel.

The second partial differential equation describes the charge in the micropores and is given by

$$p_{\mathrm{mi}}\frac{\partial \sigma_{\mathrm{mi}}}{\partial t}=2p_{\mathrm{mA}}D\frac{\partial}{\partial x}\left(c_{\mathrm{mA}}\frac{\partial \phi_{\mathrm{mA}}}{\partial x}\right) \tag{15}$$

At each position in the electrodes, the macropore potential ϕ_{mA} is related to the potential ϕ_1 in the carbon matrix according to

$$\phi_1-\phi_{\mathrm{mA}}=\Delta\phi_{\mathrm{d}}+\Delta\phi_{\mathrm{St}} \tag{16}$$

with expressions for $\Delta\phi_d$ and $\Delta\phi_{St}$ given by Eqs. (3)-(6). At each position the micropore ions concentration $c_{\text{ions,mi}}$ is related to charge σ_{mi} according to

$$c_{\text{ions,mi}}^2 = \sigma_{\text{mi}}^2 + \left(2 \cdot c_{\text{mA}} \cdot \exp\left(\mu_{\text{att}}\right)\right)^2 \tag{17}$$

With the potential in the carbon matrix set to zero (ϕ_1=0), the cell voltage is given by

$$V_{\text{cell}} = 2 \cdot V_{\text{T}} \cdot \left(\phi_{\text{mA}}\big|_{x=0} + \Delta\phi_{\text{sp}}\right) \tag{18}$$

where "*x*=0" refers to the front side of the electrode (in contact with the spacer channel), and where $\Delta\phi_{\text{sp}}$ is the voltage drop across half the spacer channel, obtained from

$$J = -4 c_{\text{sp}} p_{\text{sp}} D \cdot L_{\text{sp}}^{-1} \cdot \Delta\phi_{\text{sp}} \tag{19}$$

where J is the current density (in mol/m^2/s). The ions flux, J_{ions}, out of the spacer channel required in Eq. (13) is equal to the ions flux directed into the electrode

$$J_{\text{ions}} = -2 p_{\text{mA}} D \left.\frac{\partial c_{\text{mA}}}{\partial x}\right|_{x=0} \tag{20}$$

and a similar relation holds for the current density,

$$J = -2 p_{\text{mA}} D \left.\left(c_{\text{mA}} \frac{\partial \phi}{\partial x} \right)\right|_{x=0} \tag{21}$$

For an overview of the required initial and boundary conditions in c_{mA}, ϕ_{mA}, σ_{mi} and $c_{\mathrm{ions,mi}}$ in each sub-cell. In the full model for the CDI-cell, *M* of the sub-cells as described above, are placed sequentially in the direction of flow. In this direction salt is transported through the spacer channel downstream, as described by Eq. (13) with c_{sp} the concentration in sub-cell i and $c_{\mathrm{sp,in}}$ the concentration in the up-stream sub-cell i-1. The concentration in the last sub-cell (i=*M*) is equal to the effluent concentration. The sub-cell volume is equal to the total spacer channel volume (height times electrode area) divided by the number of sub-cells, *M*. In the present work we do not include a "dead volume" after the stack as in refs. [10, 26]. The current density per cell, *I* (in A/m^2) is calculated from $I=F/M\cdot\Sigma_i J_i$, where Σ_i is a summation over all sub-cells. This current density, *I*, can be integrated over time and multiplied by the cell cross-sectional area to obtain the total stored charge. The charge stored in an electrode can also be calculated by averaging the local charge density σ_{mi} (Eq. 15) and multiplying by Faraday's number, the microporosity p_{mi}, and the volume of the electrode. Dividing by electrode mass (anode and cathode together) gives us the charge Σ_F (C/g) as plotted in Figs. 3-7, 3-8 and 3-9.

3.2.3. Experimental

Electrode preparation. Carbon composite electrode was fabricated using YP-

50F (Kuraray, Japan), carbon black (Vulcan XC72R, Cabot Corp., Boston, MA), and a binder (85:5:10 in weight ratio). In order to prepare the binder solution (3 wt%), polyvinylidene fluoride (PVDF, Kynar HSV 900, Arkema Inc., Philadelphia, PA) was dissolved in N-methyl-2-pyrrolidone (NMP) and vigorously stirred for 24 h to secure homogeneity. After YP-50F and carbon black were mixed with the prepared binder solution, it was intensively blended in a ball-milling machine for 40 min (500 rpm) and the resulting carbon slurry was used for casting. The electrode casting was carried out on a glass plate with a doctor blade (thickness 500 μm). Afterwards, the electrode was directly transferred into deionized water together with the glass plate to solidify the binder. The resulting carbon electrode (~260 μm) was cut into square pieces (6×6 cm^2) with a small square (1.5×1.5 cm^2) located at the center.

CDI experiments. Fig. 3-6a shows a schematic diagram of the CDI system used in this study. Each cell consists of a pair of graphite current collectors, a pair of carbon electrodes, and a spacer (AP20, Glass Fiber Filter, Millipore, MA, uncompressed thickness ~380 μm). A stack was constructed of N_s=4 of such cells and installed in a rectangular Teflon housing which was sealed off. As depicted in Fig. 1a, water is pumped from outside to inside through the spacer using a peristaltic pump (flow rate 30 mL/min for the stack of 4 cells), and the outlet conductivity and pH were continuously monitored. The experiments were conducted in NaCl solutions of different concentration (c_∞=5, 20, 80 mM) prepared in a vessel (10 L) with N_2 purging. While the solution flows through the CDI stack, the system was controlled by a power supply (IviumStat, Ivium Technologies, the Netherlands). The following voltage differences across each cell were imposed: a voltage V_{ch} during charging (deionization, salt adsorption) and V_{disch} during discharge (regeneration, desorption). For the equilibrium experiments (Figs. 3-8 and 3-9) the duration of each step (half-cycle time, or HCT) was 20 min while HCT was lower (but again the same for charging and discharging) in the experiments of Fig. 3-10. Each experiment was carried out at a distinct value of V_{disch}, ranging from 0 to 0.9 V, while the charging voltage V_{ch} was always set to 1.2 V as described in Fig. 3-6b (except for experiments reported in Fig. 3-7 and Fig. 3-11). From the measured electrical current, the charge transferred (back and forth) in one cycle is calculated, while from the measured conductivity (corrected via the measured pH for the partial conductivity of protons and hydroxyl ions) and from the water flow rate, the salt adsorption is calculated. Note that salt adsorption in mg/g of NaCl is based on the mass of all electrodes in the system (both anode and cathode). The charge was obtained from the charging step (from integrating the current vs. time-plot), after subtracting a small leakage current, which is the current which still flows when equilibrium is reached after 20 min. Note that when the leakage current would not be accounted for, the calculated charge is a few percent higher, and thus values of the charge efficiency are a few percent less than reported. The charge transfer during discharge is generally a few percent lower than charge transfer in the charging step, i.e., the Coulombic efficiency is below 100%. Charge efficiency, Λ, is the salt adsorption divided by charge, see Eq. (11). None of the reported results are from the first or second cycle after a new experiment, as then dynamic equilibrium is not yet established and the charging salt adsorption and charge are not yet the same as the values during discharge. This condition of salt balance and charge balance is well achieved in subsequent cycles.

To calculate the salt adsorption per cycle, as required in Figs. 3-10a and 3-10b, we use the “new data analysis approach” discussed in ref. [138], where the salt adsorption is based on the entire time period that the effluent salt concentration is below the inflow concentration (period from A to B in Fig. 3 in ref. [138]), a period which is slightly delayed relative to the period of cell charging. Instead, in prior work discussing short cycle times, salt adsorption (desorption) was calculated based on the period of cell charging (discharging).

Data analysis to derive EDL-properties. To fit the i-mD model (EDL theory) to the data, four parameters must be adjusted as summarized in Table 3-2: υ_{mi}, E, $C_{\mathrm{St,vol,0}}$ and α. The analysis is based on the following procedures. First of all, we note that predictions of the theory for Λ, or $\Gamma_{\mathrm{m,salt}}$, as function of Σ_{F} (and vice-versa) depend on the micropore volume υ_{mi} and on the energy E, but are independent of the Stern layer parameters $C_{\mathrm{St,vol,0}}$ and α. Thus, we first plot data for $\Gamma_{\mathrm{m,salt}}$ versus Σ_{F} and compare with the i-mD model to find appropriate values for E and υ_{mi}. A second comparison considers the interesting fact that the Donnan potential, $\Delta\phi_{\mathrm{d}}$ which uniquely determines Λ, also uniquely relates both $c_{\mathrm{ions,mi}}$ and σ_{mi} to one another, see Eqs. (5) and (6) (with the energy E as parameter) and therefore describes the cell voltage V_{cell} (including in the fit $C_{\mathrm{St,vol,0}}$ and α), all independent of the value of υ_{mi}. This is also the case for non-zero values of V_{disch}. So fitting theory for $\Lambda(V_{\mathrm{ch}},V_{\mathrm{disch}})$ to data does not require information of υ_{mi}, see Fig. 3-8d and 3-9d. Together with the direct comparisons of $\Gamma_{\mathrm{m,salt}}$ and Σ_{F} vs V_{cell}, we therefore have various parallel methods for reliable data fitting, and as Figs. 3-8 and 3-9 demonstrate, across a large dataset (varying c_{∞}, V_{ch} and V_{disch}), we can very satisfactorily fit all data of $\Gamma_{\mathrm{m,salt}}$ and Σ_{F} using the i-mD model.

An important point to note is that the micropore volume of υ_{mi}=0.400 mL/g (per gram electrode) that we use in the theory is less than the total pore volume measured by gas sorption analysis which for Kuraray YP-50 is about 0.67 mL per gram of activated carbon (0.57 mL/g electrode), see refs. [10, 56]. Thus, to get an optimum fit of the i-mD model to the data, υ_{mi} is best used as a fitting parameter, not necessarily the same as the total pore volume inside the carbon particles. This is different from our approach in ref. [10] where the pore volume measured by gas adsorption up to pore sizes of 30 nm was included as micropore volume in EDL-modeling and porous electrode (transport) theory. Instead, in the approach as we present here, with υ_{mi} a further fitting parameter, we must consider that the fitted value of υ_{mi} is different from the pore volume from gas adsorption analysis, and we suggest to call this difference (0.57-0.40 mL/g in the present case) mesoporosity. In the mesopores, like in the nearby macropores, we assume equal concentrations of cations and anions (for a 1:1 salt), at the same concentration as in the nearby macropores. The only difference with the macropores is that the ions in the mesopores do not contribute to ion transport across the electrode. The macropore volume, p_{mA}, represents the space located in between the carbon particles and follows from geometrical sizes of the electrodes, the total pore volume from gas sorption analysis, and the skeleton density of the mixture of carbon, carbon black, and binder (for which we use ρ_{sk}=1.93 g/mL). This value is in our case p_{mA}=0.566. Note that the three porosities p_{mA}, p_{meso}, and p_{mi} taken together sum up to a number less than unity (0.794 in the present case), because of the volume taken up by the carbon skeleton itself, by binder and by other solid additives.

Table 3-3. System and electrode dimensions, operational parameters, and settings for theoretical calculations.

	Experimental parameters		
N_s	Number of cells in the CDI stack	4	
ρ_{el}	Electrode mass density	0.41	g mL^{-1}
A_{cell}	Electrode geometric surface area	33.75	cm^2
L_{sp}	Spacer channel thickness (when compressed)	250	μm
p_{sp}	Spacer channel porosity (when compressed)	0.50	
ϕ_v	Flowrate through the CDI stack	30	mL min^{-1}
T	Temperature	298	K
c_∞	Inlet NaCl salt concentration	5, 20, 80	mM
	Values for use in EDL and transport theory		
υ_{mi}	Micropore volume	0.40	mL g^{-1}
p_{mi}, p_{meso}, p_{mA}	Micro-, meso- and macroporosity	0.160, 0.068, 0.566	
D	Average diffusion coefficient of Na$^+$ and Cl$^-$ (in free solution)	1.68*10^{-9}	m^2 s^{-1}
$C_{St,vol,0}$	Volumetric Stern layer capacitance in the zero-charge limit	0.17	GF m^{-3}
α	Parameter for non-constant contribution to Stern capacitance	20	F m^3 mol^{-2}
E	Micropore ion-correlation energy	220	kT mol m^{-3}
M	Number of mathematical subcells in the model	1	

3.2.4. Results and Discussion

To illustrate the response of a CDI cell to the applied cell voltage signal as depicted in Fig. 3-6b, we show in Fig. 3-7 the typical CDI behavior of the effluent salt concentration profile over time, and the accumulated charge (current integrated over time), Σ_F. As can be observed, the effluent concentration drops as the charging starts and in time recovers to the initial value, where the area under the base line (dashed line representing the inlet salt concentration) indicates the amount of salt adsorption, $\Gamma_{m,salt}$. Incorporating the factor $F/M_{w,NaCl}$, the ratio of $\Gamma_{m,salt}$ over Σ_F is the charge efficiency, Λ, see Eq. (11). Experimental data for Σ_F, $\Gamma_{m,salt}$ and Λ are further analyzed in Figs. 3-8 to 3-11. An important operational parameter is the half-cycle time (HCT) which in all experiments is the same for charging and discharging (except for the constant-current experiments of Fig. 3-11). The value of HCT in the experiments reported in Figs. 3-7 to 3-9 is 20 min, while it is reduced to values as low as 1 min in Fig. 3-10. Because of the long HCT, the data reported in Figs. 3-8 and 3-9 can be described by the equilibrium EDL model explained in the first half of the Theory-section, without considering porous electrode ion transport theory which is used in Figs. 3-10 and 3-11. Note that in a series of experimental CDI-cycles as reported in Fig. 3-7, the apparent accumulated charge slowly shifts upward because of a leakage current (see Experimental section). In Fig. 3-7 this shift is removed in data-processing, and each subsequent charging cycle shifted back to zero charge.

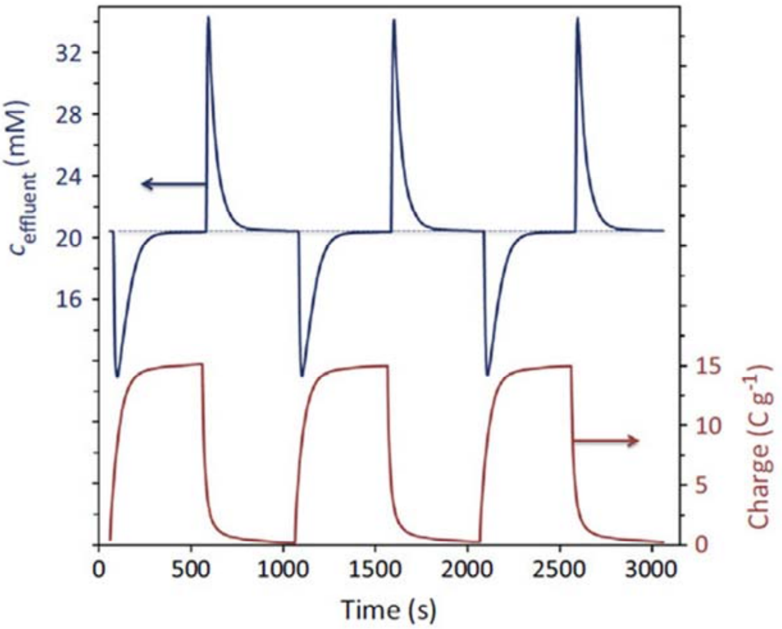

Figure 3-13. Experimental data of CDI cycles for effluent salt concentration and accumulated charge, versus time (V_{ch}=1.2 V, V_{disch}=0.3 V, c_∞=20 mM, half-cycle time 1200 s, only first 500 s shown).

From equilibrium cycles such as reported in Fig. 3-7, data on salt adsorption $\Gamma_{\mathrm{m,salt}}$ and charge Σ_{F} can be extracted which are reported in Figs. 3-8 and 3-9. Fig. 3-8 shows experimental results (points) and theory (lines) of salt adsorption, charge and charge efficiency as function of the salt concentration and the charging voltage, V_{ch}. Fig. 3-8 follows the classical operational method of CDI where always V_{disch}=0 V. Note that here in Fig. 3-8 we present data as function of charging voltage, for a larger range of salinities than before [142], from c_∞=5 to 80 mM. Fig. 3-8a-c shows data and theory for salt adsorption in mg/g (left y-axis) and charge in C/g (right y-axis), in such a way that for Λ=1, the two lines (data sets) should overlap. As clearly they do not overlap, the charge efficiency is less than unity, Λ<1. Fig. 3a shows that at the lowest salt concentration of c_∞=5 mM the two lines (data sets) are closest, and Λ is the closest to unity. Fig. 3-8a-c shows that as function of V_{ch}, both Σ_{F} and $\Gamma_{\mathrm{m,salt}}$ increase, but the latter increases faster (relatively) and thus their ratio, which is Λ, increases with V_{ch}. As function of c_∞ (for a given V_{ch}), Σ_{F} increases while $\Gamma_{\mathrm{m,salt}}$ is constant (in the range of c_∞ studied). Thus Λ increases with V_{ch} and decreases with c_∞, as shown in more detail in Fig. 3d. In the present data range, $\Gamma_{\mathrm{m,salt}}$ does not vary with c_∞, in line with data in ref. [142] which showed that for even lower and higher c_∞, $\Gamma_{\mathrm{m,salt}}$ decreases again. This non-monotonic trend cannot be explained by a simple adsorption isotherm that describes the adsorption of an uncharged solute, which would always predict $\Gamma_{\mathrm{m,salt}}$ to increase with c_∞. Instead, the observed dependence of $\Gamma_{\mathrm{m,salt}}$ on c_∞ (to first increase, and then to decrease again) is the consequence of the salt storage mechanism in CDI, where salt is stored as individual ions in the electrical double layers of two mutually charged porous electrodes.

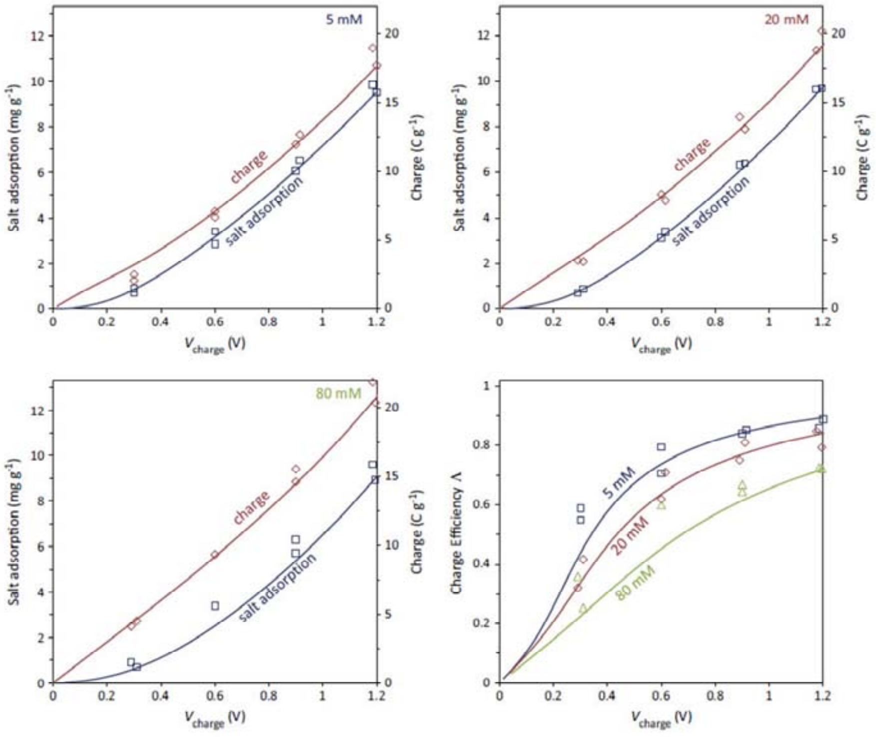

Figure 3-14. Equilibrium salt adsorption, charge, and charge efficiency as function of salt concentration and V_{ch}, which is the cell voltage during charging (V_{disch}=0 V). Solid lines obtained according to the i-mD model (parameters in Table 3-2).

Fig. 3-9 presents results where we fix V_{ch} at 1.2 V and vary V_{disch} for different values of the salt concentration and again plot salt adsorption, charge and charge efficiency. As can be seen, theory again properly describes the data. Experimentally we observe that the charge efficiency increases with increasing V_{disch}, see Fig. 3-9d, which is also in alignment with the theoretical predictions. The charge efficiency increases to values close to unity, especially for V_{disch} beyond 0.3 V. In Figs. 3-9a-c, the salt adsorption and the charge transfer are separately displayed, where the ratio of these two parameters refers to the charge efficiency. As confirmed in Fig. 3-9d, we observe that these two parameters (charge and salt adsorption) get closer as V_{disch} increases. As expected, the charge decreases quite linearly when V_{disch} increases (note that the increase in V_{disch} leads to a decrease in the difference V_{ch}-V_{disch}), indicating the typical capacitive behaviour of carbon electrodes. On the other hand, the behaviour of the salt adsorption as a function of V_{disch} is different from that of the charge. In contrast to the dependence of charge on V_{disch}, the salt adsorption in a cycle remains quite invariant with V_{disch}, as long as V_{disch} does not go beyond 0.3 V. This result confirms that charge efficiency can be increased by increasing V_{disch} to values up and including V_{disch}=0.3 V with only a marginal loss of the salt adsorption per cycle. At c_{∞}=20 mM, upon increasing V_{disch} from 0 to 0.3 V, the charge decreases by 20% while the salt adsorption goes down by only 7%. This implies that the charge efficiency goes up by 14%, and thus the energy consumption per ion removed goes down by that number of 14%, as will be explained below.

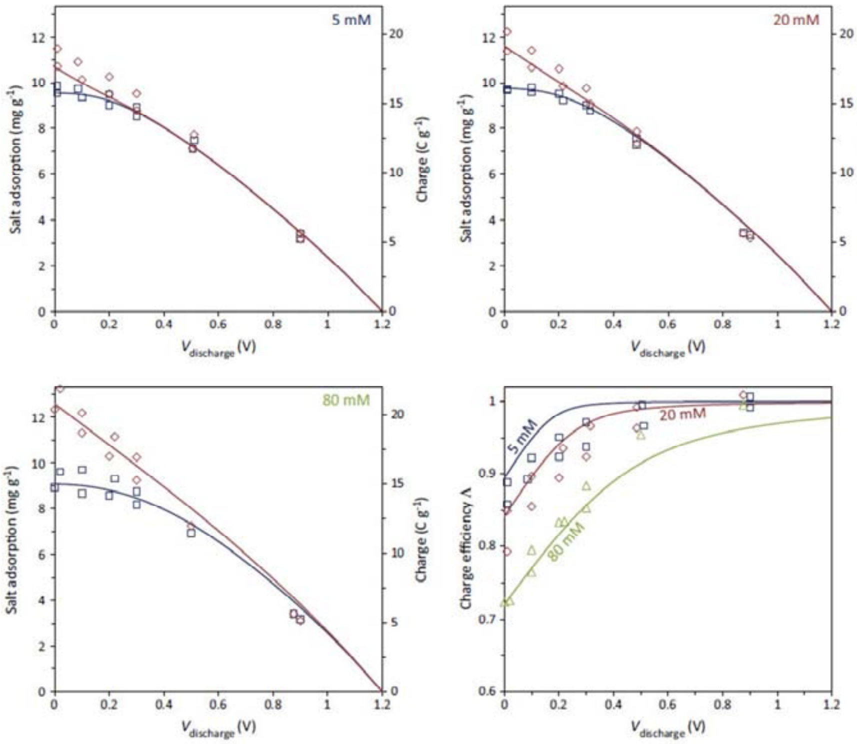

Figure 3-15. Salt adsorption, charge, and charge efficiency (Λ) as function of salt concentration and discharge voltage, V_{disch} (V_{ch}=1.2 V). Solid lines obtained according to the i-mD model (parameters in Table 3-2).

An explanation for the positive effect of increasing V_{disch} is as follows. When the cell is charged at V_{ch}=1.2 V followed by a discharge at V_{disch}=0 V (following the conventional method), the adsorption of counter-ions is accompanied by the expulsion of co-ions, so that the charge efficiency drops to values below unity [143]. This undesirable behaviour of co-ions can be minimized by increasing the *dis*charge voltage. Now, with values of V_{disch} higher than 0 V, a certain amount of co-ions remains expelled during discharging (is not re-adsorbed). In a next cycle, therefore, the expulsion of co-ions is small when the charging starts from a value of V_{disch} higher than 0 V, and thus most of the electrical charge transferred between the two electrodes is utilized solely for the adsorption of counter-ions.

The increased value of charge efficiency directly implies a reduction in the required energy per ion removed. This can be understood as follows. Because the adsorption operates at constant charging voltage, the energy input is directly proportional to the quantity of charge transfer, and thus is inversely proportional to the charge efficiency Λ. For example, for the data at c_∞=20 mM, the energy costs per ion removed is ~30 kT at V_{disch}=0 V, and decreases to ~26 kT for V_{disch}=0.3 V, a reduction by 14%. In this calculation we have not included possible energy recovery during discharge, which is possible when V_{disch}>0 V [152]. Indeed, for this situation of V_{disch}=0.3 V, assuming perfect energy recovery during discharge, the energy per ion removed is reduced to ~20 kT, a reduction of about 30% compared to the original value at V_{disch}=0 V. Note also that for the separation that was achieved, the thermodynamic minimum energy input (decrease in mixing entropy) is only about 0.2 kT per removed ion, a factor 100 below the actual energy input.

Figs. 3-8 and 3-9 discussed equilibrium EDL-properties. The next task is to analyse the kinetics of the CDI process. To this end we first analyze CDI cycles at constant voltage (CV), at increasingly short half-cycle times (HCT), see Fig. 3-10.

In Fig. 3-10a we plot the average salt adsorption rate, "ASAR" which is the salt adsorption per cycle, divided by the total cycle time, which is twice the HCT. Fig. 3-10a clearly demonstrates, both theoretically and experimentally, that ASAR increases with lowering HCT, and in addition that there is hardly an effect of V_{disch}. Admittedly, we had hoped that at an increased V_{disch}, ASAR will be higher, but this is not the case, and ASAR is actually somewhat less. This prior assumption was based on the idea that with $V_{\text{disch}}=0$ V at the start of each charging or discharging step, co-ions and counter-ions go in opposite direction through the electrode and into the micropores. This opposite movement would lead to ion-ion friction and thus a retardation in the motion of both types of ions. Increasing V_{disch} would then lead to a situation where only counter-ions move in and out of the electrode, undisturbed by other ions moving in the opposite direction. However, results in Fig. 3-10a do not support such hypothesis of a frictional force between ions moving in opposite direction, and apparently this suggested retardation effect is not there, or at least is not strong. The transport model doesn't include such an effect either, and describes data very well.

Analyzing both the charge transfer Σ_F and salt adsorption $\Gamma_{m,salt}$ per cycle, Fig. 3-10b shows results of the ratio of the two, the "dynamic" charge efficiency, Λ^*. Here we add the prefix "dynamic" because in contrast to the results of Fig. 3-8 and 3-9, here the charge efficiency is based on a CDI cycle that is not yet at equilibrium. Consequently, the theory lines for Λ^* in Fig. 3-10b are not based on an equilibrium EDL model but are based on the transport model. Both in theory and data, Fig. 3-10b shows that shorter cycles result in a lower Λ^* (vs. the values at longer HCT), indicating an increase in energy costs per ion removed. This is the case because the required energy per amount of salt removed is inversely proportional to Λ^* for a fixed charging voltage. As in Fig. 3-9, we observe that operation at V_{disch}=0.3 V gives a higher charge efficiency, and thus the same energetic advantage of operation at increased values of V_{disch} remains, of about 14% without energy recovery and 30% with energy recovery.

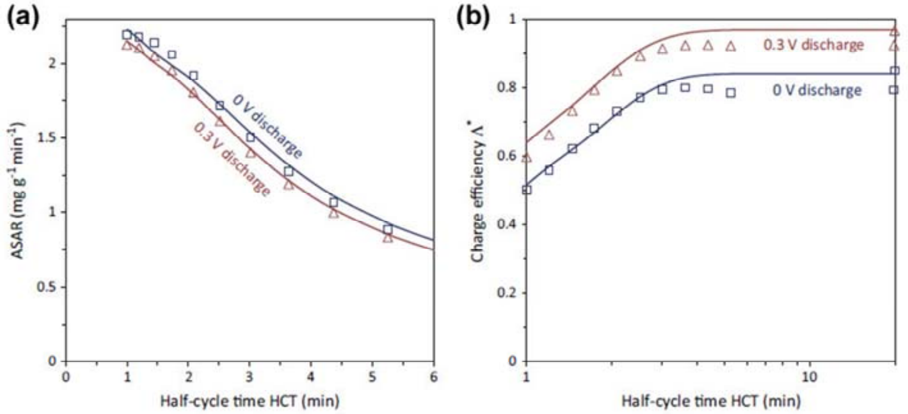

Figure 3-16. CDI at short cycle times. (a). Average salt adsorption rate as function of half-cycle time (HCT; charging and discharging step of equal duration, namely equal to HCT) and as function of V_{disch}. (b). Dynamic charge efficiency as function of HCT (V_{ch}=1.2 V, c_∞=20 mM, electrode thickness 235 μm).

Finally, we show results for constant-current (CC) operation during charging in Fig. 3-11. Constant-current operation is advantageous over constant-voltage (CV) because it leads to a constant effluent salt concentration, $c_{\mathrm{eff,level}}$, that can be easily tuned by adjusting the current. However, up to now it was argued that this operational mode is only feasible with ion-exchange membranes incorporated in CDI (membrane-CDI), because without membranes (i.e., in normal CDI) it takes a longer time before $c_{\mathrm{eff,level}}$ is reached after switching the current direction. In Fig. 3-11 we show our results aiming at reducing the time for $c_{\mathrm{eff,level}}$ to be reached. In these experiments with CC-operation during charging (with a constant current of 0.41 A applied to the stack of N_s=4 cells, thus at a current density of 30.6 A/m^2, until a cell voltage of V_{cell}=1.4 V is reached), the discharge step is always defined by CV operation at certain values of V_{disch}, always for a duration of 250 s. Fig. 3-11a demonstrates that a more rapid drop of salt concentration to $c_{\mathrm{eff,level}}$ is found with increasing V_{disch}, both in the experimental data (points) and in the theoretical calculations (lines). This is due to the fact that at V_{disch}=0 V, at the start of a new charging step, co-ions and counter-ions replace one another, a phenomenon called “ion swapping” in ref. [153] without resulting desalination. Instead, with increasing V_{disch} we reach the situation that right after start of a new cycle only counter-ions are adsorbed (with co-ions remaining outside the micropores at all times).

Fig. 3-11a also shows a theory line for the case that for a short duration of about

20 s after start of the charging step, we use a twice-higher value of the current. The current vs. time-curve is $I(t)=I_{\mathrm{final}}*(2\alpha*(1-\tanh(\alpha*(t-\beta)))+1)$, $\alpha=1/4$, $\beta=22$. This modification (in combination with $V_{\mathrm{disch}}=0.3$ V) results in reaching the value $c_{\mathrm{eff,level}}$ even more rapidly. Note that the theoretical calculations for Fig. 6 are based on $\Phi=27.5$ mL/min (for the stack of 4 cells), instead of $\Phi=30$ mL/min, to make the theory-lines fit the data somewhat better. Thus the present calculations must be considered not as exact, but as illustrative. Fig. 3-11b shows that considering only the first 100 s of charging, the dynamic charge efficiency Λ^* increases significantly with discharge voltage. As the total charge input is constant (41 C), this implies that the deionization also increased in the same way. In this case, however, the energy consumption is not inversely proportional to Λ^* as it is in Fig. 3-10, because the cell voltage is no longer constant. Instead, Fig. 3-11c shows how for CC-operation the energy consumption (without energy recovery) is rather invariant with V_{disch}. Interestingly, both theory and data predict a shallow minimum in the energy consumption, though at a different value of V_{disch}.

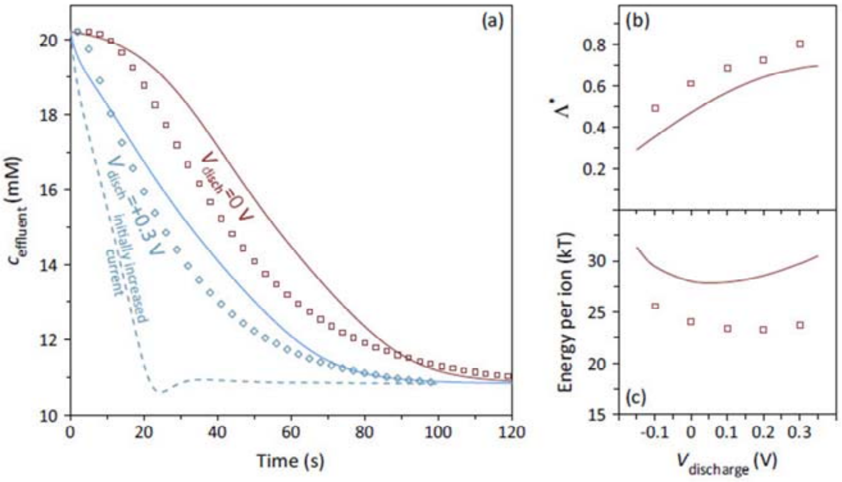

Figure 3-17. Constant-current CDI operation. (a) Effluent salt concentration as function of V_{disch} (data represented by dots; theory calculations by lines). (b) Dynamic charge efficiency vs. V_{disch}. (c) Electrical energy input per ion removed (kT) vs. V_{disch}. (I_{ch}=30.6 A/m^2, c_∞=20 mM, electrode thickness 260 μm).

3.2.5. Conclusions

In this work, we have demonstrated that the charge efficiency of a CDI cycle can be improved by increasing the discharge voltage V_{disch}. In constant voltage (CV) operation, V_{disch} up to 0.3 V was promising since the charge efficiency was significantly enhanced from 0.8 to 0.9 while the salt adsorption only minutely decreased. Another important finding was kinetics in constant-current (CC) operation: the constant level in effluent salt concentration, which is the key advantage of CC operation, was more rapidly reached when V_{disch} was increased to a value higher than zero. For CV operation, the required energy input per ion removed went down significantly when we increased the discharge voltage, for our standard experimental settings by about 14% without energy recovery during discharge, and by 30% with perfect energy recovery.

The improved modified (i-mD) Donnan model described the full experimental data set of equilibrium salt adsorption and charge to an excellent degree. Including the i-mD model in a porous electrode transport theory resulted in a dynamic theory that well illustrates several of the observed dynamic features of ion transfer and charge storage, both for constant-voltage and constant-current operation. In conclusion, our work showed that to increase system performance of CDI, there are many more options open besides developing new electrode materials, or the development of improved membranes. We demonstrate that by carefully adjusting voltage and current levels in a CDI-cycle, salt adsorption per unit charge transferred can be significantly increased, as well as the rate by which (in CC operation) a constant salt effluent level is reached.

4. Deionization Rate in Capacitive Deionization

4.1. Solvent Evaporation Mediated Preparation of Hierarchically Porous Metal Organic Framework-derived Carbon with Controllable and Accessible Large-scale Porosity

4.1.1. Introduction

Nanoporous carbon materials have been a crucial component in a variety of energy- and environment-based applications, including gas storage, separation, catalysis, electronics, water treatment, and biochemistry [154-158]. Recently, nanoporous carbon materials with hierarchical pore architectures possessing three-dimensional (3D) interconnected micro-, meso-, and macropores have provided new insights into the advanced utilization of nanoporous carbon materials [158-160]. Hierarchical pore architectures can extend the molecular selectivity and accessibility of a catalytic application and facilitate ion transport in electrochemical applications. These architectures therefore overcome the drawbacks associated with catalyst deactivation and slow reaction kinetics [158, 160, 161].

To address these pore characteristics, a host of synthetic techniques have been developed to create mesoporous features in microporous materials and vice versa

[159, 162, 163] or to simultaneously evolve hierarchical porosity by removable a template material with features on multiple length scales [158, 164]. These approaches include the incorporation of a self-assembled mesopore structure-directing molecule into a microporous carbon material synthesis procedure [165], chemical activation of a mesoporous carbon material [163], or nanocasting (or nano-replication) using colloidal silica, polymer beads, or zeolites [164, 166, 167]. Although synthetic technologies can serve as a conceptually versatile alternative for obtaining hierarchically porous carbon materials, their complicated synthesis and removal from the original template remains a challenge for practical applications. Importantly, the porosity generated by such techniques does not fulfil the demands for the pore characteristic (a high surface area with a hierarchical pore architecture) because adoption of such techniques can sacrifice the original pore characteristics of the starting carbon materials [162, 163, 168].

Xu et al. proposed a new type of nanoporous carbon material in which a metal–organic framework (MOF) and a furfuryl alcohol were used as the template and carbon precursor, respectively [156, 169]. The resultant carbons exhibited intrinsically hierarchical porosity with a relatively high specific surface area (SSA>2000 m^2/g). Consequently, outstanding performances were obtained in an evaluation of the materials as electrodes for high-rate electrochemical capacitors. Recently, the direct carbonization of MOFs without the use of additional carbon sources was found to be more effective at increasing the overall porosity [113, 170]. Despite recent progress in the use of hierarchically porous MOF-derived carbons (MDCs), the lack of systematic control over the pore characteristics continues to hinder the construction of designed pore architectures and the extension of these novel hierarchically porous carbon materials to applications.

Here, we demonstrate a template-free novel carbonization method by which hierarchically porous MDCs with a controlled-macroporosity and an ultrahigh pore volume can be realized. Solvent evaporation during heat treatment can lead to the formation of defect cracks on the surfaces of an MOF, and these cracks play an important role in the introduction of large-sized meso- and macropores within the MDC without the detriments associated with microporosity [171]. The direct thermal evaporation of a non-volatile solvent captured in the micropores of a MOF tends to slightly reduce the overall porosity and is often regarded as a process to be avoided [172-174]. We attempted to utilize this unfavorable effect to direct the reorganization of MOFs toward the production of ultrahigh porous carbon materials featuring micro-, meso-, and macropores as shown in Fig. 4-1. The new porous carbon material produced through this process can be used as a substitute for capacitive deionization (CDI) electrodes based on conventional porous carbon for the desalination of brackish water. The unique hierarchical porosity facilitated swift ion transport and, hence, large amounts of salt could be eliminated within a short period of time. The CDI performances of the benchmark materials suggested that the novel hierarchical porosity of the MDC could guide the development of new porous carbons-based materials for deionization with improved kinetics relative to the current standard.

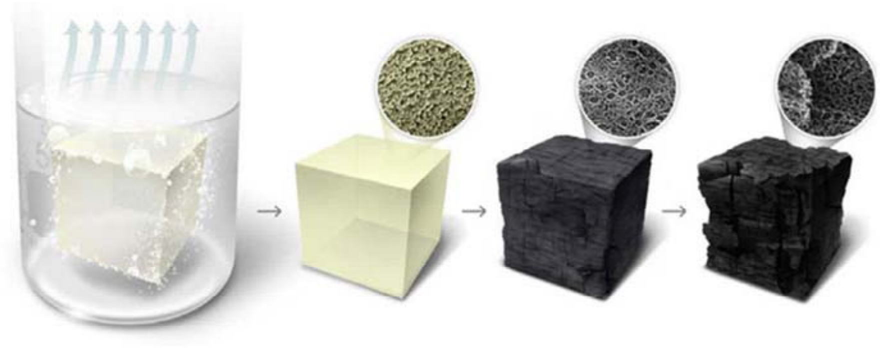

Figure 4-1. Schematics showing the formation of hierarchically porous carbon with an ultrahigh pore volume from MOFs; (a) The structural evolution of the large-sized pore seeds with micrograin boundaries by non-volatile solvent evaporation; (b) The formation of amesoporous metal oxide@carbon hybrid; (c) Micro- and macroporeswere introduced by continuously reducing the metal oxide, evaporating the metal, and carbonizing the material.

4.1.2. Experimental

Reagents and chemicals. Zinc nitrate tetrahydrate (Merck), terephthalic acid (Aldrich), N,N'-diethylformamide (DEF, Merck), N,N'-dimethylformamide (DMF, Daejung, Korea), and anhydrous chloroform (Aldrich) were used without further purification.

Synthesis of isoreticular MOF-1 (IRMOF-1). Zinc nitrate tetrahydrate (0.78 g, 3mmol) and terephthalic acid (0.17 g, 1mmol) were dissolved in DEF (30 ml) in a vial. The reaction mixture was heated in a furnace at 105^{o}C for 24 h to yield large cubic crystals of IRMOF-1. The reaction vessel was removed from the furnace and allowed to cool to room temperature.

Preparation of MDC-A, -C, and -D. The prepared IRMOF-1 was transferred to a tube furnace and heat-treated at a target temperature (900^{o}C) under nitrogen with a heating rate of 5^{o}C/min to pyrolyze the MOFs. After reaching the target temperature, the material was maintained at this temperature for 3 h and then cooled to room temperature. The MDC-A was obtained by pyrolyzing the pore-activated IRMOF-1. Guest molecules captured by the IRMOF-1 were completely removed using repetitive washing steps with DMF and anhydrous chloroform, followed by immersion in anhydrous chloroform for 12 h. The sample was then vacuum-dried at pressures less than 10^{-}3 Torr at 150°C for 24 h. The MDC-C or -D materials were obtained by pyrolyzing the IRMOF-1 while immersed in chloroform or DMF, respectively.

Characterization. X-ray diffraction (XRD) studieswere conducted using a D8 Advance (Bruker) diffractometer. Diffractograms were recorded in the reflection mode using Ni-filtered CuKa radiation (λ = 0.154184 nm). Raman spectroscopy was conducted using a RAMANplus (Nanophoton) with a 532 nm laser to analyze the surface chemical structures of the products. Volumetric nitrogen adsorption isotherms (at 77 K) up to 1 bar were measured using a Micromeritics ASAP 2020 static volumetric gas adsorption instrument. All sorption isotherms were obtained using ultrahigh-purity gases (99.999%). Prior to the sorption analysis, samples (0.1–0.2 g) in the analysis chamber were subject to a vacuum of 10^{-}5 Torr at 150°C for 12 h. Scanning electron microscopy (SEM; JSM6700F instrument, JEOL) and transmission electron microscopy (TEM; Tecnai F20, FEI) were employed for microstructure analysis.

Electrode preparation. MDC-D and commercially available carbons were used as active materials, where microporous carbon (CEP21) and meso/macroporous carbon (carbon aerogel, CA) were fabricated by PowerCarbon Technology

(Korea) and Enen (Korea), respectively. Carbon composite electrodes were fabricated using carbon materials as an active material, polytetrafluoroethylene (PTFE, Aldrich) as a binder, and carbon black (SuperP, Timcal) as a conducting agent (86:7:7 weight ratio). These components were mixed with a few ml of ethanol (Aldrich) and kneaded until it became muddy. Then, the mixture was made to have a thickness of ~360 μm using a roll press machine and was dried in a vacuum oven at 120°C for 12 h. The resulting carbon composite electrode was cut into a pair of small (18mm in diameter) and large electrodes (50mm in diameter with a 4-mm-diameter hole) for electrochemical characterizations and deionization performance analysis, respectively.

Electrochemical characterizations. Cyclic voltammetry (CV) and electrochemical impedance spectroscopy (EIS) were carried out for electrochemical characterizations in a 3-electrode configuration with 1 M NaCl using a PARSTAT 2273 (Princeton Applied Research, USA). A pair of carbon composite electrodes was served as a working and a counter electrode, and Ag/AgCl (in saturated KCl) electrode was served as a reference electrode. These electrodes were installed into a home-made electrochemical cell combined with a spacer (cellulose nitrate, Advanced Microdevices, India) and graphite current collectors. CV measurements were made by applying potential in the range of 0–0.6 V (vs. Ag/AgCl) at various scan rates (2, 10, 20, 50, and 100 mV/s). In the case of EIS, impedance was recorded over the frequency range of 10 kHz–2 mHz by applying ac voltage (10 mV vs. open circuit potential).

Deionization performance analysis. Deionization of a NaCl solution (10 mM) was carried out in a home-made CDI module. The carbon composite electrodes were pressed in the module combined with nylon (spacer) and graphite sheets (current collectors). Then, the feed solution was supplied to the module using a peristaltic pump (Gilson, Inc., USA) with a flow rate of 10 ml/min. Constant voltage of 1.2 and 0 V were applied to the CDI module using a cycler (WBCS3000, WonATech, Korea) for deionization and regeneration, respectively. During the operation, conductivity of the effluent was continuously recorded using a flow-type conductivity meter (3573-10C, HORIBA, Japan).

4.1.3. Results and Discussion

An undesirable reduction in the porosity of the IRMOF-1 can be avoided through the appropriate selection of the pore activation method applied to the IRMOF-1. Colorless cube-shaped crystals were repeatedly washed with DMF and anhydrous chloroform and soaked in anhydrous chloroform, and the exchanged guest solvent was removed under reduced pressure at 150°C [173, 175] for 20 h. In order to verify the influence of the solvent molecule during carbonization on the porosity evolution, we set up three different samples which were carbonized IRMOF-1s in the presence of a guest molecule (immersed in non-volatile DMF or volatile chloroform) or the absence of a guest molecule (complete removal using appropriate pore activation processes), and the resulting materials were denoted MDC-D, MDC-C, and MDC-A, respectively.

Characterization of the field emission-SEM (FE-SEM) micrographs (Fig. 4-2a–c and e–g) clearly revealed that the morphological evolution proceeded through different pathways depending on the presence or absence of a solvent during carbonization. MDC-A preserved the cubic morphology of the IRMOF-1 and yielded a defect-free smooth surface (Fig. 4-2c). By contrast, non-volatile solvent evaporation (MDC-D) led to the formation of an interconnected 3D wormhole-like macroporous structure (Fig. 4-2f, g and 4-3). Note that the periodically ordered texture could be readily achieved using this strategy without the need for replication or templating steps [161, 164, 165]. These properties were attributed to the highly crystalline structure of the IRMOF-1. The sample prepared using a volatile solvent (MDC-C) displayed a slightly developed macroporous texture, as shown in Fig. 4-4, suggesting that the non-volatile guest molecule played a crucial role in evolving the ordered macroporous texture. In contrast with the apparent discrepancies in the surface textures, the TEM micrographs revealed that all materials were translucent and consisted of non-graphitic thin carbon layers, similar to the microstructures of typical microporous carbons [176]. These observations indicated that solvent evaporation induced the formation of 3D ordered meso- and macroporous MDCs while maintaining the parent microporosity.

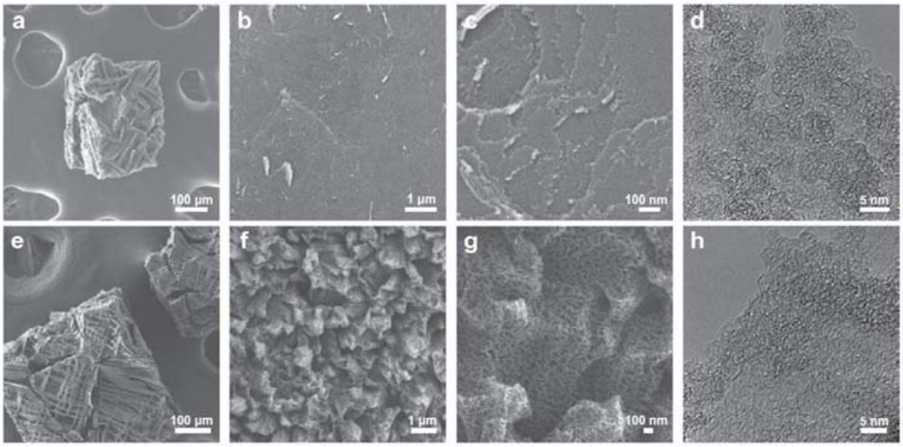

Figure 4-2. FE-SEM and TEM images of the product obtained (a–d) after pore activation (MDC-A) and (e–h) upon immersion in DMF (MDC-D).

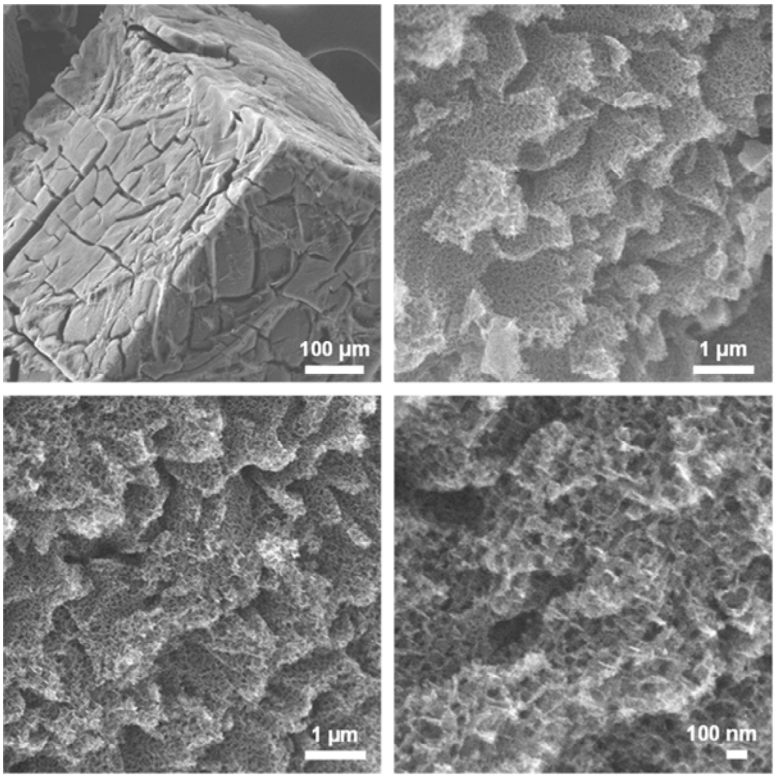

Figure 4-3. Additional FE-SEM micrographs of MDC-D.

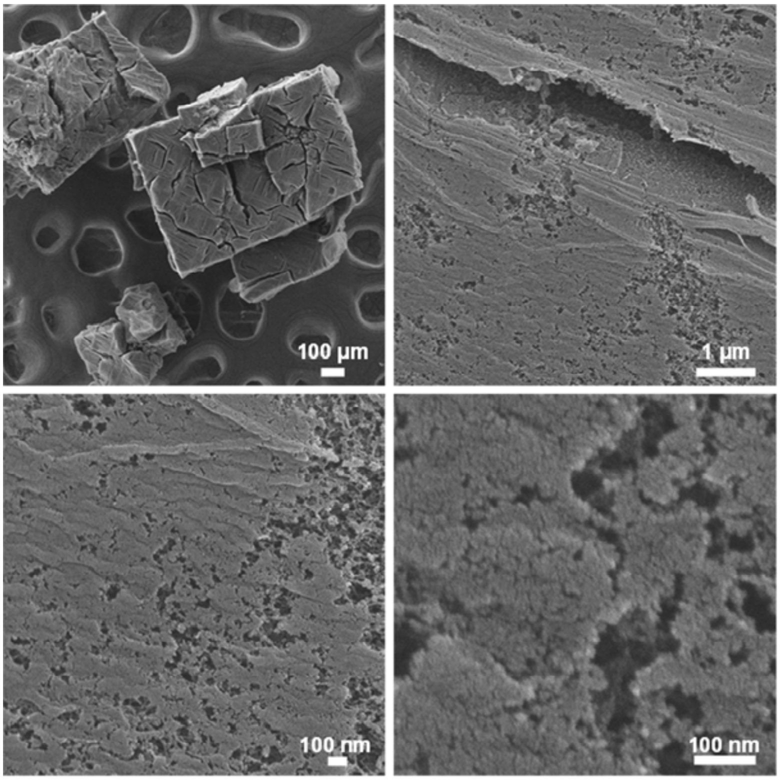

Figure 4-4. FE-SEM micrographs of the MDC-C.

The surface textural characteristics of the products were confirmed quantitatively by measuring the cryogenic nitrogen adsorption isotherms (Fig. 4-5a). All isotherms displayed the combined characteristics of type I and IV isotherms, indicating the presence of micro- and mesopores. The SEM results confirmed that the morphology induced a very steep increase at 0.85–0.99 of the relative pressure, which reached a value of 3526 cm^3/g nitrogen uptake (at $P/P_0 = 0.99$). It should be noted that the calculated total pore volume of the MDC-D was about 5.45 cm^3/g, which exceeded the highest value among the reported porous materials [164, 177]. The quantified Brunauer–Emmett–Teller (BET) SSAs were estimated to be 3110, 3200, and 2980 m^2/g for the MDC-A, -C, and -D, respectively. Considering that the SSA was mainly determined by the microporosity and the small-sized mesoporosity, these observations suggested that solvent evaporation provided an effective method for introducing large-sized pores into the resultant MDCs without sacrificing the quality or microporosity.

The effectiveness of the solvent evaporation method was investigated by determining the pore size distributions, which were extracted from the isotherms using non-local density function theory (NLDFT; micropore region: Fig. 4-5b) and the Barrett–Joyner–Halenda (BJH) model (meso- and macropore region: Fig. 4-5c). The micropore size distribution and TEM results indicated that solvent evaporation affected the microporosity of the MDCs to a limited extent. The meso- and macropore size distributions, however, displayed significant differences: The ultralarge mesopore (30–40 nm) and macropore (MDC-D) rather than small-sized mesopore (3–4 nm: MDC-A) were formed, consistent with TEM results. These novel pore characteristics, to our best knowledge, have not been reported previously and are consistent with the uniformly porous morphology observed by SEM.

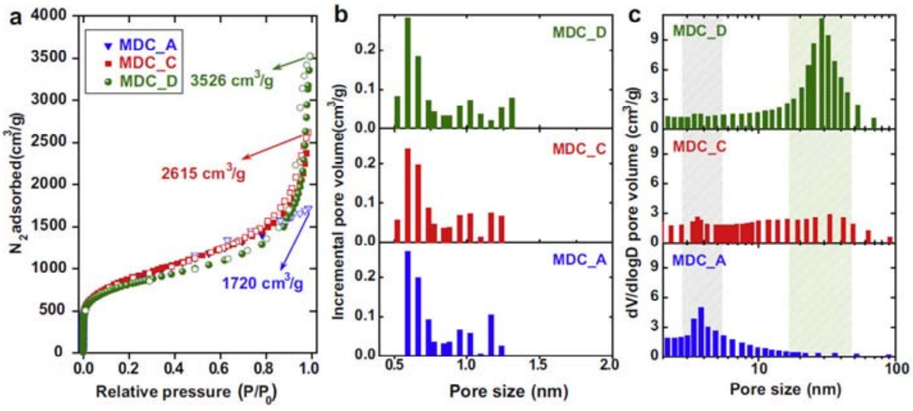

Figure 4-5. (a) Nitrogen adsorption isotherms and the corresponding pore size distributions determined using (b) the NLDFT function (microporosity) and (c) the BJH equation (mesoporosity).

The crystal structure of the materials which depended on the carbonization condition was investigated using XRD and Raman spectroscopy. The XRD patterns (Fig. 4-6a) revealed that all products consisted of a nearly amorphous carbonaceous material, as observed in the ultrahigh-porosity carbon, and the patterns were not distinguishable [113, 178]. Raman spectra (Fig. 4-6b) of the products displayed two apparent bands at 1320 and 1590 cm^{-1}, which could be assigned, respectively, to the typical D and G bands of the amorphous carbon [113, 159]. The full-width at half-maximum of the D band and the I_D/I_G ratio of the products were comparable, demonstrating a similar degree of graphitization in the products. Together with the microscopic analyses and measured pore size distributions, these observations confirmed that the microstructures and microporosity were retained, even after completely different mesoscopic structures had evolved.

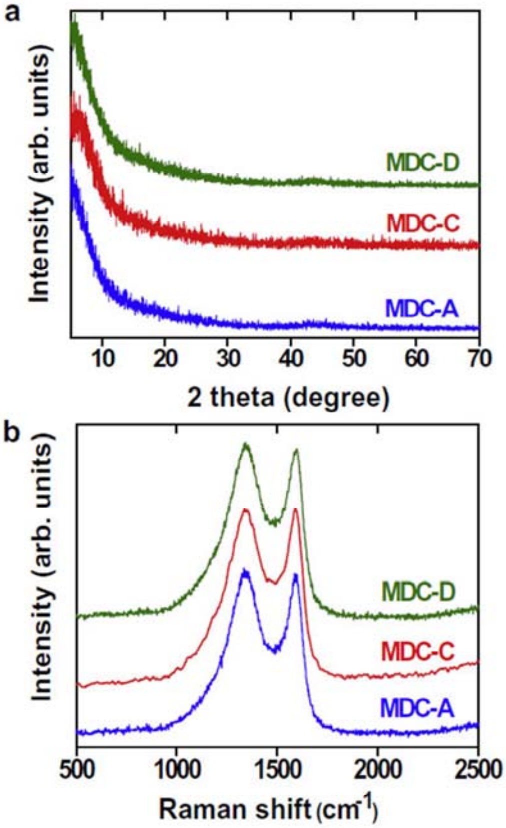

Figure 4-6. (a) XRD patterns and (b) Raman spectroscopy of the products.

Further insight into the underlying reorganization mechanism was sought by exploring the initial states of the MOFs under two sets of conditions: conventionally activated (DMF washing and chloroform exchange, followed by solvent evacuation under mild conditions: MOF_A) and directly-activated at 200^{o}C (thermal-assisted evacuation of the DMF solvent captured in IRMOF-1: MOF_D). The micrographs shown in Fig. 4-7a and b displayed significant differences in the surface morphologies, whereas the crystal structures of the products remained unaffected (Fig. 4-8). Conventional activation methods (MOF_A) yielded smoothed and defect-free surfaces, whereas thermal activation produced surfaces with defects and nanoparticle agglomerates (with a diameter distribution centered at 100 nm) [174]. Interestingly, the nanoparticles were arranged in a slightly ordered pattern, from which we presumed that these nanoparticles could be hetero-sites that developed ultrahigh meso- and macropore volumes. The N_2 adsorption isotherms (Fig. 4-7c), as expected, demonstrated a reduction in the SSA value of the MOF_D, from 3440 (MOF_A) to 3290 m^2/g. This surface transformation could lead to the introduction of large-scale meso- or macroporosity into the microporous MOFs. These effects were attributed to an increase in the N_2 adsorption near a relative pressure of 0.99 (see the inset in Fig. 4-7c). This isotherm behavior agreed well with the behavior of the MDC-D and further supported the pre-determined textural properties of the MDC-D obtained by solvent evaporation.

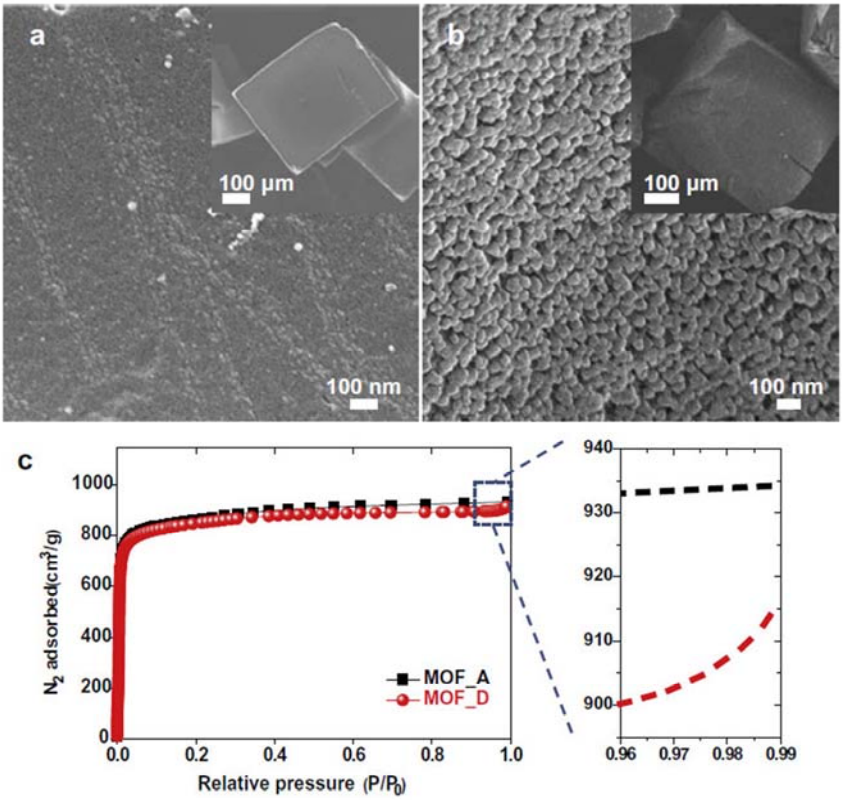

Figure 4-7. FE-SEM images of (a) MOF_A and (b) MOF_D (inset: whole image of MOF). (c) N_2 adsorption isotherms of the products.

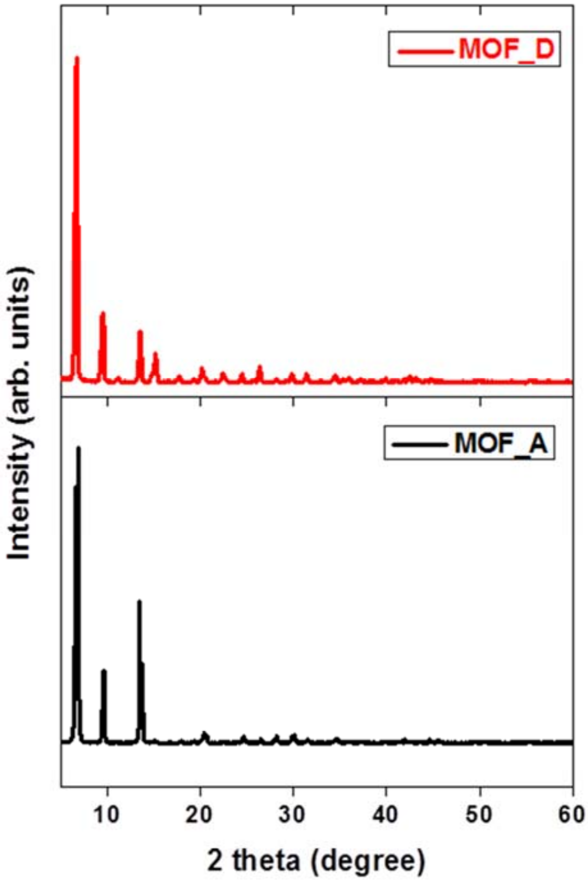

Figure 4-8. XRD patterns of the products.

To consider a whole formation process, the textural evolution of the resultant MDC-D was investigated (Fig. 4-9). Combined with these structural reorganization results, we suggested the formation mechanism of a hierarchically porous MDC-D material featuring large-scale meso- and macroporosity as shown in Fig. 4-1 and 4-9. During the early stages of the transformation, the removal of non-volatile solvents by thermal evacuation led to the formation of defects, and the granular surface consisted of nanoparticles (step a in Fig. 4-1). As the temperature was increased, the nanoparticles were transformed into the ZnO@C material while retaining their shapes, and these nanoparticles aggregated together more tightly to form a concentrated packing (step b in Fig. 4-1). Finally, further thermal treatment at high temperatures reduced ZnO following the evaporation of the Zn metal (step c in Fig. 4-1), thereby resulting in unique hierarchically porous carbons that possessed large numbers of micro-, large-sized meso-, and macropores [113, 156, 169, 170].

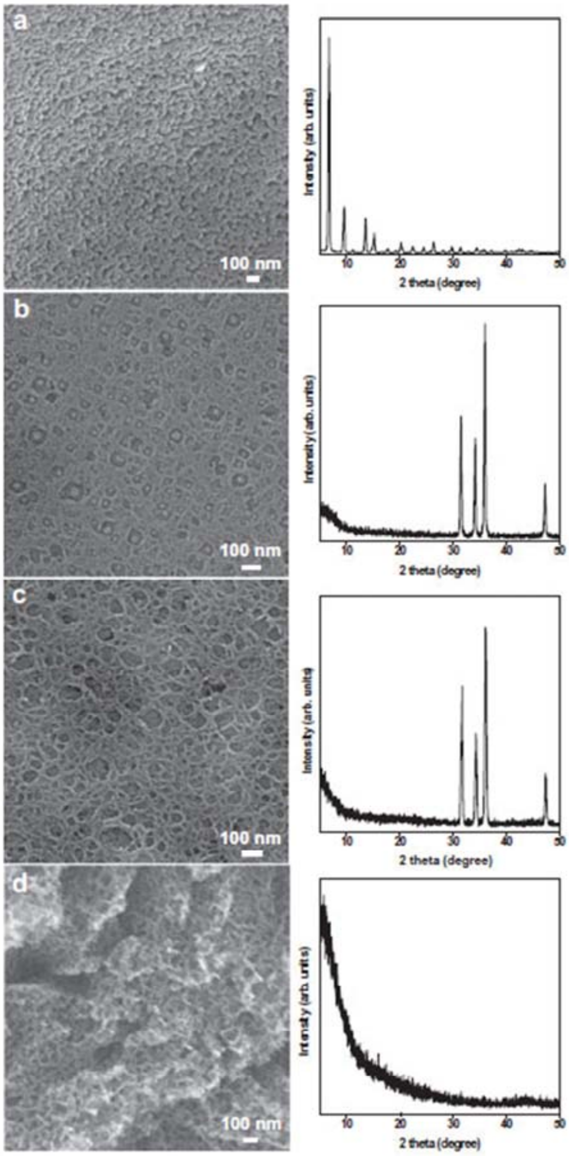

Figure 4-9. FE-SEM micrographs and XRD patterns of the carbonizing IRMOF-1 immersed in the DMF at different temperatures. (a) 200, (b) 600, (c) 800, and (d) 900°C for 3 h.

The efficacy of the hierarchically porous MDCs as electrode materials was evaluated by examining the electrochemical behaviors of the materials (Figs. 4-10 and 4-11 to 4-13), particularly in comparison with MDC-D, a typical microporous carbon (CEP21), and a commercialized meso- and macroporous CA in a 1 M NaCl solution (Fig. 4-14). CV profiles were recorded at different scan rates (Fig. 4-10a), demonstrating the excellent rate performance of MDC-D. The rectangular shape was preserved without remarkable distortion as the scan rate increased from 2 to 100 mV/s. This result indicated that the electrolyte ions could be rapidly transported inside the pore structures of the electrode. The frequency-dependent capacitance (Fig. 4-10b), which was obtained using EIS, also agreed well with the CV results. The MDC-D exhibited a much higher capacitance at high frequencies (0.1–10 Hz) compared to the other carbon electrodes. The excellent rate performance of the MDC-D was ascribed to the unique hierarchic pore architecture. Large-scale meso- and macropores provided transport channels that allowed the rapid transport of electrolyte ions [4, 158]. Similar performances were observed in the case of CA, which mainly consisted of large-scale meso- and macropores, although the capacitance of this material was due to a lack of micropores (Fig. 4-14a). On the other hand, micropores provided a high surface area and a subsequent high capacitance, as in the case of CEP21. The pore characteristics of CEP21, however, were disadvantageous for the rapid transport of electrolyte ions, leading to a significant deterioration in the capacitance at fast scan rates and high frequencies (Figs. 4-10a and 4-14b). A rapid rate performance, accompanied by a high capacitance, could be realized by MDC-D because its hierarchical pore architecture possessed micropores, mesopores, and even macropores. The unique electrochemical behavior of MDC-D was especially beneficial to CDI applications that required the removal of large amounts of salt within a few minutes to achieve effective deionization. As confirmed by Fig. 4-15a, MDC-D rapidly removed NaCl from the feed solution (top) with good recyclability (bottom). Importantly, the deionization capacity (the integrated number of deionized ions) of the MDC-D was much higher during the initial phase of deionization (Fig. 4-15b). This behavior clearly illustrated the superior performance of MDC-D as a novel CDI electrode. Microporous carbons typically provide a long diffusion distance and a high ion transport resistance (Fig. 4-16a); therefore, the unique hierarchical pore structure of the MDC-D may have shortened the diffusion distance from the external electrolyte to the interior surface and minimized the ion transport resistance (Fig. 4-16b), which then contributed to the rapid deionization process [4, 39, 158, 179].

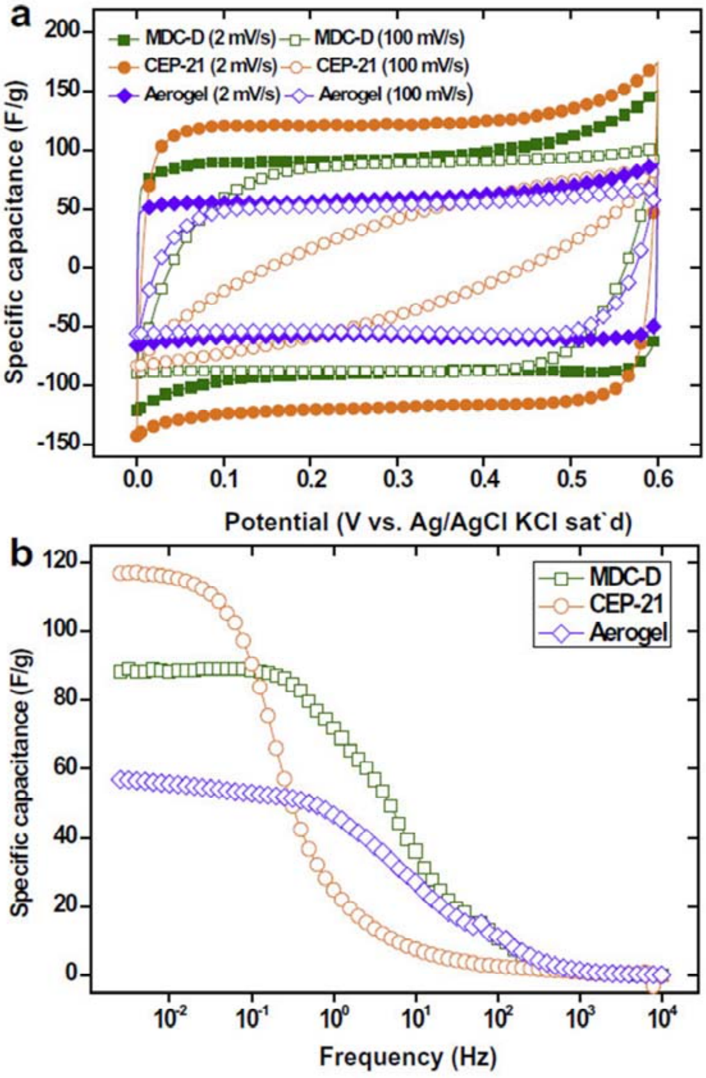

Figure 4-10. (a) CVs and (b) Frequency-dependent capacitance of MDC-D, CEP21, and CA.

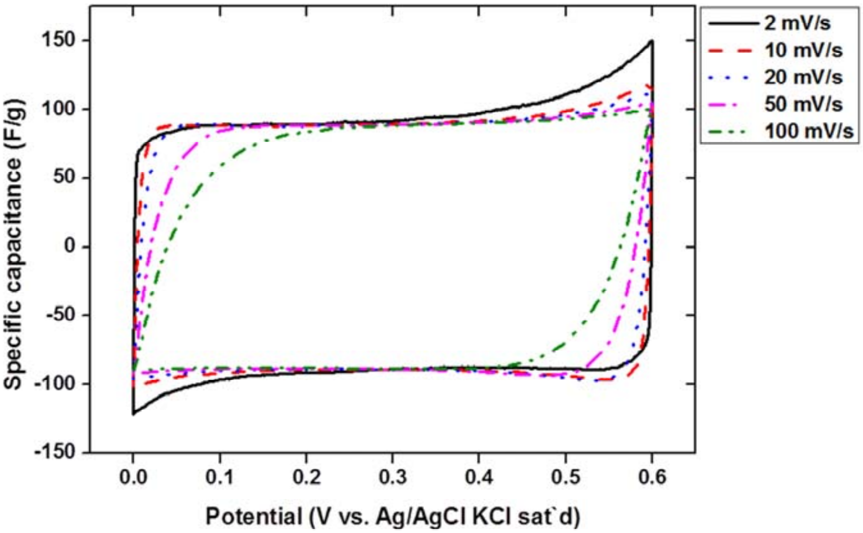

Figure 4-11. Cyclic voltammograms of the MDC-D recorded at various scan rates.

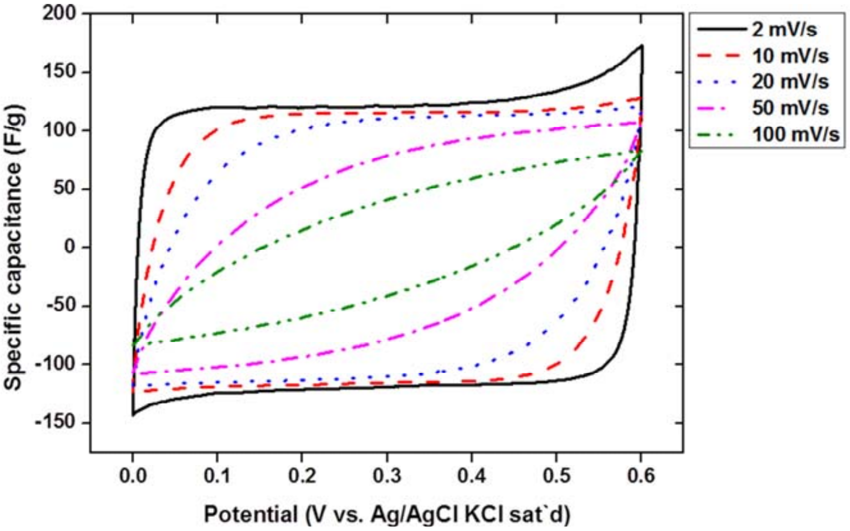

Figure 4-12. Cyclic voltammograms of the microporous carbon (CEP-21) recorded at various scan rates.

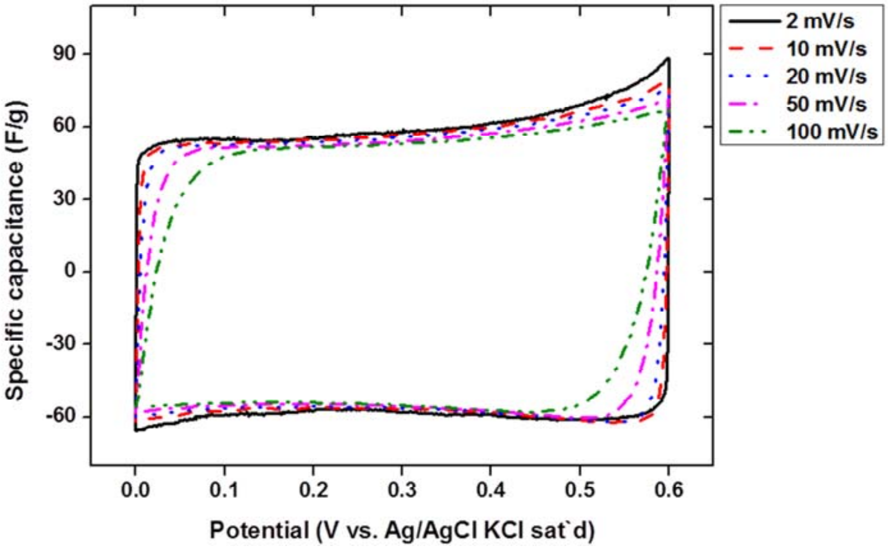

Figure 4-13. Cyclic voltammograms of the carbon aerogel (CA) recorded at various scan rates.

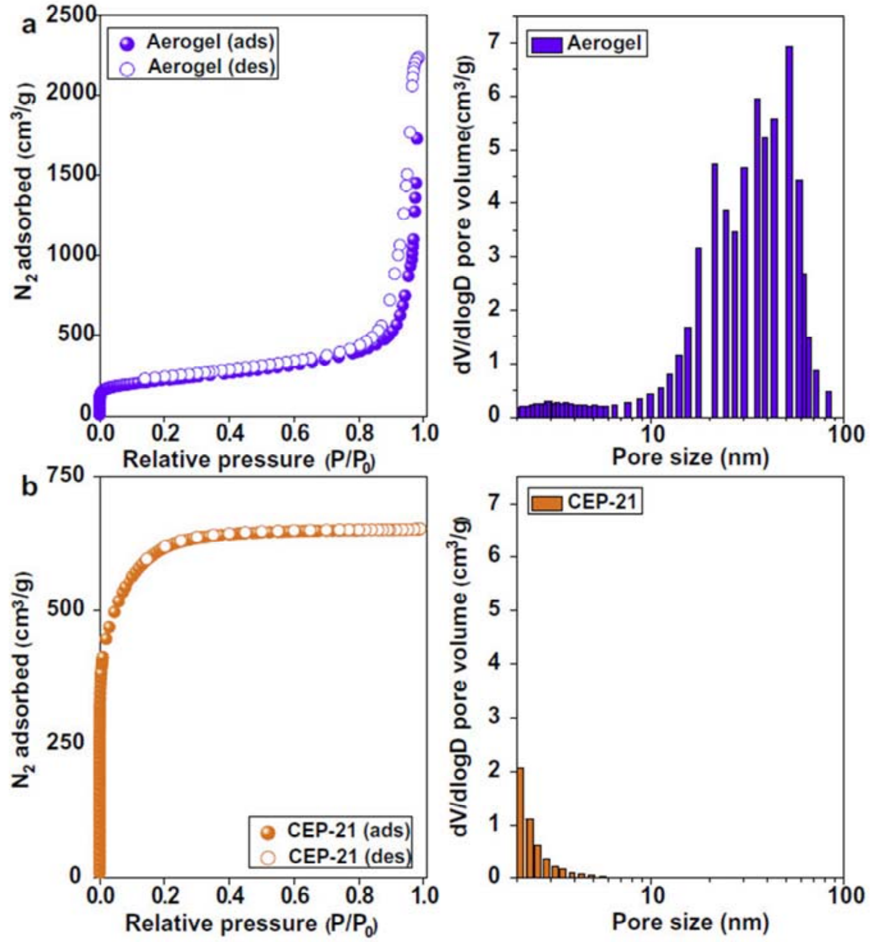

Figure 4-14. Nitrogen adsorption isotherms and corresponding meso- and macropore size distribution of (a) CA and (b) CEP21. Calculated BET SSA with total pore volume at 0.99 of relative pressure of CA and CEP21 are 790 (3.45) and 2210 m^2/g (1.00 cm^3/g), respectively.

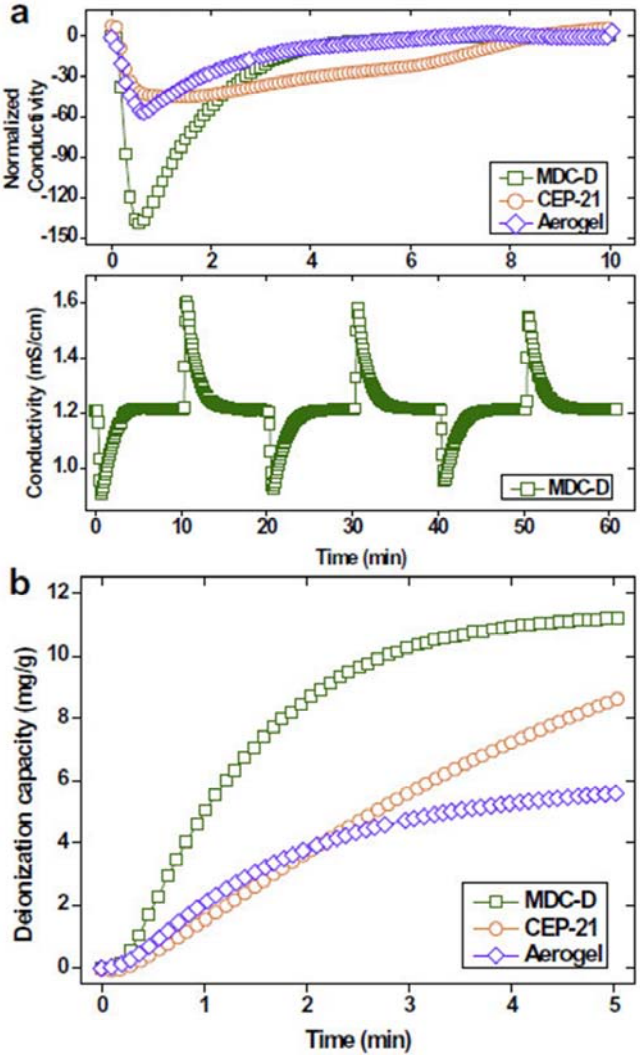

Figure 4-15. (a) conductivity changes in the effluent (top) and recyclability of MDC-D (bottom), and (b) deionization capacity (the integrated number of deionized ions per gram electrode) as a function of time.

Figure 4-16. Schematics showing the pore characteristics of a typical microporous carbon material (left) and a hierarchically porous MDC-D (right).

4.1.4. Conclusions

We demonstrated that solvent evaporation during the carbonization of MOFs led to the formation of large-sized meso- and macropores with a uniform distribution without the need for a template or replication steps. The resultant materials displayed a novel hierarchical pore architecture featuring micro-, meso-, and macropores and the highest pore volume yet reported among ultrahigh porous materials. The electrochemical performance of the novel hierarchical porous carbon revealed the role of a pore structure in a CDI. The micropores, along with the mesopores and macropores, provided ion storage sites and ion transport channels, respectively, that contributed to the outstanding deionization performance of MDC-D (rapid removal of NaCl). The resulting deionization capacity at 1 min was higher (5.0 mg/g) compared to CA (2.1 mg/g) and CEP21 (1.5 mg/g). The easy synthesis procedure introduced here may suggest new methods for the design of porous carbon from a MOF, and the unique hierarchical pore architecture may potentially be expanded to other microporous carbon materials that display kinetically limited properties during an electrochemical reaction.

4.2. Potential Sweep Method to Evaluate Rate Capability in Capacitive Deionization

4.2.1. Introduction

With growing attention on capacitive deionization (CDI), a variety of approaches have been recently investigated to understand and improve the deionization performance [2, 180]. These efforts include applications of new electrode material [4, 15, 66, 86, 111, 181], development of novel systems [22, 53, 82], electrochemical analysis [24, 104, 119, 127], modeling [10, 17, 25], and energy management [39, 123, 182]. Among them, electrochemical analysis has been recognized as the most significant method to investigate the performance of an electrode system. The analysis provides the capacitive behavior of an electrode upon charging of the electrode, which is a crucial requirement for CDI. Therefore, the electrochemical properties of an electrode are quite important in understanding deionization performance in CDI.

Capacitance has been considered as the most significant electrochemical property in many fields because it intuitively indicates the amount of charge upon charging. Compared to the energy density in energy storage devices, the charge capacity could represent the amount of ionic charges that are desalinated in a CDI system. Hence, many CDI studies have focused on measuring capacitance by means of electrochemical characterization methods such as cyclic voltammetry, galvanostatic charge/discharge tests, and electrochemical impedance spectroscopy [24, 83, 105, 119]. The same methods also have been utilized to investigate the rate performance, in which rate-dependent capacitance was obtained by altering the scan rate, current density, and frequency.

Despite intensive efforts to understand the capacitive behavior of an electrode in CDI, the rate capability of deionization, which provides the ability of the electrode to realize rapid deionization, has been poorly defined. So far, the rate performance of deionization has been reported by adopting conventional adsorption equations [7], dividing the adsorption capacity by time [82], and developing model equations [10]. However, these approaches have provided the rate performance for deionization in a fixed condition; therefore, little is known about the ability of an electrode to respond to various deionization rates. Previous studies examining the rate-dependent deionization performance have shown the effects of various current densities on effluent conductivity, salt adsorption, and the average salt adsorption rate under constant current operations [17, 39]. This approach will be extended and further examined in the present study, especially focusing on the rate-dependent deionization performance. In this manner, the rate capability of deionization can be determined, which would be an important indicator in CDI.

This study demonstrated the evaluation of the rate capability of CDI by introducing a potential sweep method. Deionization performance was obtained at different scan rates, and the resulting deionization capacity was converted to determine the rate capability. In particular, electrode thickness was selected as one of the parameters affecting the rate capability. Moreover, the capacitive behavior of the electrode from different thicknesses was specifically analyzed by electrochemical characterizations.

4.2.2. Materials and Methods

Electrode preparation. Carbon composite electrodes were fabricated with 86 wt% MSP-20 (2,223 m^2/g, Fig. 4-17, Kansai Coke and Chemicals, Japan), 7 wt% carbon black (Super P, Timcal), and 7 wt% polytetrafluoroethylene (PTFE, Aldrich). After these components were homogeneously mixed in an agate mortal with ethanol, it was kneaded to yield a gummy mixture. Then, it was pressed with a roll-pressing machine; carbon composite electrodes at different thicknesses (200, 300, and 400 μm, Table 4-1) were obtained by adjusting the gap between two of the rollers in the machine. The resulting electrodes were dried in a vacuum oven at 120°C for 12 h.

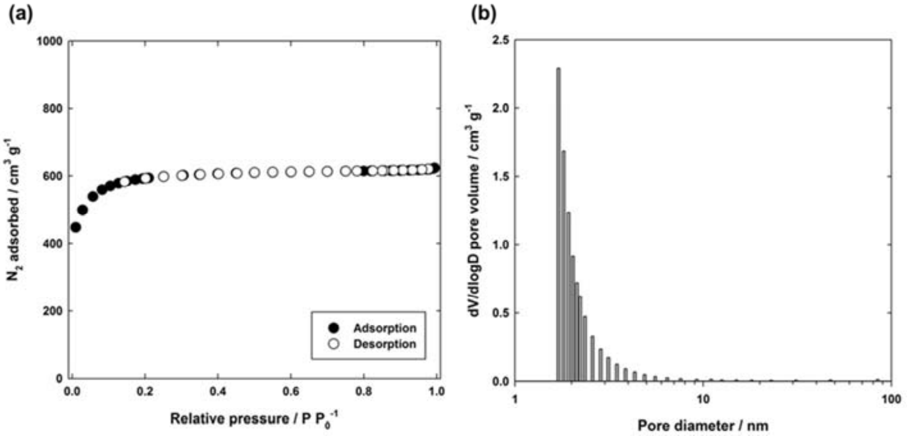

Figure 4-17. (a) Nitrogen adsorption isotherm and (b) pore size distribution of MSP-20.

Table 4-1. Information on the electrodes used in this study.

Electrode	Thickness/μm	Mass[a]/mg	Density[b]/g cm^{-3}
200 μm	198±6	62±2	1.04±0.05
300 μm	305±18	96±5	1.04±0.02
400 μm	408±10	127±5	1.03±0.02

[a] Both electrodes (cathode and anode)

[b] Volume was calculated by the thickness multiplied by the electrode area (3.02 cm^2).

Electrochemical characterizations. The electrochemical performance of the carbon composite electrodes was investigated with cyclic voltammetry (CV) and electrochemical impedance spectroscopy (EIS). To carry out the analysis, the electrodes were cut into round pieces (18 mm in diameter), and a pair of electrodes was installed to an electrochemical cell with a separator and current collectors. After the installation, the cell was filled with 1 M NaCl and tightly sealed. CV was carried out in a 3-electrode system; Ag/AgCl in a saturated KCl solution was used as a reference electrode, and the carbon composite electrodes were used as a working and counter electrode. Potential was applied to the cell ranging from -0.1 to 0.5 V at various scan rates (2, 10, 20, and 50 mV) with a PARSTAT 2273 (Princeton Applied Research, USA). EIS was conducted in a 3-electrode system (same as in the case of the CV), and impedance data were collected between 0.002–10,000 Hz by applying ac 10 mV at an open circuit potential. The collected impedance data were converted to capacitance with the following equation:

$$C = -1/(2\pi f \times Z_{im}) \tag{1}$$

, where Z_{im} is the imaginary part of the impedance and f is the frequency (Hz).

CDI performance tests. Fig. 4-18 shows a schematic diagram of the experimental setup. Carbon composite electrodes, which were cut into round pieces (20 mm in diameter) with a hole (4 mm in diameter) located at the center, were installed into a custom-built CDI module with graphite current collectors. Then, anion- and cation-exchange membranes (selemion, AGC ENGINEERING CO., LTD, Japan) and a polymer spacer were assembled and sealed together with the electrodes (membrane-assisted CDI). Experiments were carried out in a single-pass mode. A feed solution (10 mM NaCl) was supplied to the CDI module with a peristaltic pump (flow rate=2 ml/min). The solution went inward from the outside through a spacer between the electrodes, and the effluent conductivity was continuously recorded with a flow-type conductivity meter (3574-10C, HORIBA, Japan). Changes in pH were neglected because their contribution was insignificant (see Fig. 4-19). To evaluate the rate capability, a potential sweep method was introduced for controlling the CDI module with a cycler (WBCS3000, WonATech, Korea); the module was charged from 0 to 1.2 V at different scan rates (2, 4, 8, 12 mV/s), and it was discharged by short-circuiting until the conductivity returned to the initial value. These two steps were repeated 3 times and the 3rd cycle was used as a representative result for each condition (the performance became stable since 3rd cycle, see Fig 4-20). For the analysis, deionization capacity (the mass of deionized NaCl (mg) divided by the mass of both carbon electrodes (g))[24] obtained at each scan rate was normalized (the ratio of deionization capacity of a certain scan rate to that of 2 mV/s) to indicate deteriorated deionization performance as the scan rate and the electrode thickness increased. To obtain the mean deionization rate (mg/g/s, deionization capacity divided by the duration of charging) [82] under constant current operations, the module was charged at a constant current (2, 5, 9, 15 mA) with a cutoff voltage of 1.2 V followed by short-circuiting for discharging. All experiments were carried out in a temperature chamber at 25°C.

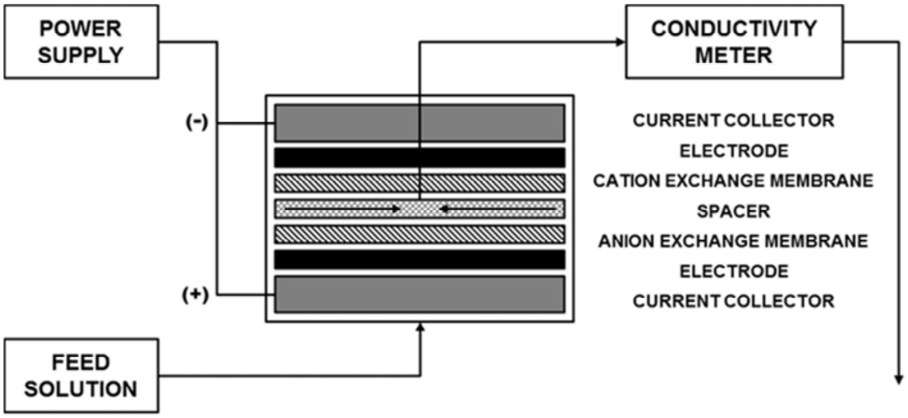

Figure 4-18. A schematic diagram of an experimental setup for the CDI tests. For the deionization, the CDI module was charged and discharged with a power supply which was connected to the current collectors inside the module. Feed solution (10 mM NaCl) passed through a spacer from outside to the center, which was located between the cation- and anion-exchange membranes. Then, the effluent conductivity was continuously recorded using a flow-type conductivity meter.

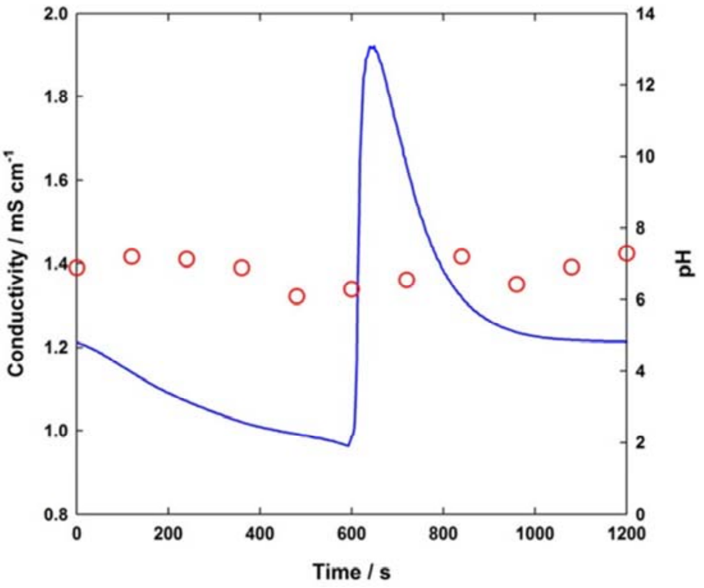

Figure 4-19. Representative conductivity and pH profiles as a function of time in potential sweep operation (electrode thickness=300 μm, scan rate=2 mV/s).

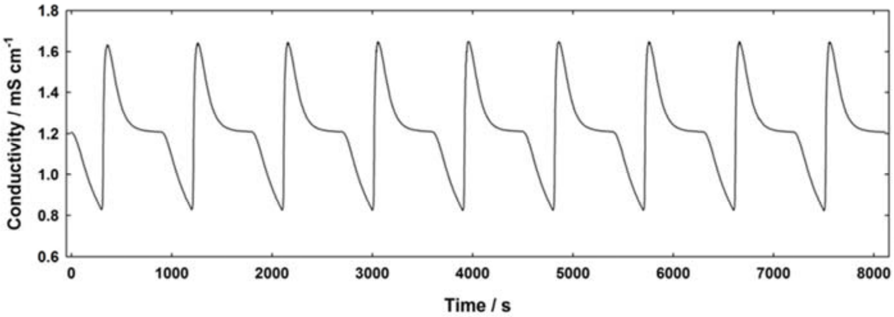

Figure 4-20. Representative cycle performance of the 300-μm-thick electrode at a scan rate of 4 mV/s.

4.2.3. Theory

Impedance data collected by EIS can be used to differentiate various terms included in the system through an equivalent circuit analysis. In particular, the system was described according to the transmission line model combined with pore size distribution (TLM-PSD) with the following equations:

$$\mathbf{Z}(f) = R_{\text{bulk}} + \mathbf{Z}_{\text{interface}} + \mathbf{Z}_{\text{pore}} \tag{2}$$

$$\mathbf{Z}_{\text{pore}} = 1/[j\omega\mathbf{C}_{\text{TLM-PSD}}(f)] \tag{3}$$

$$\mathbf{C}_{\text{TLM-PSD}}(f) = C_{\text{tot}}\int_{-\infty}^{\infty}\mathbf{C}^0(f, \alpha_{\text{o}})p(\alpha_{\text{o}})d\ln\alpha_{\text{o}} \tag{4}$$

, where $\mathbf{C}^0$ is the unit complex capacitance of a single TLM element [26]; $p(\alpha_o)$ is the log-normal distribution function [183-185]; f is the frequency (Hz); C_{tot} is the total capacitance (F/g); ω is the angular frequency ($2\pi f$); and α_o is the penetrability coefficient ($s^{-0.5}$). $\mathbf{C}^0(f, \alpha_o)$, $p(\alpha_o)$, and α_o can be described with the following equations [185-187]:

$$\boldsymbol{C}^0(f, \alpha_{\text{o}}) = \alpha_{\text{o}}/\sqrt{j\pi f}\tanh\left(\sqrt{j\pi f}/\alpha_{\text{o}}\right) \tag{5}$$

$$p(\alpha_{\text{o}}) = 1/(\sqrt{2\pi}\sigma)\exp[-(\ln\alpha_{\text{o}} - \ln\alpha_{\text{o}}^*)^2/(2\sigma^2)] \tag{6}$$

$$\alpha_0 = \alpha\sqrt{2\pi f} \tag{7}$$

, where σ is the degree of distribution, α is the ionic penetrability and α_o^* is the characteristic penetrability coefficient. The ionic penetrability is a dimensionless variable and defined as the penetration depth of an ac signal with respect to the average pore length. It is maximized if we use favorably structured electrodes, a highly conductive electrolyte, and low frequency ac signal. The characteristic penetrability coefficient, α_o^*, is inversely proportional to the average pore length shown by the following equation:

$$\alpha_0^* = 0.5\sqrt{\kappa r/(C_\mathrm{d} l^2)} \tag{8}$$

, where l is the average pore length (cm); r is the average pore radius (cm); C_d is the double-layer capacitance per area (F cm^{-2}); and κ is the ionic conductivity (Ω^{-1} cm^{-1}). The average pore length can be defined as the average pathway of the ionic charge inside the electrode until it is adsorbed to the electrode surface [185]. Note that this theory is valid in high ionic concentrations (e.g., 1 M NaCl) but may fail in lower ionic concentrations.

4.2.4. Results and Discussion

Fig. 4-21 shows representative effluent conductivity profiles obtained at different scan rates with respect to the electrode thickness. As can be seen in the figure, the conductivity linearly decreases with the charging of the module, and its slope becomes steeper as the scan rate increases. Interestingly, the profiles show an intermediate behavior compared to constant voltage charging and constant current charging; the typical profile of constant voltage exhibits a sharp drop followed by a gradual increase [24, 111], and that of the constant current shows a constant conductivity value [39]. For the different electrode thicknesses with the same scan rate, we observed that the area below the influent conductivity (~1.2 mS/cm) becomes larger as the thickness increases from 200 μm (Fig. 4-21(a)) to 400 μm (Fig. 4-21(c)), indicating different carbon loadings depending on the thickness. The thicker electrodes contain a higher carbon loading within the same area, thus exhibiting more charging with the corresponding deionization.

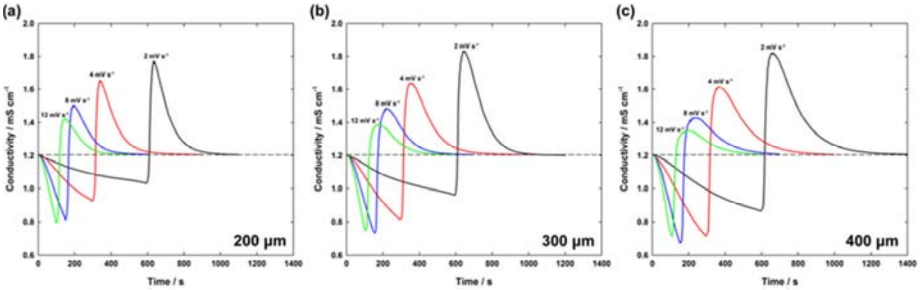

Figure 4-21. Representative effluent conductivity profiles as a function of the scan rate for different electrode thicknesses ((a) 200, (b) 300, and (c) 400 μm). The module was charged from 0 to 1.2 V at different scan rates (2, 4, 8, 12 mV/s) followed by short-circuiting until the conductivity returned to the initial value.

Fig. 4-22 shows the deionization capacity, charge, and dynamic charge efficiency as a function of the scan rate for different electrode thicknesses. In Figs. 4-22(a)–(c), we observed that the deionization capacity and charge decrease as the scan rate increases. In addition, the deionization capacity and charge of the 200-μm-thick electrode (Fig. 4-22(a)) at the same scan rate were the highest (16.5 mg/g and 32.5 C/g at 2 mV/s) followed next by those of 300- (Fig. 4-22(b), 14.9 mg/g and 30.1 C/g at 2 mV/s) and 400-μm-thick electrode (Fig. 4-22(c), 14.1 mg/g and 27.7 C/g at 2 mV/s). It can be inferred that the thinner electrode is favorable for charging and subsequent the deionization, thus resulting in better deionization performance compared to the thicker electrodes. In addition, the gap between the deionization capacity and charge increased as the scan rate increased. This change indicates that the ratio of deionization capacity to the total charge that transferred to the electrode, which is defined as the dynamic charge efficiency [25, 39], decreases as the scan rate increases. As confirmed in Fig. 4-22(d), the dynamic charge efficiency decreased with an increasing scan rate. Comparing the dynamic charge efficiency between the different electrode thicknesses at each scan rate, a marginal difference was found regardless of the thickness.

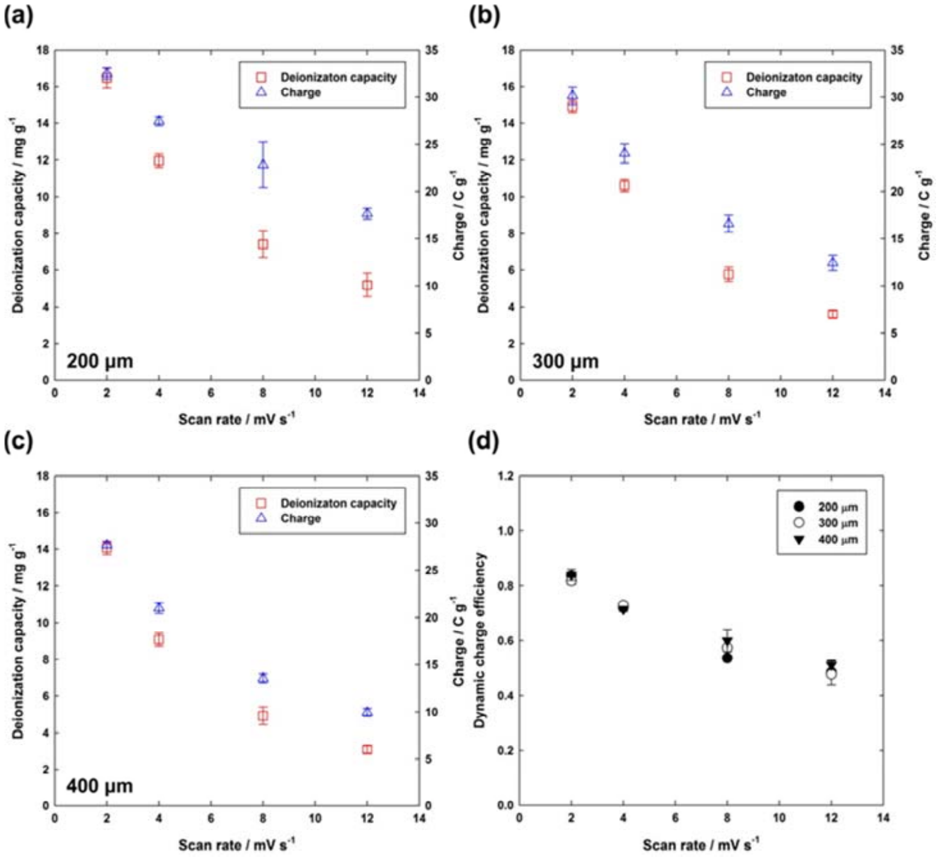

Figure 4-22. Deionization capacity, charge, and dynamic charge efficiency as functions of the scan rate and electrode thickness. Deionization capacity (rectangle) and charge (triangle) were obtained from the conductivity meter and the cycler for (a) 200-, (b) 300-, and (c) 400-μm-thick electrodes. (d) The dynamic charge efficiency was calculated by dividing the deionization capacity by the total charge that transferred to the electrode.

Next, the rate capability of deionization was evaluated which is the main result of this study. As shown in Fig. 4-23, the retention ratio (deionization capacity of each scan rate divided by that of 2 mV/s) decreases as the scan rate increases. In particular, less reduction was found in the thinner electrode, indicating a better rate capability compared to the thicker electrodes. The retention ratio of the 200-μm-thick electrode was 0.45 at 8 mV/s, and that of 300- and 400-μm-thick electrode were 0.39 and 0.35, respectively. This result indicates that the thickness of an electrode is one of the factors affecting the rate capability; a thinner electrode is able to exhibit a better deionization performance in terms of the deionization capacity (mg/g) when it is rapidly charged in order to desalinate more salts within a short time. Also, flow rate and salt concentration also affected rate capability together with electrode thickness (see supporting information, Figs. 4-24 to 4-29). Considering the result in Fig. 4-22, the charging property of an electrode would be attributed more to the rate capability depending on the electrode thickness rather than the transport of counter- and co-ions; the decrease in the charge (Figs. 4-22(a)–(c)) with an increasing scan rate was remarkable while the charge efficiency (Fig. 4-22(d)) was similar regardless of the thickness at each scan rate. Therefore, it can be concluded that the capacitive behavior of an electrode is quite important for the rate capability of deionization in CDI.

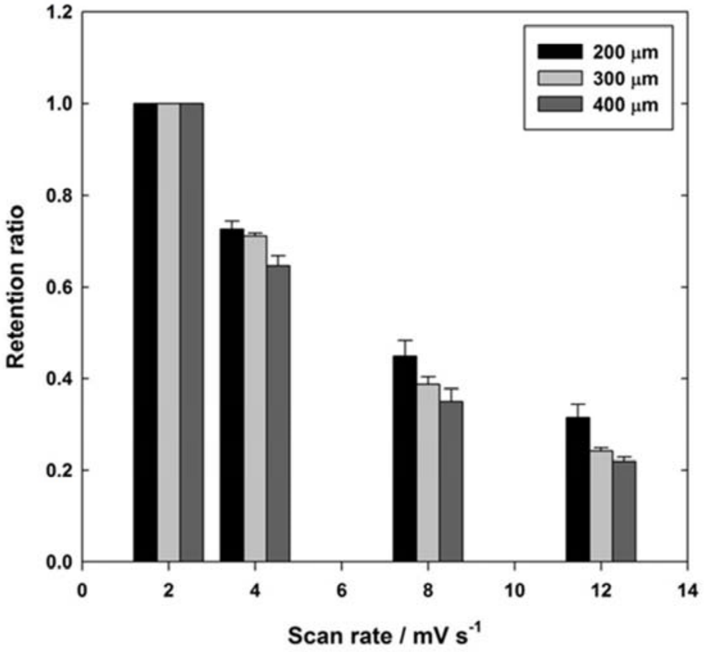

Figure 4-23. Retention ratio of the deionization capacity as a function of the scan rate for different electrode thicknesses. The retention ratio was calculated by dividing the deionization capacity of each scan rate by that of 2 mV, indicating the rate capability.

Fig. 4-24 shows representative conductivity profiles obtained at different flow rates (1, 2, 4 ml/min, electrode thickness=300 µm, scan rate=4 mV/s). As can be seen, the lower effluent conductivity was achieved for the lower flow rate, which is in good agreement with the previous study (Zhao et al., *Water Research* 47 (2013) 1941-1952). The collected data at various scan rates (2, 4, 8, 12 mV/s) was converted for quantitative analysis. Fig. 4-25 shows deionization capacity, charge, and dynamic charge efficiency as a function of scan rate, which were obtained at different flow rates. As can be observed, higher deionization capacity and dynamic charge efficiency were achieved as the flow rate increased. In particular, higher retention ratio was obtained with increasing flow rate (Fig. 4-26), indicating better rate capability. Therefore, it can be inferred that flow rate is another parameter determining rate capability together with electrode thickness.

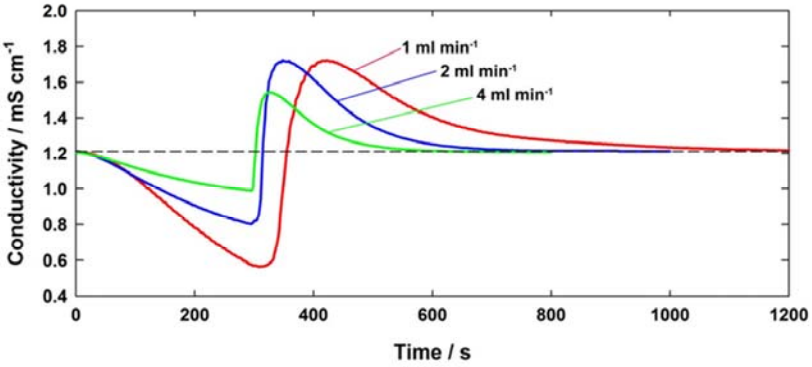

Figure 4-24. Representative conductivity profiles obtained at different flow rates (electrode thickness=300 μm, scan rate=4 mV/s).

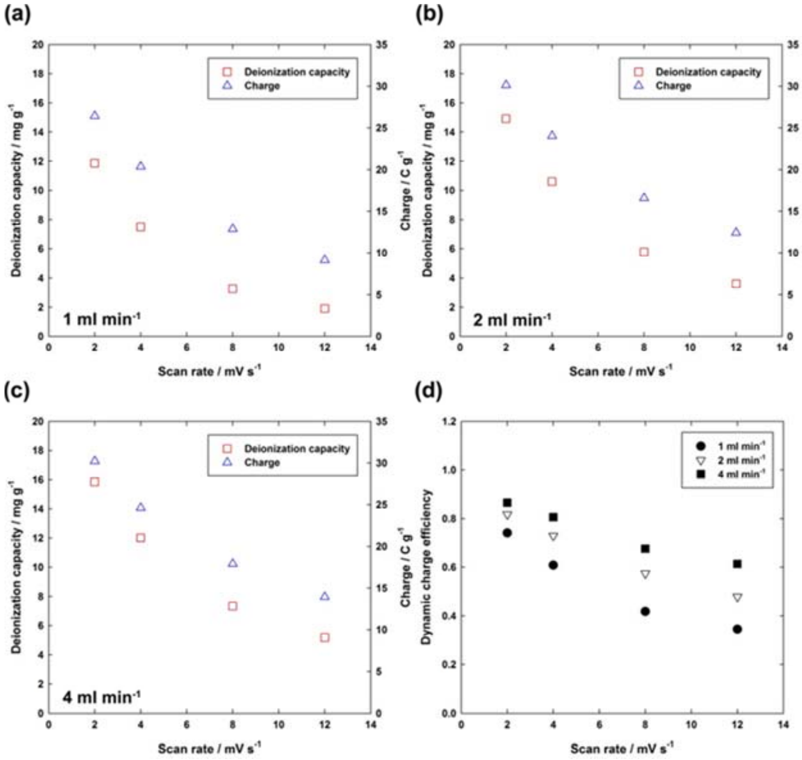

Figure 4-25. Deionization capacity, charge, and dynamic charge efficiency as a function of scan rate for different flow rates (electrode thickness=300 μm).

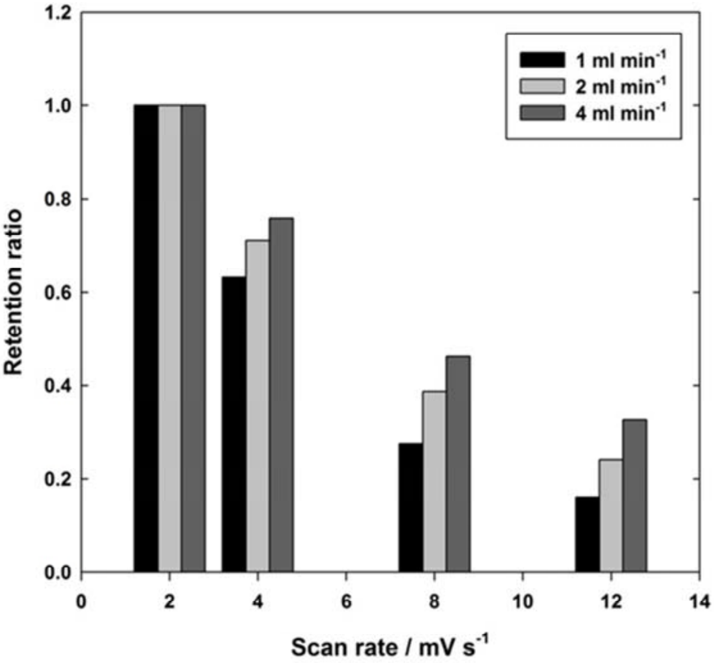

Figure 4-26. Retention ratio as functions of scan rate and flow rate (electrode thickness=300 μm).

We also carried out the same analysis on different salt concentrations (2, 10, 50 mM). Fig. 4-27 shows representative conductivity profiles obtained at 2, 10, and 50 mM NaCl solutions. As can be observed, more rapid decrease was achieved with the higher salt concentration, which is mostly due to lower resistance of electrolyte and subsequent swift transport of ions. Also, we observe that more area below a base line for the higher salt concentration, indicating higher deionization capacity. As confirmed in Fig. 4-28, higher deionization capacity was obtained at every scan rate as salt concentration increases. Interestingly, dynamic charge efficiency decreased with increasing scan rate, but was found to be similar regardless of salt concentration at each scan rate. Finally, retention ratio, deionization capacity of each scan rate divided by that of 2 mV/s, was obtained in Fig. 4-29. As expected, better rate capability was achieved at the higher salt concentration. Therefore, it can be inferred that salt concentration one of parameters determining rate capability together with flow rate and electrode thickness.

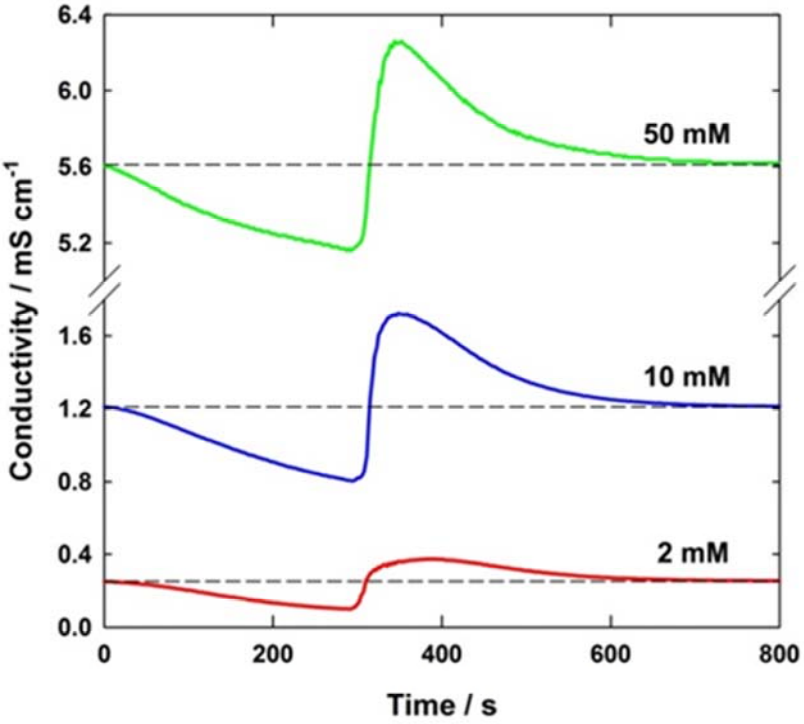

Figure 4-27. Representative conductivity profiles obtained at different salt concentrations (electrode thickness=300 μm, scan rate=4 mV/s).

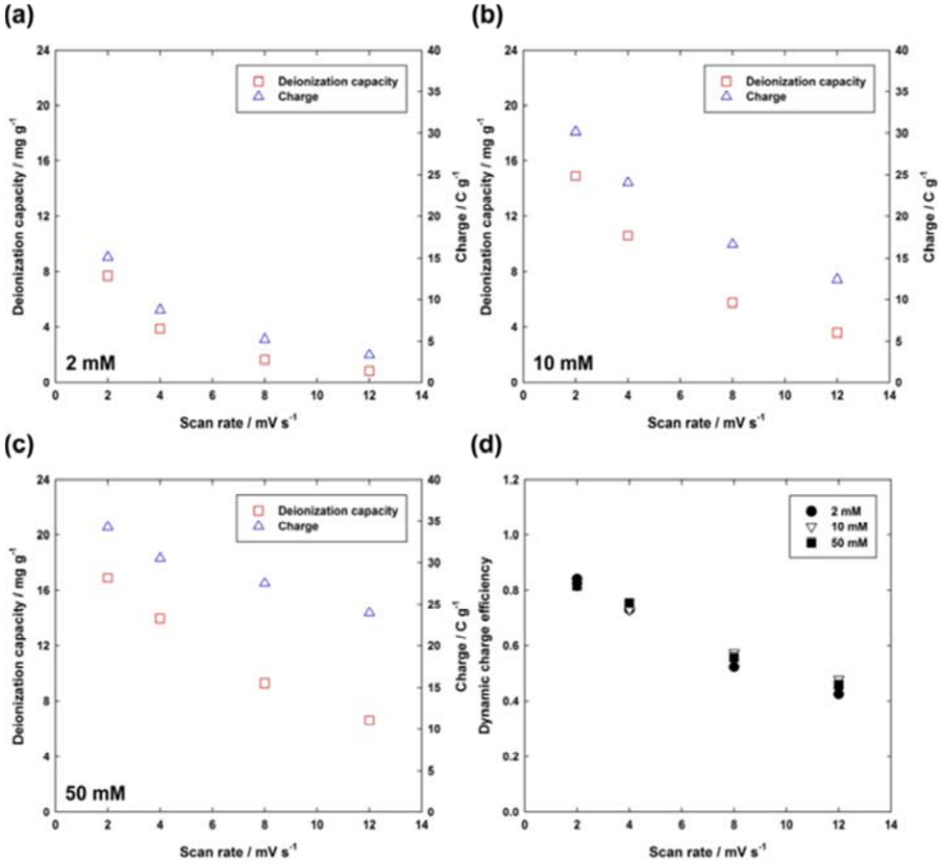

Figure 4-28. Deionization capacity, charge, and dynamic charge efficiency as a function of scan rate for different salt concentrations (electrode thickness=300 μm).

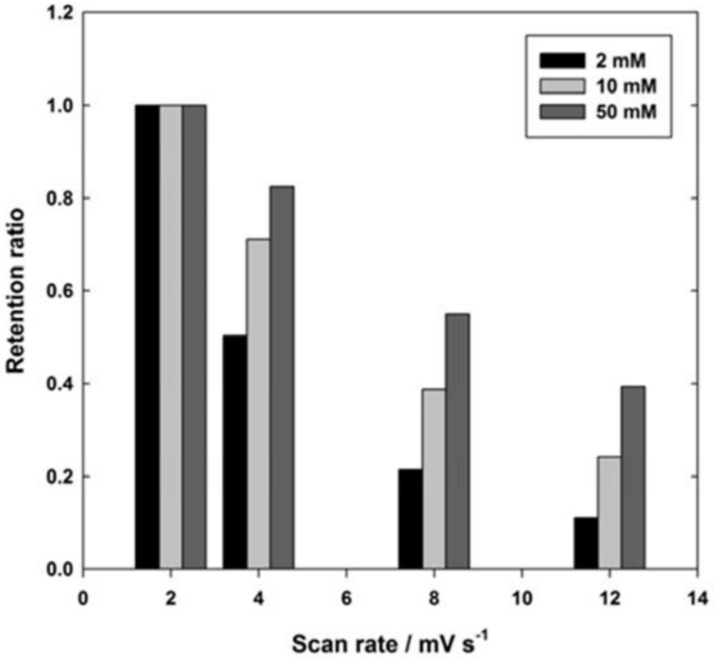

Figure 4-29. Retention ratio as functions of scan rate and salt concentration (electrode thickness=300 μm).

To correlate the evaluated rate capability with a conventional CDI operation, constant current operation was carried out as a function of the current density with respect to the electrode thickness. Fig. 4-30 shows the mean deionization rate [17, 82] of the electrodes with different thicknesses as a function of the current density. As can be seen in the figure, the mean deionization rate of the thinner electrode was higher than that of the thicker electrodes at every current density. The rate of the 200-μm-thick electrode was 0.062 mg/g/s at 9 mA and that of the 300- and 400-μm-thick electrode were 0.047 and 0.036 mg/g/s, respectively. This result is in good agreement with the rate capability evaluated by the potential sweep method; the better rate capability leads to a higher mean deionization rate. Furthermore, electrochemical analysis was carried out at a higher electrolyte concentration (1 M NaCl) compared to the CDI experimental condition (10 mM NaCl). In this way, the capacitive behavior of an electrode, which is the starting point of deionization in CDI, can be exclusively examined focusing on the thickness, while minimizing the contribution of resistance due to the low electrolyte concentration. Though careful attention is required when conventional electrochemical analysis methods are applied in a low electrolyte concentration [2], electrochemical properties obtained at a high electrolyte concentration could provide capacitive behavior of an electrode, which will eventually affect deionization performance in CDI [24].

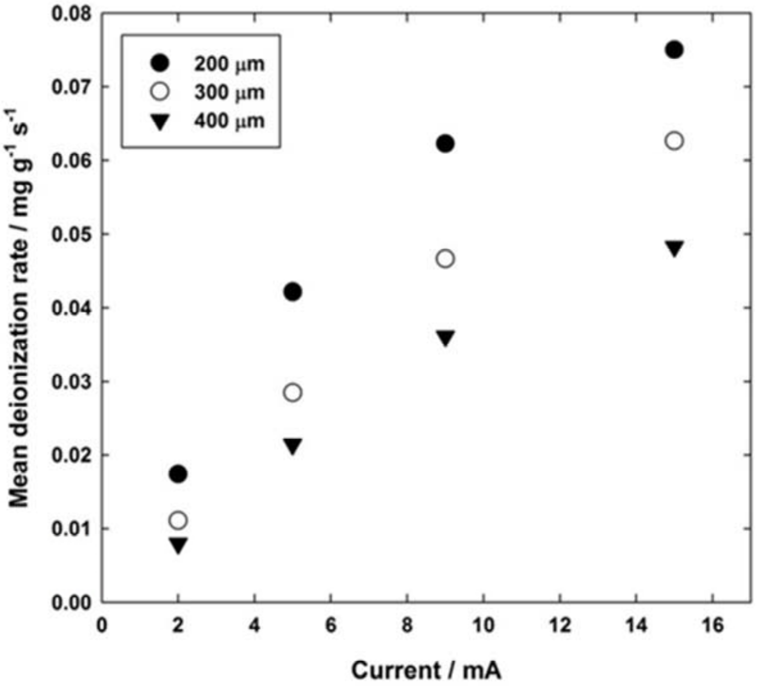

Figure 4-30. Mean deionization rate of the electrodes with different thicknesses as a function of the current density. The mean deionization rate (mg/g/s) was calculated by dividing the deionization capacity (mg/g) by the duration of charging (s). Deionization performance tests were carried out in the constant current mode; the module was charged at various current densities (2, 5, 9, 15 mA) with a cutoff voltage of 1.2 V.

Fig. 4-31 shows the cyclic voltammograms of the carbon electrodes as functions of the electrode thickness and scan rate, which were obtained by dividing the current profile by the scan rate and the mass of the electrode. The results show that the thinner electrode has a better rate capability than that of the thicker electrodes. In the case of 2 mV/s (Fig. 4-31(a)), the shape was rectangular, and their specific capacitance values were 120, 124, and 116 F/g for the 200-, 300-, and 400-μm-thick electrodes, respectively. The capacitance was quite similar regardless of the thickness, indicating that the entire ability of the electrodes was achieved due to the low scan rate. However, the shape became distorted as the scan rate increased to 50 mV/s (Fig. 4-31(b)); the specific capacitance of the electrodes decreased to 70, 37, and 14 F/g for the 200-, 300-, and 400-μm-thick electrodes, respectively. Particularly, the distortion was significant for the 400-μm-thick electrode, where its capacitance retention ratio ($C_{50\ \mathrm{mV/s}}/C_{2\ \mathrm{mV/s}}$) was only 0.12. The intense distortion and subsequent reduction in the retention ratio revealed that the 400-μm-thick electrode exhibits a retarded current response to the potential sweep. Therefore, a better rate capability was achieved for the thinner electrode.

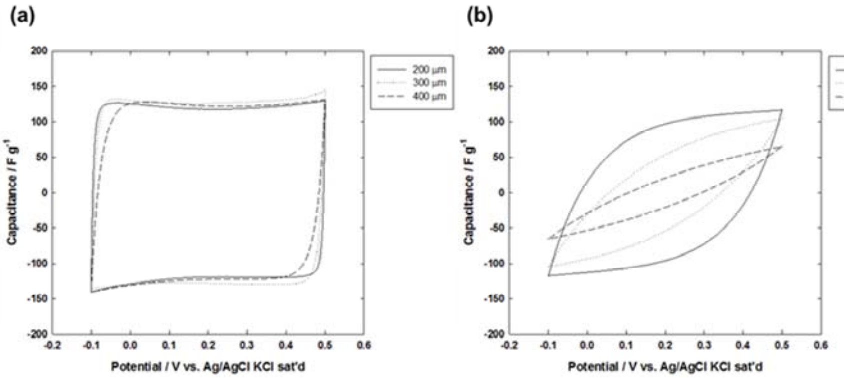

Figure 4-31. Cyclic voltammograms of the carbon composite electrodes with different thicknesses. The results were obtained in 1 M NaCl solution at a scan rate of (a) 2 mV/s and (b) 50 mV/s.

Furthermore, EIS allowed for frequency-dependent analysis as well as equivalent circuit analysis depending on the thickness of the electrodes. First, we obtained the frequency-dependent capacitance of the carbon composite electrodes in a frequency range of 0.002 to 100,000 Hz (Fig. 4-32, the data show up to 100 Hz). As can be seen in this capacitance vs. frequency plot, the capacitance of the 200-µm-thick electrode is the highest (58 F/g at 1 Hz) followed next by that of the 300- (43 F/g) and 400-µm-thick electrodes (33 F/g) between 0.1 and 10 Hz, indicating that the thinner electrode exhibits a better rate capability. Under the higher frequency (>10 Hz), the capacitance approaches to zero because the electrolyte ions hardly penetrate into the pores of the carbon. On the other hand, all the electrodes exhibited their entire capacitance below 0.01 Hz; the capacitance reached to approximately 125 F/g at 0.002 Hz regardless of the thickness. This result is in good agreement with the CV in terms of the rate capability. The electrodes exhibited their entire capacitance at a low scan rate regardless of the thickness, which was relevant to the low frequency in the EIS. However, the capacitance started to decrease as the scan rate and the frequency increased depending on the thickness. In all cases, the thinner electrode showed a better rate capability than that of the others, and ion diffusivity is one of the significant factors affecting the capacitive behavior of the electrodes with different thicknesses [188].

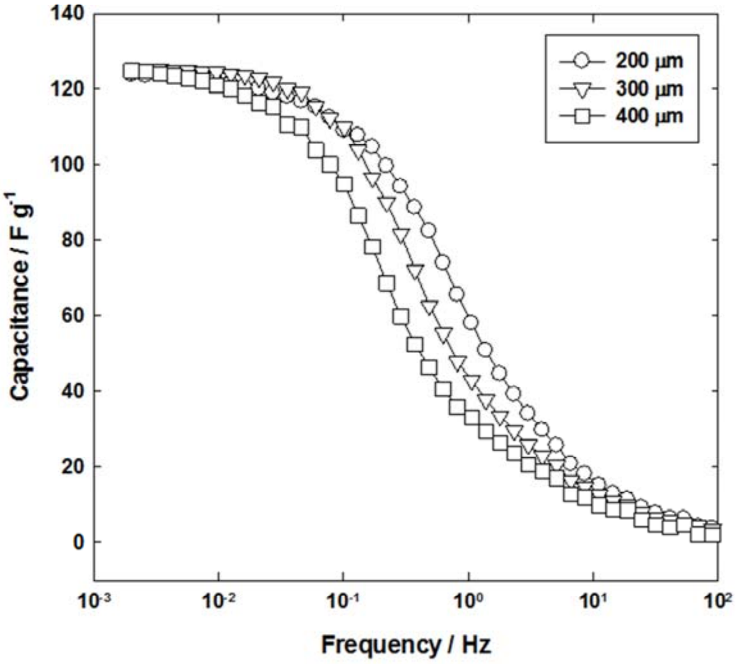

Figure 4-32. Capacitance vs. frequency plots for different electrode thicknesses.

Table 4-2 shows the resulting parameters of the equivalent circuit analysis. As a result, a similar specific capacitance (C_{tot}) was obtained regardless of the thickness confirmed by the above electrochemical characterizations. The other parameters, including the degree of distribution (σ), had no tendency according to the electrode thickness. Interestingly, the characteristic penetrability coefficient (α_{o}^{*}) was found to be closely related to the electrode thickness. The penetrability decreased as the thickness increased, indicating that the thinner electrode was favorable for the penetration of ions inside the electrode. According to Eq. 8, the penetrability coefficient is inversely proportional to the average pore length, which is the average pathway of the ion inside the electrode until it reaches the double layer. The thicker electrodes have a longer pathway; thus, the subsequent lower penetrability contributed to the increased pore resistance. Therefore, the rate capability depending on the thickness can be understood based on the fitting result that the electrode thickness affects the ion penetrability. For the thicker electrode, ion penetration was retarded due to a longer pathway inside the electrode; thus, the current response to the voltage change was also retarded. On the other hand, ion penetration for the thinner electrode was enhanced because of the opposite reason; hence, a better rate capability was achieved.

Table 4-2. Parameters obtained by equivalent circuit analysis as a function of the electrode thickness.

Electrode	C_{tot}[a]/F g^{-1}	σ	α_o*[b]/s$^{-0.5}$	chi squared
200 μm	122	0.384	0.551	0.0013
300 μm	125	0.295	0.418	0.00068
400 μm	124	0.394	0.305	0.00053

[a] Total capacitance

[b] Characteristic penetrability coefficient

4.2.5. Conclusions

In the present study, a new method to evaluate the rate capability in CDI was demonstrated, the potential sweep method. Deionization performance was examined at various scan rates, and the resulting deionization capacity was converted to a normalized parameter; a higher retention ratio indicates a better rate capability. The results show that the thinner electrode exhibited a higher retention ratio (0.32) with an increasing scan rate (2 to 12 mV/s) compared to the thicker electrodes, indicating a better rate capability in deionization. Furthermore, electrochemical analysis showed that the rate capability was affected by the capacitive behavior of the electrode. Particularly, the capacitive behavior to determine the rate capability can be explained by the ion penetrability, which was obtained with an equivalent circuit analysis in the EIS. Electrode thickness was closely related to the average pore length; thus, the relatively short average pore length of the thinner electrode and the subsequent low pore resistance could enhance the rate capability. Therefore, the thickness of an electrode needs to be carefully determined to achieve a versatile CDI system producing various product concentrations with an outstanding rate capability.

5. CDI Ragone Plot as a Functional Tool to Evaluation Deionization Performance in Capacitive Deionization

5.1. Introduction

Capacitive deionization (CDI) is a promising desalination process driven by electrical potential and the consequent double layer formation on the surface of a porous electrode [2, 180]. An excess of counter-ions in the double layer leads to a depletion of ions in the region adjacent to the electrode surface; thus, desalinated water can be produced by extracting the solution between the two electrodes. CDI has attracted much attention compared to conventional desalination processes such as thermal distillation and reverse osmosis (RO) because of its potential for an efficient energy use [117, 138]. Furthermore, the energy consumed during deionization is simultaneously stored in electrodes because its configuration and principle are similar to an energy storage device. Therefore, the stored energy can be conceptually recovered [54, 123, 182, 189], and a practical energy recovery system [152, 190, 191] facilitates low-energy production of fresh water, although it still has a long way to go to realize such an ideal desalination process at this moment.

So far, various attempts have been carried out to achieve an efficient deionization performance. These approaches include synthesizing novel carbon materials [5, 7, 8, 10, 11, 88], modifying carbon electrodes [15, 16], involving Faradaic reactions [19, 20, 87], incorporating ion-exchange membranes or polymers [17, 18, 65], altering operation methods [21], and developing new processes [22, 56, 82]. No matter what strategy CDI implements, it is quite important to determine its deionization performance based on an appropriate evaluation method. However, deionization performance has been reported in various ways; thus, CDI requires a standard method to evaluate the deionization performance which could allow for further advancements in this area. Among the various ways, two indicators have most frequently been reported as representing performance, which are the capacity and rate of deionization. The deionization capacity shows the amount of removed ions per mass of electrodes, normally when the performance reaches its equilibrium [2]. On the other hand, the deionization rate indicates the speed of deionization expressed as the rate constant [7] or capacity divided by time [17, 82]. However, these two parameters have been separately provided at the specific condition, thus facile acquisition of the overall deionization performance is difficult. Therefore, CDI requires a more advanced evaluation method, determining the overall performance which includes the capacity and rate

In this study, we propose a new concept to evaluate deionization performance in CDI called the CDI Ragone plot. Compared to the conventional Ragone plot for energy storage devices, the CDI Ragone plot evaluates the deionization performance taking into consideration both the capacity and rate, which allows for the intuitive acquisition of the overall deionization performance based on a conventional operating method. Herein we show an evaluation methodology and the implications of the CDI Ragone plot along with the effects of the various parameters, as a standard tool for examining deionization performance in CDI.

5.2. Experimental

Carbon composite electrodes were prepared with MSP-20 (Kansai Coke and Chemicals, Japan), carbon black (Super P, Timcal), and polytetrafluoroethylene (PTFE, Aldrich) binder (86:7:7 in weight ratio). A mixture containing these components was kneaded with a few milliliters of ethanol until it solidified, and sheet-type electrodes were made by pressing with a roll-pressing machine. The desirable thickness was obtained by adjusting the gap of the two rollers; the thickness was ~300 μm unless otherwise specified. After the fabrication, the electrodes were dried in a vacuum oven at 120^{o}C for 12 h. Other carbon electrodes (S-51HF (Norit), YS-2 (Japan EnviroChemicals), CEP21 (Power Carbon Technology, Korea), and MDC12 (MOF-derived carbon)) were fabricated with the same procedure.

A custom-built CDI cell was used to evaluate deionization performance, in which built-in graphite current collectors were installed. A pair of round-shape carbon electrodes (20 mm in diameter) having a center hole (4 mm in diameter) was placed onto current collectors, and each electrode was covered by anion- and cation-exchange membranes (selemion, AGC ENGINEERING CO., LTD, Japan) with the same geometry as the electrode (membrane-assisted CDI, MCDI). Between the two ion-exchange membranes, a polymer spacer (thickness=185 μm) was located to allow a feed solution to pass from the outside to the center hole. After the assembly, the CDI cell was pressed and sealed off. A feed solution (2, 10, 50, and 100 mM NaCl) was supplied to the CDI cell with a peristaltic pump (flow rate=1, 2, and 4 ml/min) and the effluent conductivity was collected with a flow-type conductivity meter (3574-10C, HORIBA, Japan) which was connected to the outlet. After passing through the conductivity meter, the effluent was disposed (single-pass mode). All experiments were conducted in a temperature chamber at 25°C.

Deionization performance was evaluated under constant current operation [2, 39]. The CDI cell was controlled with a cycler (WBCS3000, WonaTech, Korea); it was charged under various constant currents (1–25 mA) with a cut-off voltage of 1.2 V followed by short-circuiting for many seconds until the outlet conductivity showed a plateau which was close to the initial conductivity. These steps were repeated 3 times to secure the dynamic equilibrium, and the 3rd cycle was used as a representative profile. The deionization capacity (mg/g, the mass of NaCl (mg) divided by the mass of both electrodes (g)) was derived from the area below the influent conductivity during the charging step [24]. The mean deionization rate (mg/g/s) was obtained by dividing the deionization capacity by the duration of charging (s). It should be noted that operating method (i.e., constant current charging–constant current discharging, constant voltage charging–zero voltage discharging, etc.) or CDI without membranes could result in different deionization performances [17], but our focus was to observe the performance obtained only from constant current charging in MCDI. Detailed operating parameters for each experimental condition are provided in Table 5-1.

Table 5-1. Detailed operating parameters for each experimental condition.

Carbon	**Salt concentration (mM)**	**Flow rate (ml/min)**	**Electrode thickness[a] (μm)**	**Current load (mA)**
MSP-20	2	2	300	1, 2, 3, 4
MSP-20	10	2	300	2, 5, 9, 15, 18
MSP-20	50	2	300	2, 5, 9, 15, 20, 25
MSP-20	100	2	300	2, 5, 9, 15, 20, 25
MSP-20	10	1	300	2, 5, 9, 12
MSP-20	10	4	300	2, 5, 9, 15, 18
MSP-20	10	2	200	2, 5, 9, 15, 18
MSP-20	10	2	400	2, 5, 9, 15, 18
S-51HF	10	2	300	2, 5, 9
YS-2	10	2	300	2, 5, 9, 15, 18
CEP21	10	2	300	2, 5, 9, 15, 18
MDC	10	2	300	2, 5, 9, 15

[a] The numbers refer to characteristic thickness of the electrode. The real electrode thickness varied depending on samples, but its deviation was controlled not to over 10%.

5.3. Results and Discussion

Fig. 5-1(a) shows a conceptual diagram of the CDI Ragone plot, in which x and y axes represent the deionization capacity and mean deionization rate, respectively. This plot combines two important parameters that represent the deionization performance, which are relevant to the energy and power of energy storage devices in a conventional Ragone plot [192]. The most outstanding aspect of the CDI Ragone plot is that it can provide three essential parameters at once: the deionization capacity (x-axis), mean deionization rate (y-axis), and deionization time (dashed lines). More importantly, the overall deionization performance can be evaluated minimizing bias caused by selecting a specific condition. The deionization performance must be evaluated under various current loads to achieve this goal; the lowest and highest current loads could provide the full capacity and maximum rate, respectively. Fig. 5-1(b) shows representative experimental data, which were converted to draw the CDI Ragone plot. As can be seen, steady conductivity profiles were observed below the initial conductivity (dashed line), showing the typical behavior of constant current operation [39]. When operating the CDI cell in this mode, a steady and controlled effluent can be produced depending on the current load; the lower current produces an effluent with a slightly decreased conductivity for a longer time while the higher current produces an effluent with a largely decreased conductivity in a relatively short time. Therefore, a higher mean deionization rate is expected when increasing the current load. On the other hand, the deionization capacity decreases as the current load increases, which could be ascribed to impeded ion transport from the bulk phase to the inside of an electrode and voltage loss because of IR drop. When all of the data points obtained at each current load are plotted, it becomes an arc-shaped line pointing from upper-left to bottom-right in the colored regions in Fig. 5-1(a). There can be two extreme cases; the one with a high rate but a low capacity (denoted by the blue color) and the one with a high capacity but a low rate (denoted by the red color). The goal of developing a CDI electrode or system will be to shift the plot toward the upper, right region of the plot, which represents the ideal deionization performance (denoted by the green color).

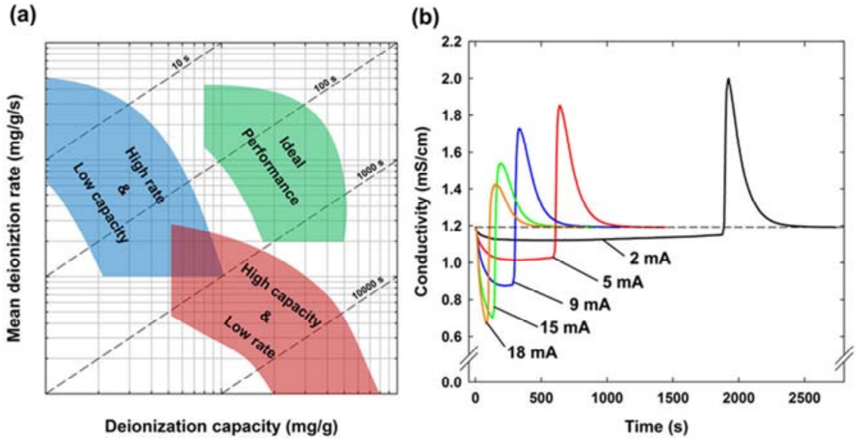

Figure 5-1. A conceptual diagram of a CDI Ragone plot (a) and the representative conductivity profiles (b). A CDI Ragone plot consists of the deionization capacity and mean deionization rate, indicating total removed ions

during charging and deionization capacity divided by duration of charging, respectively. These two parameters were obtained under constant current charging followed by zero-voltage discharging shown in (b); the area below the influent conductivity (dashed line) refers to the removed ions by the CDI cell. Data points obtained at each current load are located in the CDI Ragone plot, thus becoming a curve representing its experimental condition. The location and shape of a curve represent the deionization performance; two imaginary cases would be a high rate & low capacity (blue color) and a high capacity & low rate (red color). An ideal CDI system would shift a curve toward the upper, right region of the plot (green color).

To confirm the implications of the CDI Ragone plot, prevalent parameters affecting the deionization performance were examined including salt concentration, flow rate, electrode thickness, and types of carbon materials. First, we investigated the effect of salt concentration (2–100 mM NaCl) on the CDI Ragone plot. As shown in Fig. 5-5(a), a higher salt concentration shifted the plot toward the upper, right region of the plot, indicating increases in both the deionization capacity and mean deionization rate. The capacity increase (a shift to the right region) is mainly because of the compaction of the double layer and the subsequent rise in capacitance [24, 122]. In addition, the enhanced rate (a shift to the upper region) can be simply explained by the conductivity increase of the influent solution and the subsequent swift transport of ions from the spacer channel to the electrodes. When comparing the capacity and rate dependent on the salt concentration, more change was observed in the rate than in the capacity; the maximum rate at each highest current load ranged from 0.019 to 0.101 mg/g/s (a five-fold difference), while a relatively minor difference was observed in the full capacity (17.9 to 23.6 mg/g) at each lowest current load. In this regard, a higher salt concentration is advantageous because rapid deionization can be achieved compared to a lower salt concentration. However, it should be noted that the charge efficiency (the ratio of removed ions to transferred charge) [2] has been reported to decrease with an increase in salt concentration [39, 142]. From an energetic point of view, a lower charge efficiency is disadvantageous because it implies that more energy is consumed for deionization. Table 5-2 shows deionization capacity, charge, and charge efficiency obtained at different salt concentrations in Fig. 5-5(a). As can be seen, both deionization capacity and charge increase as salt concentration increases up to 50 mM NaCl. However, deionization capacity of 100 mM is similar to that of 50 mM, while charge increases consistently (also see Fig. 5-2). As a consequence, charge efficiency (ratio of deionization capacity to charge) decreases above 50 mM NaCl; no more enhanced deionization capacity can be achieved with an increase in energy consumption. Therefore, a higher salt concentration becomes disadvantageous in terms of energy use, though deionization rate can be enhanced as electrolyte resistance decreases.

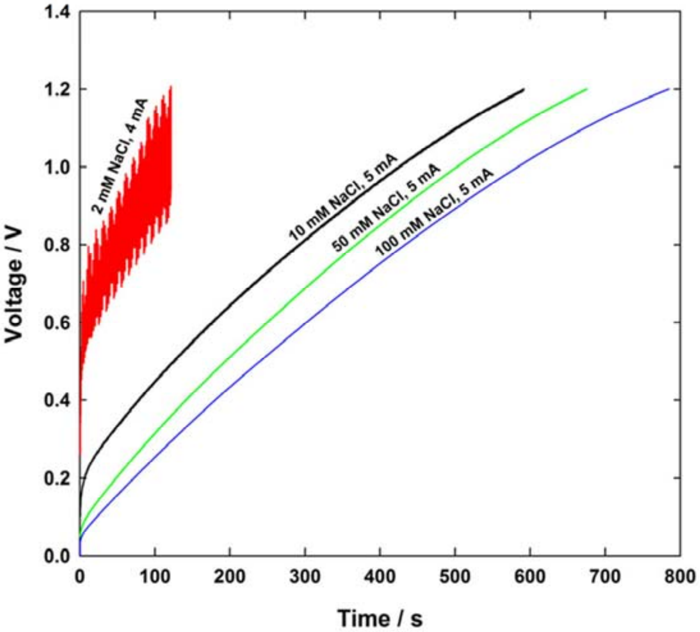

Figure 5-2. Representative voltage profiles of different salt concentrations obtained during charging step.

Next, the effect of flow rate (1–4 ml/min) on deionization performance was examined as plotted in Fig. 5-5(b). The result shows that each plot converges to one point at the lowest current load, indicating a similar deionization capacity and mean deionization rate, while the difference becomes significant as the current load increases. A lower current load allows enough time for ion transport from a bulk phase to an electrode regardless of the flow rate. At a higher current load, however, a higher flow rate could provide more ions in response to an increase in the current load compared to a lower flow rate (see Fig. 5-3), thus exhibiting a higher capacity and rate. This is in good agreement with a previous study on flow rate [17], and also extended the previous result by evaluating the overall performance, which is the major advantage of the CDI Ragone plot.

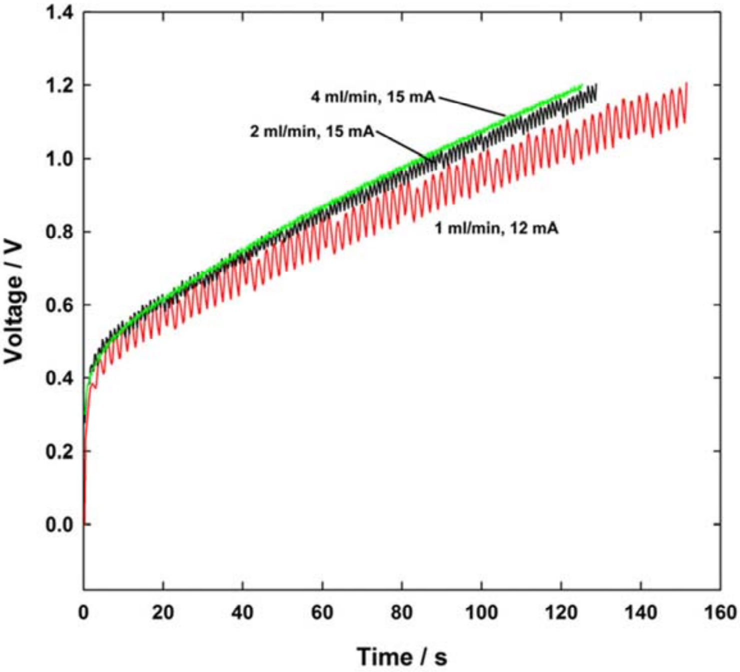

Figure 5-3. Representative voltage profiles of different flow rates during charging step.

Fig. 5-5(c) shows the deionization performance depending on the variation in electrode thicknesses (200–400 μm), which is extended result of our previous work [27]. As can be seen, the plot shifts upward when increasing the electrode thickness, indicating faster deionization, while the full capacity obtained at the lowest current load for each thickness shows a similar value. This tendency was still valid when the electrode became thinner than 200 μm (see Fig. 5-4). The result confirms the strong influence of the electrode thickness on the rate of deionization [10], which is one of the important parameters when designing and optimizing a CDI process. Compared to previous two parameters, however, the variation in the thickness led to different carbon loading on the electrode; a different CDI Ragone plot would come out when it is normalized by another basis (e.g., foot print area, see Fig. 5-6), so that a careful attention is required to interpret the plot. In addition, thinner electrodes require more stacks to be assembled into a CDI module with fixed volume; thus, it requires more ion-exchange membranes/coatings which are disadvantageous in an economic point of view. Also, increased number of stacks in a CDI module decreases flow rate in each spacer channel, which would deteriorate deionization performance as shown in Fig. 5-5(b).

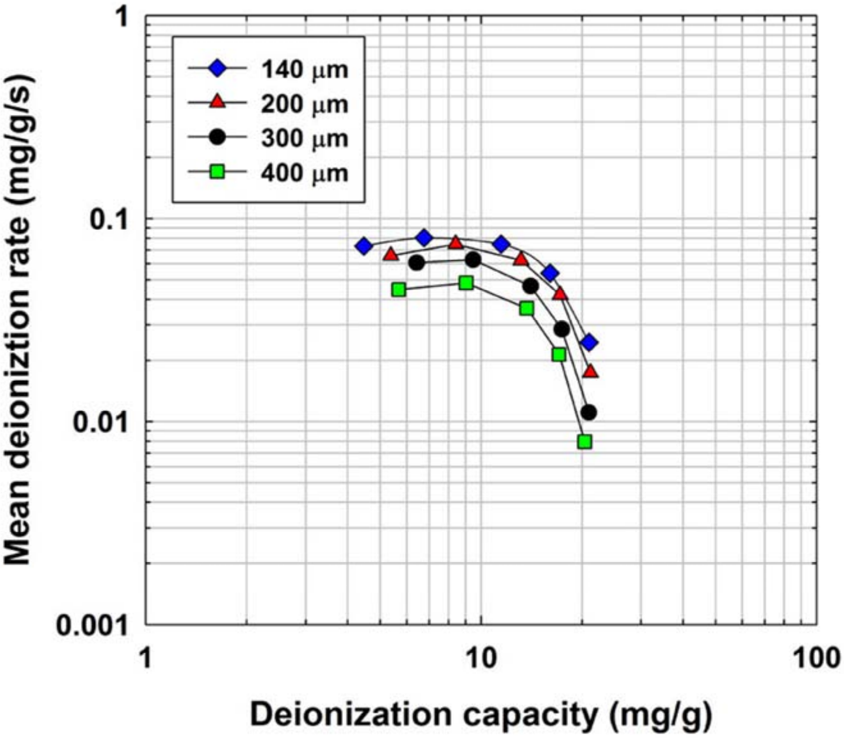

Figure 5-4. Extended data of variation in electrode thickness. Original figure (Fig. 5-5(c)) contained plots for various electrodes in the range of 200 to 400 μm. In a further experiment, more thinner electrode (140 μm, ◆) was fabricated and plotted together with the previous electrodes. The plot for the 140-μm-thick electrode was located above the 200-μm-thick electrode, indicating better deionization rate. It implies that the influence of electrode thickness on rate is valid even below 200 μm.

Lastly, we show a comparison of various carbon materials on the CDI Ragone plot, which is the most frequently used approach by developing novel electrodes. As shown in Fig. 5-5(d), the CDI Ragone plot enables a comprehensive comparison of electrodes made of various carbon materials at a glance in terms of deionization performance. First, a comparison of microporous activated carbons (S-51HF (▲), YS-2 (■), and MSP-20 (●)) [24] shows the effect of surface area on the deionization capacity and rate. A higher surface area and subsequent capacitance [24] shifted the plot toward the upper, right side of the CDI Ragone plot, indicating a higher capacity and rate. When comparing MSP-20 (●) and CEP21 (▼), for which CEP21 is relatively hydrophobic (see Fig. 5-7), CEP21 exhibited a higher capacity at the lowest current load but its capacity and rate decreased with increasing current load. It can be inferred that hydrophobicity inhibited the transport of ions inside the electrode [193], and this interruption became significant when faster charging was implemented. Therefore, we could deduce from the CDI Ragone plot that carbon which is more hydrophilic (MSP-20) is a better option for rapid deionization. The CDI Ragone plot also could be used to find the role of pore structures on deionization performance. As reported in our previous study [11], a large pore size could facilitate the rapid transport of ions, thus resulting in rapid deionization. We observed that MDC (◆) is located more in the upper region of the plot than that of the other materials, especially at the higher current load, indicating faster deionization. On the other hand, its capacity is relatively low, indicating a tradeoff behavior between capacity and rate as in the case of the 'high rate & low capacity' shown in Fig. 5-1(a). However, similar to the case of the variation in the thickness, a careful attention is required because the activated carbons had different pore structure, especially the MDC. Though the large pore size of MDC could facilitate the performance when it is shown in the mass basis, but its low density led to poor performance based on area of the electrode (see Fig. 5-6(b)). In other words, the conventional mass-based normalization for desalination performance needs improvement to be applicable for entire parameters that were discussed above. Among various normalization units (e.g., mg/g, mg/cm^2, mg/cm^3), the performance based on electrode volume (mg/cm^3) could provide more beneficial information for commercialization because overall performance can be determined under restricted volume of the CDI system in practice. However, normalization by electrode volume still makes bias for the electrode thickness; the mass- (Fig. 5-5(c)) and volume-based (data not shown) CDI Ragone plots are the same in terms of their relative locations (the thinner electrode was located upward), leading to conflicting result compared to the overall performance assessed from the area-based normalization (Fig. 5-6(a)). Therefore, it is recommended to fix the electrode thickness in order to use volume-based performance, suggesting a standard experimental condition should be made together with a normalization basis in future studies. From the result that was obtained in various parameters, the CDI Ragone plot was found to be a functional tool to investigate and optimize the desalination performance of a system; it could provide overall desalination performance in terms of capacity and rate. Furthermore, the CDI Ragone plot could be used to determine an optimal current load depending on its applications: maximum capacity, rate, and balanced performance between capacity and rate. Comparison between studies would be possible after a standard experimental setup is defined in the future study. More importantly, this study could produce many sequel studies based on various standards (e.g., volume-based capacity or full cycle-based rate), operation methods (e.g., constant voltage), and configurations (e.g., CDI without membranes or flow-electrode CDI).

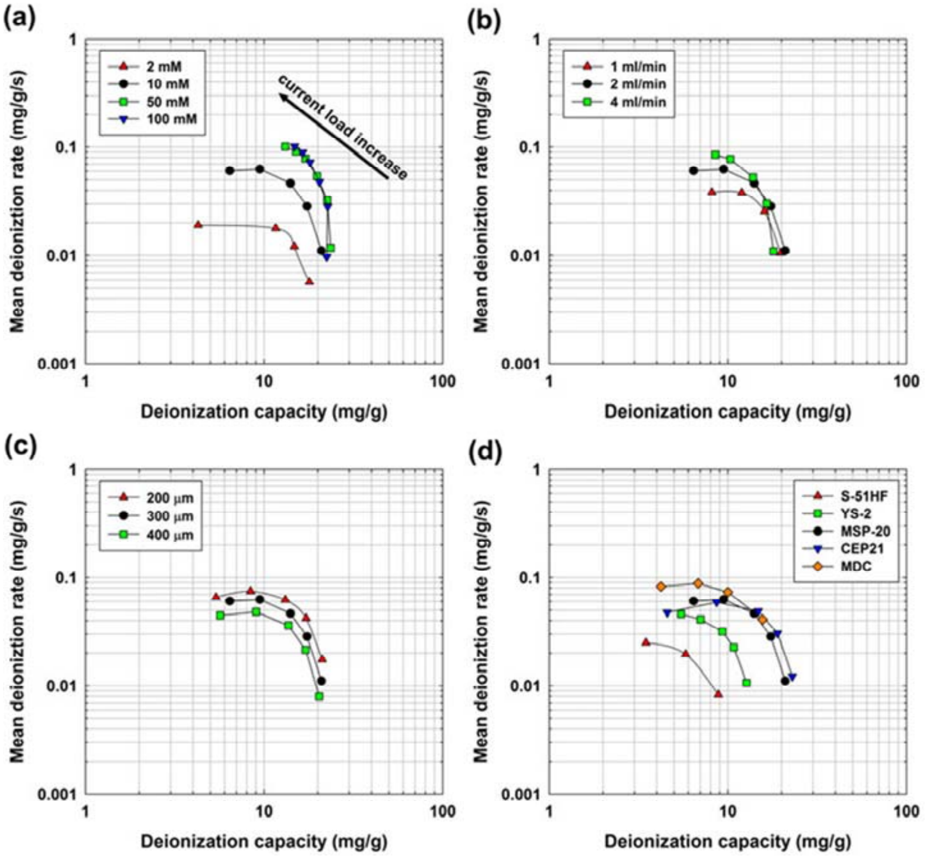

Figure 5-5. Effect of various parameters on the CDI Ragone plot. Each plot shows the effect of the (a) salt concentration, (b) flow rate, (c) electrode thickness, and (d) type of carbon materials. Each parameter was examined based on the standard operating condition (10 mM NaCl, 2 ml/min, 300 µm, and MSP-20), and the range of the current load was from 1 to 25 mA but properly adjusted to show the overall performance. Detailed operating parameters for each experimental condition are provided in Table 5-1.

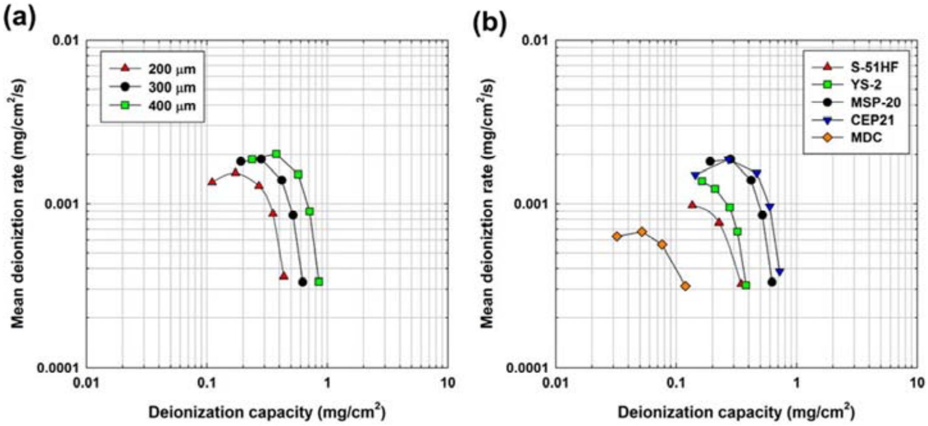

Figure 5-6. CDI Ragone plots normalized by foot print area of electrode (3.02 cm^2) for (a) electrode thickness and (b) type of carbon materials. Results of Figs. 5-5(c) and 5-5(d) were converted from mass-based performance (mg/g and mg/g/s) to area-based performance (mg/cm^2 and mg/cm^2/s). All experiments were carried out under the standard operating condition (10 mM NaCl, 2 ml/min, 300 μm, and MSP-20), unless otherwise indicated. Detailed operating parameters for each experimental condition are provided in Table 5-1.

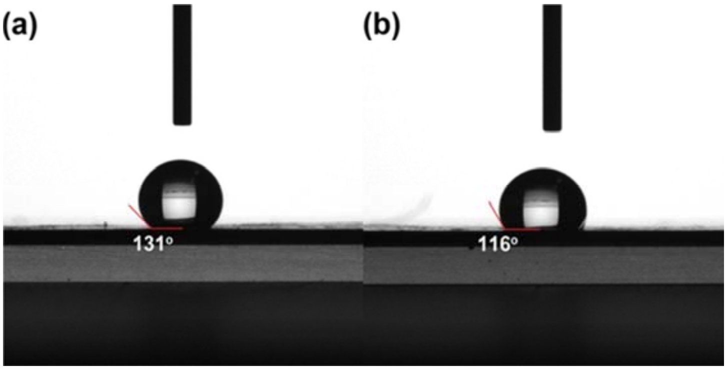

Figure 5-7. Contact angle images of (a) CEP21 and (b) MSP-20. To obtain these images and contact angle values, a contact angle analyzer (KRÜSS, DSA100, Germany) and DSA100 software were used. The electrode was dried prior to the measurement and installed to the analyzer. Then, 6 µL of deionized (DI) water attached at the tip of a needle was smoothly transferred to the electrode surface by direct contact and following detachment. The contact angle measurement was immediately made after the transfer in order to avoid water penetration into the electrode and evaporation. The contact angle was collected from five different points of the electrode, and the resulting averaged values were 131±1 and 116 ± 3^{o} for CEP21 and MSP-20, inferring that the surface of MSP-20 is more hydrophilic compared to that of CEP21. Though various factors could affect contact angle measurement, oxygen functional groups developed on the carbon would play a major role. XPS analysis confirmed that atomic O/C ratio of MSP-20 was 0.20, which is two-fold higher than that of CEP21 (0.10), indicating MSP-20 contains more oxygen functional groups.

From the results that we have found in this study, provisional relationship can be suggested to provide an insight to design/select carbon materials for CDI applications. As shown in Fig. 5-8(a), small pores developed in a carbon material lead to high specific surface area and subsequent high deionization capacity. On the other hand, large pores increase pore volume of a carbon material and facilitate the transport of ions. Therefore, well-developed small pores of activated carbons (MSP-20 and CEP21 in Fig. 5-8(b)) resulted in high deionization capacity, and large pores of MDC enhanced the mean deionization rate (MDC in Fig. 5-8(b)). However, this relationship is valid only when deionization performance was evaluated based on the mass of electrodes. Volume-based deionization performance (Fig. 5-9) showed a completely reversed result for a carbon material containing large pore size. As shown in Fig. 5-9(a), large pore size would show poor deionization performance both for capacity and rate. A carbon material with large pores has low density, thus containing less amount of carbon in a fixed volume. Therefore, such carbon material (e.g. MDC in Fig. 5-9(b)) shows poor deionization performance. In practice, volume of CDI module is quite important, thus both mass- and volume-based deionization performance should be taken into account when designing carbon materials.

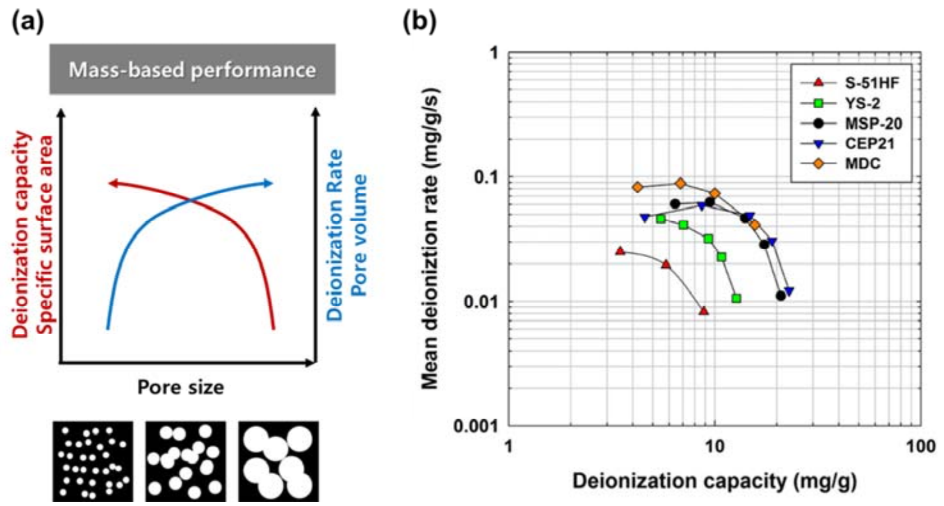

Figure 5-8. (a) Mass-based deionization performance as a function of pore size and (b) the CDI Ragone plot of various carbon materials normalized by the mass of electrodes.

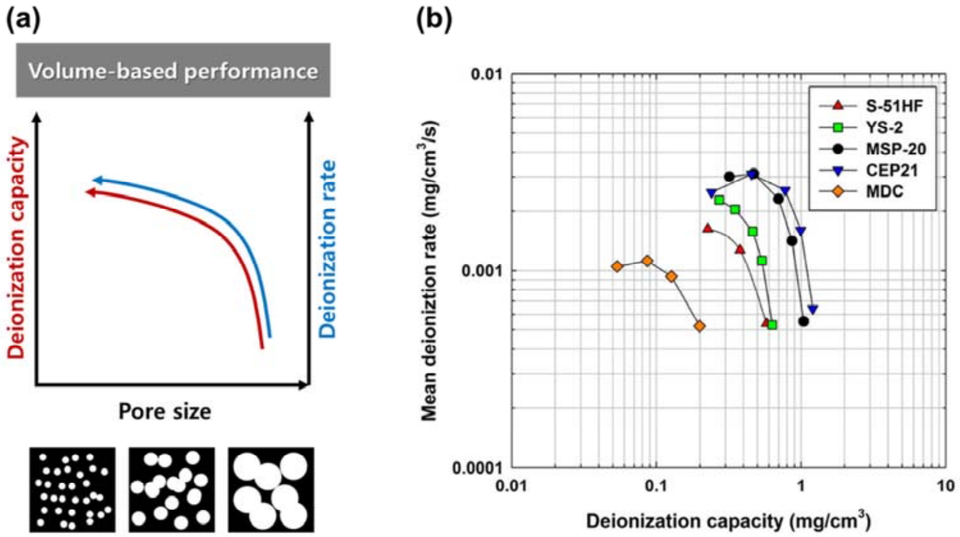

Figure 5-9. (a) Volume-based deionization performance as a function of pore size and (b) the CDI Ragone plot of various carbon materials normalized by the volume of electrodes.

5.4. Conclusion

A novel concept to evaluate deionization performance was proposed, called the CDI Ragone plot. This plot can facilitate the design and optimization of the CDI process depending on its application. From the comparative study on various parameters using the CDI Ragone plot, optimal conditions can be suggested for the best desalination performance in terms of the deionization capacity and rate. In the CDI Ragone plot, a upper, right side shift in the plot is favorable because it indicates a higher deionization capacity and rate. This kind of shift was achieved by increasing the salt concentration and flow rate, and decreasing the electrode thickness. In addition, three carbon electrodes exhibited outstanding desalination performance (mg/g and mg/g/s) in different aspects. CEP21 had the highest capacity with a poor rate performance and MDC had the highest rate with a low capacity while MSP-20 was in between the two. However, MDC exhibited the poor desalination performance in the different normalization units (mg/cm^2 and mg/cm^2/s), suggesting the necessity of improving the conventional mass-based normalization method. Therefore, a standard experimental condition and normalization basis are required for more reliable evaluation of various parameters and for comparison between studies. Such accomplishment can make the CDI Ragone plot to facilitate designing and optimizing the CDI process, working as a comprehensive guide to evaluate desalination performance.

6. Conclusions

In this dissertation, deionization performance was investigated in relation to physicochemical and electrochemical properties of carbon electrodes. In the first part, it was confirmed that high surface area and subsequent high capacitance exhibited a higher deionization capacity. To predict the capacity upon applied voltage, a model equation was adopted and it successfully described capacity, charge, and charge efficiency over applied voltage. In particular, reduced charge efficiency was obtained by increasing discharge voltage without sacrificing the capacity, which was proved by experimental results as well as the model equation. In the second part, hierarchically porous carbon, MDC, exhibited rapid deionization performance compared to microporous and mesoporous carbon electrodes due to its unique pore structure. Moreover, to evaluate rate capability, potential sweep method was proposed which allowed systematic comparison for various parameters such as electrode thickness, salt concentration, and flow rate. Lastly, the CDI Ragone plot was proposed as a comprehensive guide for deionization performance in CDI. It enabled intuitive acquisition of deionization performance of a specific experimental condition by providing available deionization capacity and rate at a glance. In conclusion, this dissertation further extended previous understandings on deionization capacity and rate. Importantly, a novel concept was proposed, called the CDI Ragone plot, to properly show the overall deionization performance, which would become a standard for CDI.

References

[1] M.A. Shannon, P.W. Bohn, M. Elimelech, J.G. Georgiadis, B.J. Marinas, A.M. Mayes, Nature, 452 (2008) 301-310.

[2] S. Porada, R. Zhao, A. Van Der Wal, V. Presser, P. Biesheuvel, Prog. Mater Sci., 58 (2013) 1388-1442.

[3] L.L. Zhang, X. Zhao, Chem. Soc. Rev., 38 (2009) 2520-2531.

[4] C.J. Gabelich, T.D. Tran, I.M. Suffet, Environ. Sci. Technol., 36 (2002) 3010-3019.

[5] C. Tsouris, R. Mayes, J. Kiggans, K. Sharma, S. Yiacoumi, D. DePaoli, S. Dai, Environ. Sci. Technol., 45 (2011) 10243-10249.

[6] G. Wang, Q. Dong, Z. Ling, C. Pan, C. Yu, J. Qiu, J. Mater. Chem., 22 (2012) 21819-21823.

[7] H. Li, L. Zou, L. Pan, Z. Sun, Environ. Sci. Technol., 44 (2010) 8692-8697.

[8] Z.-Y. Yang, L.-J. Jin, G.-Q. Lu, Q.-Q. Xiao, Y.-X. Zhang, L. Jing, X.-X. Zhang, Y.-M. Yan, K.-N. Sun, Adv. Funct. Mater., (2014).

[9] L. Wang, M. Wang, Z.-H. Huang, T. Cui, X. Gui, F. Kang, K. Wang, D. Wu, J. Mater. Chem., 21 (2011) 18295-18299.

[10] S. Porada, L. Borchardt, M. Oschatz, M. Bryjak, J. Atchison, K. Keesman, S. Kaskel, P. Biesheuvel, V. Presser, Energy & Environmental Science, 6 (2013) 3700-3712.

[11] S.J. Yang, T. Kim, K. Lee, Y.S. Kim, J. Yoon, C.R. Park, Carbon, 71 (2014)

294-302.

[12] H.-J. Oh, J.-H. Lee, H.-J. Ahn, Y. Jeong, Y.-J. Kim, C.-S. Chi, Thin Solid Films, 515 (2006) 220-225.

[13] W. Huang, Y. Zhang, S. Bao, R. Cruz, S. Song, Desalination, 340 (2014) 67-72.

[14] F. Duan, Y. Li, H. Cao, Y. Xie, Y. Zhang, Desalination and Water Treatment, 52 (2014) 1388-1395.

[15] H. Yin, S. Zhao, J. Wan, H. Tang, L. Chang, L. He, H. Zhao, Y. Gao, Z. Tang, Adv. Mater., 25 (2013) 6270-6276.

[16] L. Han, K. Karthikeyan, M. Anderson, J. Wouters, K.B. Gregory, Electrochim. Acta, 90 (2013) 573-581.

[17] R. Zhao, O. Satpradit, H. Rijnaarts, P. Biesheuvel, A. van der Wal, Water Res., 47 (2013) 1941-1952.

[18] Y.-J. Kim, J.-H. Choi, Water Res., 44 (2010) 990-996.

[19] J. Lee, S. Kim, C. Kim, J. Yoon, Energy & Environmental Science, (2014).

[20] M. Pasta, C.D. Wessells, Y. Cui, F. La Mantia, Nano Lett., 12 (2012) 839-843.

[21] T. Kim, J.E. Dykstra, S. Porada, A. van der Wal, J. Yoon, P.M. Biesheuvel, J. Colloid Interface Sci.

[22] S.-i. Jeon, H.-r. Park, J.-g. Yeo, S. Yang, C.H. Cho, M.H. Han, D.K. Kim, Energy & Environmental Science, 6 (2013) 1471-1475.

[23] G. Wang, B. Qian, Q. Dong, J. Yang, Z. Zhao, J. Qiu, Sep. Purif. Technol.,

103 (2013) 216-221.

[24] T. Kim, J. Yoon, J. Electroanal. Chem., 704 (2013) 169-174.

[25] R. Zhao, P. Biesheuvel, H. Miedema, H. Bruning, A. Van der Wal, The Journal of Physical Chemistry Letters, 1 (2009) 205-210.

[26] S. Porada, M. Bryjak, A. Van Der Wal, P. Biesheuvel, Electrochim. Acta, 75 (2012) 148-156.

[27] T. Kim, H.D. Yoo, S.M. Oh, J. Yoon, Electrochim. Acta, 139 (2014) 374-380.

[28] C.-H. Hou, J.-F. Huang, H.-R. Lin, B.-Y. Wang, Journal of the Taiwan Institute of Chemical Engineers, 43 (2012) 473-479.

[29] J.-B. Lee, K.-K. Park, S.-W. Yoon, P.-Y. Park, K.-I. Park, C.-W. Lee, Desalination, 237 (2009) 155-161.

[30] L. Chang, Y. Zhou, X. Duan, Desalination and Water Treatment, (2013) 1-7.

[31] L. Chang, Y. Yu, X. Duan, W. Liu, Sep. Sci. Technol., 48 (2012) 359-365.

[32] 윤제용, 김태영, 김춘수, 김정찬, 이재한, 조규식, 축전식 탈염기술을 위한 고기능, 고성능의 탄소 전극 개발 (환경융합신기술 개발사업, 223-111-003) 최종보고서, (2013).

[33] S. Nadakatti, M. Tendulkar, M. Kadam, Desalination, 268 (2011) 182-188.

[34] P. Biesheuvel, R. Zhao, S. Porada, A. Van der Wal, J. Colloid Interface Sci., 360 (2011) 239-248.

[35] Y.-J. Kim, J.-H. Choi, Sep. Purif. Technol., 71 (2010) 70-75.

[36] J.-H. Lee, J.-H. Choi, J. Membr. Sci., 409 (2012) 251-256.

[37] Z. Chen, H. Zhang, C. Yang, X. Sun, H. Guo, C. Wu, F. Xue, L. Gao, Desalination and Water Treatment, 51 (2013) 3489-3496.

[38] Y.-J. Kim, J.-H. Kim, J.-H. Choi, J. Membr. Sci., 429 (2013) 52-57.

[39] R. Zhao, P. Biesheuvel, A. Van der Wal, Energy & Environmental Science, 5 (2012) 9520-9527.

[40] S.-J. Kim, J.-H. Choi, J.-H. Kim, Process Biochem., 47 (2012) 2051-2057.

[41] J.-H. Yeo, J.-H. Choi, Desalination, 320 (2013) 10-16.

[42] B.-H. Park, Y.-J. Kim, J.-S. Park, J. Choi, Journal of Industrial and Engineering Chemistry, 17 (2011) 717-722.

[43] J.-H. Lee, J.-H. Choi, Desalination and Water Treatment, 51 (2013) 503-510.

[44] L. Zou, G. Morris, D. Qi, Desalination, 225 (2008) 329-340.

[45] L.M. Chang, X.Y. Duan, W. Liu, Desalination, 270 (2011) 285-290.

[46] P.-I. Liu, L.-C. Chung, H. Shao, T.-M. Liang, R.-Y. Horng, C.-C.M. Ma, M.-C. Chang, Electrochim. Acta, 96 (2013) 173-179.

[47] C. Kim, J. Lee, S. Kim, J. Yoon, Desalination, 342 (2014) 70-74.

[48] E.S. Im, J.-H. Choi, K.Y. Jung, J. Electrochem. Soc., 159 (2012) E198-E203.

[49] P. Hojati-Talemi, L. Zou, M. Fabretto, R.D. Short, Electrochim. Acta, 106 (2013) 494-499.

[50] R. Zhao, M. Van Soestbergen, H. Rijnaarts, A. Van der Wal, M. Bazant, P. Biesheuvel, J. Colloid Interface Sci., 384 (2012) 38-44.

[51] C.-H. Hou, C.-Y. Huang, Desalination, 314 (2013) 124-129.

[52] S.-Y. Huang, C.-S. Fan, C.-H. Hou, J. Hazard. Mater., (2014).

[53] S. Porada, B. Sales, H. Hamelers, P. Biesheuvel, The Journal of Physical Chemistry Letters, 3 (2012) 1613-1618.

[54] S.-i. Jeon, J.-g. Yeo, S. Yang, J. Choi, D.K. Kim, Journal of Materials Chemistry A, 2 (2014) 6378-6383.

[55] K.B. Hatzell, E. Iwama, A. Ferris, B. Daffos, K. Urita, T. Tzedakis, F. Chauvet, P.-L. Taberna, Y. Gogotsi, P. Simon, Electrochem. Commun., 43 (2014) 18-21.

[56] S. Porada, D. Weingarth, H.V. Hamelers, M. Bryjak, V. Presser, P. Biesheuvel, Journal of Materials Chemistry A, 2 (2014) 9313-9321.

[57] S.-J. Seo, H. Jeon, J.K. Lee, G.-Y. Kim, D. Park, H. Nojima, J. Lee, S.-H. Moon, Water Res., 44 (2010) 2267-2275.

[58] E. Avraham, M. Noked, A. Soffer, D. Aurbach, Electrochim. Acta, 56 (2011) 6312-6317.

[59] M.-W. Ryoo, J.-H. Kim, G. Seo, J. Colloid Interface Sci., 264 (2003) 414-419.

[60] M.-W. Ryoo, G. Seo, Water Res., 37 (2003) 1527-1534.

[61] M.T.Z. Myint, J. Dutta, Desalination, 305 (2012) 24-30.

[62] K.C. Leonard, J.R. Genthe, J.L. Sanfilippo, W.A. Zeltner, M.A. Anderson, Electrochim. Acta, 54 (2009) 5286-5291.

[63] J.J. Lado, R.E. Pérez-Roa, J.J. Wouters, M.I. Tejedor-Tejedor, M.A. Anderson, Sep. Purif. Technol., 133 (2014) 236-245.

[64] H.-J. Ahn, J.-H. Lee, Y. Jeong, J.-H. Lee, C.-S. Chi, H.-J. Oh, Materials Science and Engineering: A, 449 (2007) 841-845.

[65] J.-B. Lee, K.-K. Park, H.-M. Eum, C.-W. Lee, Desalination, 196 (2006) 125-134.

[66] G. Wang, C. Pan, L. Wang, Q. Dong, C. Yu, Z. Zhao, J. Qiu, Electrochim. Acta, 69 (2012) 65-70.

[67] J.S. Im, J.G. Kim, Y.-S. Lee, Journal of nanoscience and nanotechnology, 14 (2014) 2268-2273.

[68] J. Liu, S. Wang, J. Yang, J. Liao, M. Lu, H. Pan, L. An, Desalination, 344 (2014) 446-453.

[69] Y. Bai, Z.-H. Huang, X.-L. Yu, F. Kang, Colloids Surf. Physicochem. Eng. Aspects, 444 (2014) 153-158.

[70] A.G. El-Deen, N.A. Barakat, K.A. Khalil, H.Y. Kim, Journal of Materials Chemistry A, 1 (2013) 11001-11010.

[71] A.G. El-Deen, N.A. Barakat, K.A. Khalil, H.Y. Kim, New J. Chem., 38 (2014) 198-205.

[72] J.C. Farmer, D.V. Fix, G.V. Mack, R.W. Pekala, J.F. Poco, J. Electrochem. Soc., 143 (1996) 159-169.

[73] J. Farmer, D. Fix, G. Mack, R. Pekala, J. Poco, J. Appl. Electrochem., 26 (1996) 1007-1018.

[74] J.C. Farmer, S.M. Bahowick, J.E. Harrar, D.V. Fix, R.E. Martinelli, A.K. Vu, K.L. Carroll, Energy & Fuels, 11 (1997) 337-347.

[75] C.-J. Kim, G. Seo, Korean Chem. Eng. Res., 42 (2004) 532-537.

[76] G.T. Lee, W.I. Cho, B.W. Cho, Journal of the Korean Electrochemical Society, 8 (2005) 77-81.

[77] X. Gao, A. Omosebi, J. Landon, K. Liu, Electrochem. Commun., 39 (2014) 22-25.

[78] M. Zafra, P. Lavela, G. Rasines, C. Macías, J. Tirado, C. Ania, Electrochim. Acta, 135 (2014) 208-216.

[79] M. Zafra, P. Lavela, G. Rasines, C. Macías, J. Tirado, J. Solid State Electrochem., (2014) 1-10.

[80] J. Landon, X. Gao, B. Kulengowski, J.K. Neathery, K. Liu, J. Electrochem. Soc., 159 (2012) A1861-A1866.

[81] D. Kohli, R. Singh, A. Singh, S. Bhartiya, M. Singh, P. Gupta, Desalination and Water Treatment, (2014) 1-7.

[82] M.E. Suss, T.F. Baumann, W.L. Bourcier, C.M. Spadaccini, K.A. Rose, J.G. Santiago, M. Stadermann, Energy & Environmental Science, 5 (2012) 9511-9519.

[83] L. Zou, L. Li, H. Song, G. Morris, Water Res., 42 (2008) 2340-2348.

[84] L. Li, L. Zou, H. Song, G. Morris, Carbon, 47 (2009) 775-781.

[85] J.O. áKiggans Jr, J. Mater. Chem., 20 (2010) 8674-8678.

[86] X. Wang, J.S. Lee, C. Tsouris, D.W. DePaoli, S. Dai, J. Mater. Chem., 20 (2010) 4602-4608.

[87] J. Yang, L. Zou, H. Song, Z. Hao, Desalination, 276 (2011) 199-206.

[88] X. Wen, D. Zhang, L. Shi, T. Yan, H. Wang, J. Zhang, J. Mater. Chem., 22 (2012) 23835-23844.

[89] R. Ryoo, S.H. Joo, M. Kruk, M. Jaroniec, Adv. Mater., 13 (2001) 677-681.

[90] H. Li, L. Pan, T. Lu, Y. Zhan, C. Nie, Z. Sun, J. Electroanal. Chem., 653 (2011) 40-44.

[91] C. Nie, L. Pan, H. Li, T. Chen, T. Lu, Z. Sun, J. Electroanal. Chem., 666 (2012) 85-88.

[92] Q. Li, Y. Ding, D. Yuan, Talanta, 85 (2011) 1148-1153.

[93] J. Yang, L. Zou, N.R. Choudhury, Electrochim. Acta, 91 (2013) 11-19.

[94] C.-H. Hou, N.-L. Liu, H.-L. Hsu, W. Den, Sep. Purif. Technol., 130 (2014) 7-14.

[95] Y. Liu, L. Pan, X. Xu, T. Lu, Z. Sun, D.H. Chua, Electrochim. Acta, 130 (2014) 619-624.

[96] C. Nie, L. Pan, Y. Liu, H. Li, T. Chen, T. Lu, Z. Sun, Electrochim. Acta, 66 (2012) 106-109.

[97] J. Yang, L. Zou, H. Song, Desalination, 286 (2012) 108-114.

[98] H. Li, L. Zou, L. Pan, Z. Sun, Sep. Purif. Technol., 75 (2010) 8-14.

[99] H. Wang, D. Zhang, T. Yan, X. Wen, L. Shi, J. Zhang, J. Mater. Chem., 22 (2012) 23745-23748.

[100] B. Jia, L. Zou, Carbon, 50 (2012) 2315-2321.

[101] Z. Peng, D. Zhang, L. Shi, T. Yan, J. Mater. Chem., 22 (2012) 6603-6612.

[102] Z. Peng, D. Zhang, T. Yan, J. Zhang, L. Shi, Appl. Surf. Sci., 282 (2013)

965-973.

[103] Q. Dong, G. Wang, B. Qian, C. Hu, Y. Wang, J. Qiu, Electrochim. Acta, 137 (2014) 388-394.

[104] D. Zhang, X. Wen, L. Shi, T. Yan, J. Zhang, Nanoscale, 4 (2012) 5440-5446.

[105] D. Zhang, T. Yan, L. Shi, Z. Peng, X. Wen, J. Zhang, J. Mater. Chem., 22 (2012) 14696-14704.

[106] H. Li, S. Liang, J. Li, L. He, Journal of Materials Chemistry A, 1 (2013) 6335-6341.

[107] H. Li, L. Pan, C. Nie, Y. Liu, Z. Sun, J. Mater. Chem., 22 (2012) 15556-15561.

[108] Y. Liu, H. Li, C. Nie, L. Pan, Z. Sun, Desalination and Water Treatment, 51 (2013) 3988-3994.

[109] D. Kohli, R. Singh, M. Singh, A. Singh, R. Khardekar, P. Ram Sankar, P. Tiwari, P. Gupta, Desalination and Water Treatment, 49 (2012) 130-135.

[110] J. Chmiola, G. Yushin, Y. Gogotsi, C. Portet, P. Simon, P.-L. Taberna, science, 313 (2006) 1760-1763.

[111] S. Porada, L. Weinstein, R. Dash, A. Van der Wal, M. Bryjak, Y. Gogotsi, P. Biesheuvel, ACS Applied Materials & Interfaces, 4 (2012) 1194-1199.

[112] M. Eddaoudi, J. Kim, N. Rosi, D. Vodak, J. Wachter, M. O'Keeffe, O.M. Yaghi, science, 295 (2002) 469-472.

[113] S.J. Yang, T. Kim, J.H. Im, Y.S. Kim, K. Lee, H. Jung, C.R. Park, Chem.

Mater., 24 (2012) 464-470.

[114] UNWater, The United Nations World Water Development Report 3, Earthscan, 2009.

[115] M.A. Shannon, P.W. Bohn, M. Elimelech, J.G. Georgiadis, B.J. Mariñas, A.M. Mayes, Nature, 452 (2008) 301-310.

[116] T. Welgemoed, C. Schutte, Desalination, 183 (2005) 327-340.

[117] Y. Oren, Desalination, 228 (2008) 10-29.

[118] I. Villar, S. Roldan, V. Ruiz, M. Granda, C. Blanco, R. Menéndez, R. Santamaría, Energy & Fuels, 24 (2010) 3329-3333.

[119] G. Rasines, P. Lavela, C. Macías, M. Haro, C. Ania, J. Tirado, J. Electroanal. Chem., 671 (2012) 92-98.

[120] L. Van der Pauw, Philips Technical Review, 20 (1958) 220-224.

[121] V. Khomenko, E. Frackowiak, F. Beguin, Electrochim. Acta, 50 (2005) 2499-2506.

[122] A. Bard, L. Faulkner, Electrochemical methods: fundamentals and applications, Wiley New York, 1980.

[123] P. Długołęcki, A. van der Wal, Environ. Sci. Technol., 47 (2013) 4904-4910.

[124] J. Zheng, T. Jow, J. Electrochem. Soc., 144 (1997) 2417-2420.

[125] J.C. Farmer, J.H. Richardson, D.V. Fix, S.L. Thomson, S.C. May, Desalination with carbon aerogel electrodes, in, DTIC Document, 1996.

[126] S. Yoon, J. Lee, T. Hyeon, S.M. Oh, J. Electrochem. Soc., 147 (2000)

2507-2512.

[127] M. Noked, E. Avraham, A. Soffer, D. Aurbach, The Journal of Physical Chemistry C, 113 (2009) 21319-21327.

[128] P. Biesheuvel, J. Colloid Interface Sci., 332 (2009) 258-264.

[129] Y. Bouhadana, E. Avraham, M. Noked, M. Ben-Tzion, A. Soffer, D. Aurbach, The Journal of Physical Chemistry C, 115 (2011) 16567-16573.

[130] Y. Bouhadana, M. Ben-Tzion, A. Soffer, D. Aurbach, Desalination, 268 (2011) 253-261.

[131] Y.A.C. Jande, W.S. Kim, Sep. Purif. Technol., 115 (2013) 224-230.

[132] S. Porada, D. Weingarth, H.V.M. Hamelers, M. Bryjak, V. Presser, P.M. Biesheuvel, Journal of Materials Chemistry A, 2 (2014) 9313-9321.

[133] K.B. Hatzell, E. Iwama, A. Ferris, B. Daffos, K. Urita, T. Tzedakis, F. Chauvet, P.-L. Taberna, Y. Gogotsi, P. Simon, Electrochem. Commun., 43 (2014) 18-21.

[134] Y. Gendel, A.K.E. Rommerskirchen, O. David, M. Wessling, Electrochem. Commun., 46 (2014) 152-156.

[135] I. Cohen, E. Avraham, M. Noked, A. Soffer, D. Aurbach, The Journal of Physical Chemistry C, 115 (2011) 19856-19863.

[136] K. Laxman, M.T.Z. Myint, H. Bourdoucen, J. Dutta, ACS Applied Materials & Interfaces, 6 (2014) 10113-10120.

[137] B.M. Asquith, J. Meier-Haack, B.P. Ladewig, Desalination, 345 (2014) 94-100.

[138] R. Zhao, S. Porada, P.M. Biesheuvel, A. van der Wal, Desalination, 330 (2013) 35-41.

[139] B. van Limpt, A. van der Wal, Desalination, 342 (2014) 148-155.

[140] M. Mossad, L. Zou, Chem. Eng. J., 223 (2013) 704-713.

[141] A. Omosebi, X. Gao, J. Landon, K. Liu, ACS Applied Materials & Interfaces, 6 (2014) 12640-12649.

[142] P.M. Biesheuvel, S. Porada, M. Levi, M. Bazant, J. Solid State Electrochem., 18 (2014) 1365-1376.

[143] E. Avraham, M. Noked, Y. Bouhadana, A. Soffer, D. Aurbach, J. Electrochem. Soc., 156 (2009) P157-P162.

[144] Y.A.C. Jande, W.S. Kim, Desalination, 329 (2013) 29-34.

[145] H. Li, F. Zaviska, S. Liang, J. Li, L. He, H.Y. Yang, Journal of Materials Chemistry A, 2 (2014) 3484-3491.

[146] B. Kastening, M. Heins, Electrochim. Acta, 50 (2005) 2487-2498.

[147] A. Johnson, J. Newman, J. Electrochem. Soc., 118 (1971) 510-517.

[148] P. Biesheuvel, Y. Fu, M.Z. Bazant, Russ. J. Electrochem., 48 (2012) 580-592.

[149] P.M. Biesheuvel, Y. Fu, M.Z. Bazant, Physical Review E, 83 (2011) 061507.

[150] M. Yaniv, A. Soffer, J. Electrochem. Soc., 123 (1976) 506-511.

[151] V.V. Nikonenko, A.V. Kovalenko, M.K. Urtenov, N.D. Pismenskaya, J. Han, P. Sistat, G. Pourcelly, Desalination, 342 (2014) 85-106.

[152] M. Alkuran, M. Orabi, N. Scheinberg, Proc. Applied Power Electronics Conference and Exposition, 2008. APEC 2008. Twenty-Third Annual IEEE, 2008.

[153] P. Wu, J. Huang, V. Meunier, B.G. Sumpter, R. Qiao, The Journal of Physical Chemistry Letters, 3 (2012) 1732-1737.

[154] H. Nishihara, T. Kyotani, Adv. Mater., 24 (2012) 4473-4498.

[155] X. Liu, S. Sen, J. Liu, I. Kulaots, D. Geohegan, A. Kane, A.A. Puretzky, C.M. Rouleau, K.L. More, G.T.R. Palmore, R.H. Hurt, Small, 7 (2011) 2775-2785.

[156] B. Liu, H. Shioyama, T. Akita, Q. Xu, J. Am. Chem. Soc., 130 (2008) 5390-5391.

[157] M.M. Pendergast, E.M.V. Hoek, Energy & Environmental Science, 4 (2011) 1946-1971.

[158] D.-W. Wang, F. Li, M. Liu, G.Q. Lu, H.-M. Cheng, Angew. Chem. Int. Ed., 47 (2008) 373-376.

[159] M. Oschatz, L. Borchardt, M. Thommes, K.A. Cychosz, I. Senkovska, N. Klein, R. Frind, M. Leistner, V. Presser, Y. Gogotsi, S. Kaskel, Angew. Chem. Int. Ed., 51 (2012) 7577-7580.

[160] D.-C. Guo, J. Mi, G.-P. Hao, W. Dong, G. Xiong, W.-C. Li, A.-H. Lu, Energy & Environmental Science, 6 (2013) 652-659.

[161] K. Na, C. Jo, J. Kim, K. Cho, J. Jung, Y. Seo, R.J. Messinger, B.F. Chmelka, R. Ryoo, science, 333 (2011) 328-332.

[162] E. Kockrick, C. Schrage, L. Borchardt, N. Klein, M. Rose, I. Senkovska, S. Kaskel, Carbon, 48 (2010) 1707-1717.

[163] Y. Lv, F. Zhang, Y. Dou, Y. Zhai, J. Wang, H. Liu, Y. Xia, B. Tu, D. Zhao, J. Mater. Chem., 22 (2012) 93-99.

[164] W. Fan, M.A. Snyder, S. Kumar, P.S. Lee, W.C. Yoo, A.V. McCormick, R. Lee Penn, A. Stein, M. Tsapatsis, Nature materials, 7 (2008) 984-991.

[165] Y. Deng, Y. Cai, Z. Sun, D. Gu, J. Wei, W. Li, X. Guo, J. Yang, D. Zhao, Adv. Funct. Mater., 20 (2010) 3658-3665.

[166] P.F. Fulvio, R.T. Mayes, X. Wang, S.M. Mahurin, J.C. Bauer, V. Presser, J. McDonough, Y. Gogotsi, S. Dai, Adv. Funct. Mater., 21 (2011) 2208-2215.

[167] H. Itoi, H. Nishihara, T. Kogure, T. Kyotani, J. Am. Chem. Soc., 133 (2011) 1165-1167.

[168] M. Sevilla, R. Foulston, R. Mokaya, Energy & Environmental Science, 3 (2010) 223-227.

[169] H.-L. Jiang, B. Liu, Y.-Q. Lan, K. Kuratani, T. Akita, H. Shioyama, F. Zong, Q. Xu, J. Am. Chem. Soc., 133 (2011) 11854-11857.

[170] M. Hu, J. Reboul, S. Furukawa, N.L. Torad, Q. Ji, P. Srinivasu, K. Ariga, S. Kitagawa, Y. Yamauchi, J. Am. Chem. Soc., 134 (2012) 2864-2867.

[171] A.J. Amali, J.-K. Sun, Q. Xu, Chem. Commun., 50 (2014) 1519-1522.

[172] T.D. Bennett, A.L. Goodwin, M.T. Dove, D.A. Keen, M.G. Tucker, E.R. Barney, A.K. Soper, E.G. Bithell, J.-C. Tan, A.K. Cheetham, Phys. Rev. Lett., 104 (2010) 115503.

[173] S.S. Kaye, A. Dailly, O.M. Yaghi, J.R. Long, J. Am. Chem. Soc., 129 (2007) 14176-14177.

[174] C.-S. Tsao, C.-Y. Chen, T.-Y. Chung, C.-J. Su, C.-H. Su, H.-L. Chen, U.S. Jeng, M.-S. Yu, P.-Y. Liao, K.-F. Lin, Y.-R. Tzeng, The Journal of Physical Chemistry C, 114 (2010) 7014-7020.

[175] S.J. Yang, C.R. Park, Adv. Mater., 24 (2012) 4010-4013.

[176] P. Kuhn, A. Forget, D. Su, A. Thomas, M. Antonietti, J. Am. Chem. Soc., 130 (2008) 13333-13337.

[177] H. Furukawa, N. Ko, Y.B. Go, N. Aratani, S.B. Choi, E. Choi, A.Ö. Yazaydin, R.Q. Snurr, M. O'Keeffe, J. Kim, O.M. Yaghi, science, 329 (2010) 424-428.

[178] H. Wang, Q. Gao, J. Hu, J. Am. Chem. Soc., 131 (2009) 7016-7022.

[179] D.S. Su, X. Chen, G. Weinberg, A. Klein-Hofmann, O. Timpe, S.B.A. Hamid, R. Schlögl, Angew. Chem. Int. Ed., 44 (2005) 5488-5492.

[180] M. Noked, A. Soffer, D. Aurbach, J. Solid State Electrochem., 15 (2011) 1563-1578.

[181] L. Han, K. Karthikeyan, M. Anderson, K. Gregory, J. Wouters, Electrochim. Acta, (2012).

[182] E. Garcia-Quismondo, C. Santos, J. Lado, J. Palma, M.A. Anderson, Environ. Sci. Technol., 47 (2013) 11866-11872.

[183] H.-K. Song, Y.-H. Jung, K.-H. Lee, L.H. Dao, Electrochim. Acta, 44 (1999) 3513-3519.

[184] H.-K. Song, H.-Y. Hwang, K.-H. Lee, L.H. Dao, Electrochim. Acta, 45 (2000) 2241-2257.

[185] H.-K. Song, J.-H. Sung, Y.-H. Jung, K.-H. Lee, L.H. Dao, M.-H. Kim, H.-N. Kim, J. Electrochem. Soc., 151 (2004) E102-E109.

[186] J.H. Jang, S.M. Oh, J. Electrochem. Soc., 151 (2004) A571-A577.

[187] S. Yoon, J.H. Jang, B.H. Ka, S.M. Oh, Electrochim. Acta, 50 (2005) 2255-2262.

[188] D.N. Futaba, K. Hata, T. Yamada, T. Hiraoka, Y. Hayamizu, Y. Kakudate, O. Tanaike, H. Hatori, M. Yumura, S. Iijima, Nature materials, 5 (2006) 987-994.

[189] M.A. Anderson, A.L. Cudero, J. Palma, Electrochim. Acta, 55 (2010) 3845-3856.

[190] A.M. Pernía, J.G. Norniella, J.A. Martín-Ramos, J. Díaz, J.A. Martinez, Power Electronics, IEEE Transactions on, 27 (2012) 3257-3265.

[191] A. Pernia, F.J. Alvarez-Gonzalez, M. Prieto, P. Villegas, F. Nuno, Power Electronics, IEEE Transactions on, 27 (2014) 3257-3265.

[192] P. Simon, Y. Gogotsi, Nature materials, 7 (2008) 845-854.

[193] J. Zhou, W. Xing, S. Zhuo, Y. Zhao, Solid State Sciences, 13 (2011) 2000-2006.

국문초록

축전식 탈염 (Capacitive deionization, CDI)기술은 새롭게 각광받고 있는 담수화 기술 중의 하나로, 기존에 널리 활용되고 있는 증발법과 역삼투 공정에 비해 간단하고 에너지 측면에서 매우 효율적이며 친환경적인 공정이다. 이러한 장점들을 잘 활용할 경우, 기존의 담수화 공정의 보조 역할을 하여 성능을 극대화할 수 있고 더 나아가서는 적용 목적에 따라 기존 공정을 대체할 수 있다. 이를 위해서는 CDI의 원리를 정확하게 이해하고 담수화 성능을 향상시키는 것이 매우 중요하다. 특히, 담수화 성능을 극대화하기 위해서는 주로 탄소 전극의 역할이 매우 중요하므로 대부분의 연구는 전극 특성 분석, 새로운 탄소 전극 소재 개발, 전극 개질을 중심으로 이루어졌다. 하지만 현재까지의 많은 기술 진보에도 불구하고 담수화 성능에 영향을 미치는 주요인자에 대한 체계적인 연구 성과는 미비한 실정이다. 따라서 본 논문에서는 기존의 CDI에 대한 이해도를 널리 확장하기 위해 용량과 속도를 중심으로 담수화 성능에 대한 연구를 진행하였다. 우선 CDI의 담수화 용량을 분석하기 위해 다양한 크기의 비표면적을 갖는 활성탄소를 이용해 전극을 만들고 이들의 전기화학적 특성과 담수화 성능을 평가하였다. 그 결과, 높은 정전용량을 갖는 전극일수록 높은 담수화 용량을 발휘하는

것으로 확인하였으며, 정전용량으로부터 얻을 수 있는 충전용량의 약 70%를 담수화에 활용할 수 있음을 밝혔다. 추가 연구에서는 염 농도와 충전전압을 통해 담수화 용량을 도출하기 위한 모델식을 이용하여 담수화 성능을 평가하고자 하였다. 그 결과, 실험 결과와 밀접한 상관관계를 갖는 모델식을 도출해낼 수 있었으며 더 나아가서는 방전전압을 조절함에 따라 전하효율을 높일 수 있음을 이론적, 실험적으로 밝힐 수 있었다. 그 다음으로, 담수화 속도에 대한 연구를 위해 새로운 탄소 소재와 함께 속도 특성을 평가할 수 있는 새로운 분석 방법을 제안하였다. 새로운 소재인 metal organic framework-derived carbon (MDC)은 미세, 중형, 대형 기공을 모두 갖고 있는 계층적 기공 구조의 탄소이다. 이를 합성, 전극으로 만든 후 마이크로 또는 메조 크기의 기공만을 갖는 탄소 전극과 전기화학적 특성 및 담수화 성능을 평가하였고, 그 결과 MDC는 계층적 기공 구조로 인해 우수한 속도 특성을 발휘할 수 있는 것으로 나타났다. 속도 특성을 분석하기 위한 새로운 방법으로 일정한 속도로 전압을 변화시키며 충전을 하는 potential sweep method를 이용하였다. 담수화 속도 특성을 평가하기 위해 다양한 주사속도에 담수화 용량을 얻었고, 속도 증가에 따른 용량 유지 비율을 얻을 수 있었다. 빠른 속도로 전위를 증가시켜 충전을 하였을 때

에도 높은 담수화 용량을 발휘할 수 있다면 우수한 담수화 속도 특성을 갖는다고 얘기할 수 있다. 이 새로운 방법을 이용해 전극 두께, 염 농도, 유속 등에 따른 속도 특성을 파악할 수 있고, 전극 두께가 얇을수록, 농도가 높을수록, 유속이 빠를수록 속도 측면에서 유리하다는 것을 밝혔다. 끝으로, CDI의 대표적인 담수화 성능 지표인 용량과 속도를 간단하고 효과적으로 도시하기 위한 CDI Ragone plot을 새롭게 제안하였다. 이는 정전류 운전을 통해 낮은 전류부터 높은 전류의 다양한 조건에서 담수화 용량 및 속도를 얻고 이를 도시하는 방법으로, 한 눈에 최고 용량과 최고 속도를 파악할 수 있어 기존의 방법들에 비해 매우 효과적이다. 결론적으로, 이 논문에서 담수화 용량과 속도에 대한 통찰력 있는 지식을 제공할 수 있었으며, 이 두 지표를 효과적으로 나타낼 수 있는 CDI Ragone plot을 새롭게 제안하였다. 이는 향후 CDI의 종합적 담수화 성능 평가/도시의 표준이 될 수 있는 중요한 개념이 될 것으로 기대된다.

주요어 : 물, 담수화, 축전식 탈염기술, 탄소 전극, 담수화 용량, 담수화 속도

학 번 : 2008-21066